REPORT R-363 AUGUST, 1967

COORDINATED SCIENCE LABORATORY

APPLICATION OF THE AUGER PROCESS TO THE STUDY OF GASEOUS ADSORPTION ON TUNGSTEN

GARY TIBBETTS

UNIVERSITY OF ILLINOIS – URBANA, ILLINOIS

This work was supported in part by the Joint Services Electronics Program (U.S. Army, U.S. Navy, and U.S. Air Force) under Contract No. DA 28 043 AMC 00073(E); and in part by NASA NsG-376.

APPLICATION OF THE AUGER PROCESS TO THE STUDY OF GASEOUS ADSORPTION ON TUNGSTEN

Gary George Tibbetts, Ph.D.
Physics Department
University of Illinois, 1967

Apparatus is described which allows the density of gas adsorbed on metal surfaces to be monitored by observing changes in the number of electrons ejected from the surface by a constant-current, low-energy ion beam. It is shown that the electron emission process (an Auger process) is temperature independent; thus, surface coverages may be easily compared at different temperatures.

Adsorption at room temperature and at the temperature of liquid nitrogen was studied by flash filament and Auger techniques. Desorption kinetics of H_2, CO, and N_2 from polycrystalline, (110), and (111) tungsten foils are discussed. With the exceptions discussed below, these gases are not adsorbed with a few unique binding energies, but they are bound to the surface with a distribution of binding energies. It is shown that desorption at constant temperature from such a distribution of states can be easily distinguished from desorption with a unique binding energy. However, the determination of the order of the desorption process is substantially more difficult. Calculations are presented which illustrate these points.

On each of the surfaces studied, H_2 desorbs with multiple state kinetics and binding energies ranging from 0.7 to 1.8 eV.

CO is bound in a β state on polycrystalline W which actually consists of a large number of states with energies varying between 2.6 and 4.2 eV. From room temperature down to liquid nitrogen temperature (77°K), CO also forms an α state desorbing with multiple state kinetics, and having binding energies between approximately 0.7 and 1.2 eV. On (111) and (110) tungsten, an α state of CO with about the same characteristics forms.

On polycrystalline tungsten, N_2 adsorbs in a β state which consists of a set of many states in a smaller energy region than the corresponding adsorption for CO. Most of the gas is held between 3.7 and 4.3 eV. As the W is cooled below room temperature, an α state, desorbing again with multiple state kinetics and energies up to 0.9 eV, appears. A very similar α state of N_2 occurs on (111) W. N_2 desorbs from a β state on the (111) surface which exhibits a unique activation energy of 3.62 eV. N_2 molecules can be adsorbed in this state to a density of 1 molecule per surface tungsten atom and are desorbed with first order kinetics and rate constant

$$\beta(T) = 1.88 \times 10^{12} \exp\left(\frac{-3.62 \text{ eV}}{kT}\right) \text{ sec.}^{-1}$$

CO adsorbs in a β state on the (111) surface initially with a unique binding energy (3.6 eV), but, as the surface fills to its saturation value of 1 molecule per surface W atom, adsorption into a series of lower energy states occurs.

(110) tungsten does not adsorb nitrogen until it is cooled to

liquid nitrogen temperatures, where N_2 adsorbs in a state of unique binding energy (0.61 eV). This state desorbs with simple first order kinetics. CO does adsorb in a β state on the (110) surface; however, the population of this state is small compared to the corresponding state for the other surfaces.

The relative changes in secondary electron yield observed for different types of gaseous bonding states are discussed. It is found that the change in electron yield due to a molecule bound in an α state is always smaller than the change due to a molecule bound in a β state.

Further applications of the Auger technique and improvements of the present apparatus are indicated.

ACKNOWLEDGEMENTS

The author wishes to acknowledge those without whose generous help this research could never have been completed. Professor Franklin M. Propst, who conceived the underlying idea for this experiment and gave invaluable guidance through the many problems encountered in the course of this research, was instrumental in every phase of this work.

Dr. T. C. Piper, T. L. Cooper, and Dr. A. Dallos each encouraged this work by giving much helpful advice.

J. Garrie Burr gave unflagging interest and energy to the technology of tungsten single crystal foil preparation.

Professor Edgar Luscher stimulated the author's early interest in surface research.

The eager cooperation of the technical staff of C. S. L. is gratefully acknowledged.

Finally, the author's wife, Pat, provided vital understanding and encouragement throughout the years of this research.

TABLE OF CONTENTS

I. INTRODUCTION

This experiment evolved from a three-fold purpose. Firstly, it was a natural extension of previous work on the potential ejection of electrons by ions. Verifying and expanding experimental data concerning the role of adsorbed gas molecules in decreasing the number of secondary electrons could, we felt, deepen knowledge of the basic physical process.

Secondly, we hoped to gain some understanding of the binding of gases on surfaces. Modern desorption experiments have begun to point out the baffling complexity of this binding, so that new "flash filament" experiments are now as likely to produce new questions as new answers.

Thirdly, we hoped to introduce a new tool into surface investigations which could complement information gained by other techniques. While this method is admittedly far more difficult experimentally than, for instance, the flash filament technique, we hoped to show that the use of the two tools in conjunction would be a powerful experimental method.

II. KINETICS OF GASEOUS DESORPTION

A. Introduction

In this work we shall attempt to measure the kinetics of the desorption of gas molecules from a tungsten surface. These molecules may be bound physically, as with dipole-dipole forces, or chemically, as with covalent bonds. The binding energies involved in these cases may vary from less than .4 ev/molecules to more than 5 ev/molecule. The adsorbed gases may be bound either as molecules, or may be dissociatively adsorbed as atoms.

In the following section, the kinetic arguments for the very simple case of gas adsorbed with a single binding energy and desorbing with first or second order kinetics will be reviewed. These conditions are those commonly assumed in the discussion of previous experiments. In the subsequent sections, the modifications of the theory required to treat the more general case of gases adsorbed with a spectrum of binding energies will be discussed. In ChapterIII a brief review of the more useful experimental techniques for studying desorption will be presented.

B. Desorption of Simple States

Consider a warm surface initially containing a number, n(0), molecules/cm^2. The law of mass action implies that molecules adsorbed at a density n(t) ($\frac{\text{molecules}}{cm^2}$) at any time, t, will desorb

according to the rate law,

$$\frac{dn}{dt} = -n^x \beta (T) , \qquad (1)$$

where $x = 1$ if the molecules desorb independently (first order desorption), and $x = 2$ if a collision between two randomly migrating atoms is required prior to desorption (second order desorption). By equating the chemical potentials for a two-dimensional adsorbed gas and a three-dimensional gas, it may be argued that[1]

$$\beta (T) = \nu e^{-E/kT} , \qquad (2)$$

where T is absolute temperature, k is the Boltzmann constant, ν is a vibration or collision frequency, and E is the activation energy for desorption.

If a method were available for measuring $n(t)$, desorption at a fixed temperature would obviously be an advantageous method of studying eq. (1). The solutions of eq. (1) for first and second order desorption at constant temperature are

$$n(t) = n(0)\, e^{-\beta_1(T)t} , \qquad (3)$$

and

$$n(t) = \frac{n(0)}{1 + n(0)\ \beta_2(T)t} , \qquad (4)$$

respectively. Figure 1 shows the shapes of these curves for the case $\beta_1(T) = n(0) \cdot \beta_2(T)$, this condition giving identical desorption

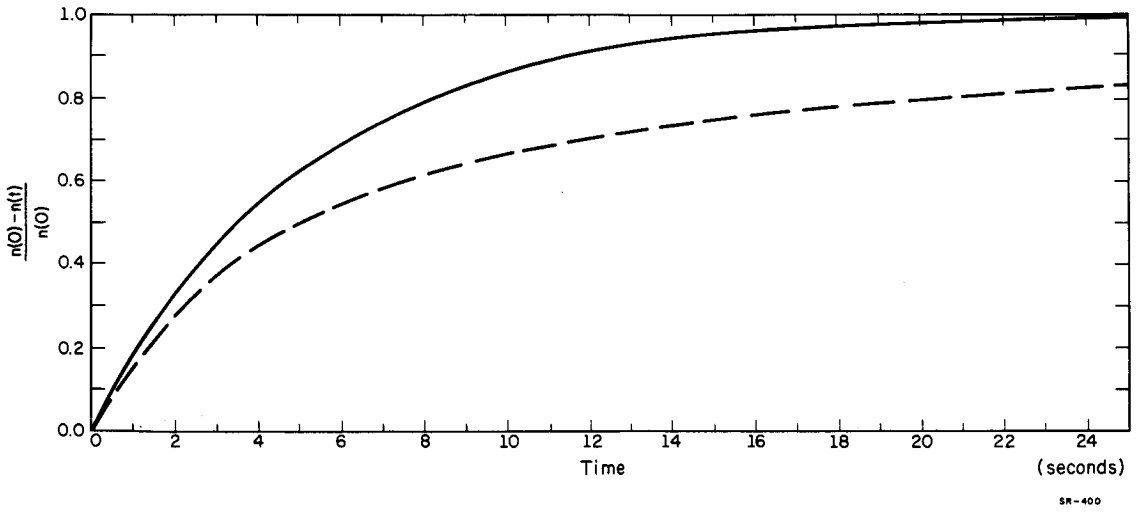

Figure 1. First order (——) and second order (----) single state desorption curves with equal desorption energies, and $\beta_1 = n(0)\,\beta_2 = 1/6$ sec^{-1}, where β_1 is the first order desorption rate constant and β_2 is the second order desorption rate constant.

rates at $t = 0$. For convenience we have plotted $[n(0) - n(t)]/n(t)$ vs time. It is apparent that the exponential first order curve approaches the asymptotic value 1 much faster than the second order curve. To make the distinction even clearer, the logarithm of $\frac{n(0)}{n(t)}$ for these two curves is plotted in Figure 2. Here the first order desorption curve becomes a straight line.

C. Desorption of Multiple States

What if the gases are desorbed at constant temperature T from many states of different binding energies E_j? If 10 independent first order states with initial density $n_j(0)$ and identical ν's are assumed, the surface density at any time t will be given by

$$n(t) = \sum_{j=1}^{10} n_j(0)\, e^{-\nu\,(e^{-E_j/kT})t} , \qquad (5)$$

with

$$n(0) = \sum_{j=1}^{10} n_j(0) .$$

When such a system is abruptly heated to a temperature high enough to quickly desorb the low energy states, but not high enough to desorb the high energy states, the surface coverage, $n(t)$, will tend toward a quasi-equilibrium value. Plotting $\log [n(0)/n(t)]$ vs. t will yield a curve which tends toward a constant value as $n(t)$ approaches quasi-equilibrium, obscuring the exponential behavior of the desorption characteristics. This may be partially alleviated by

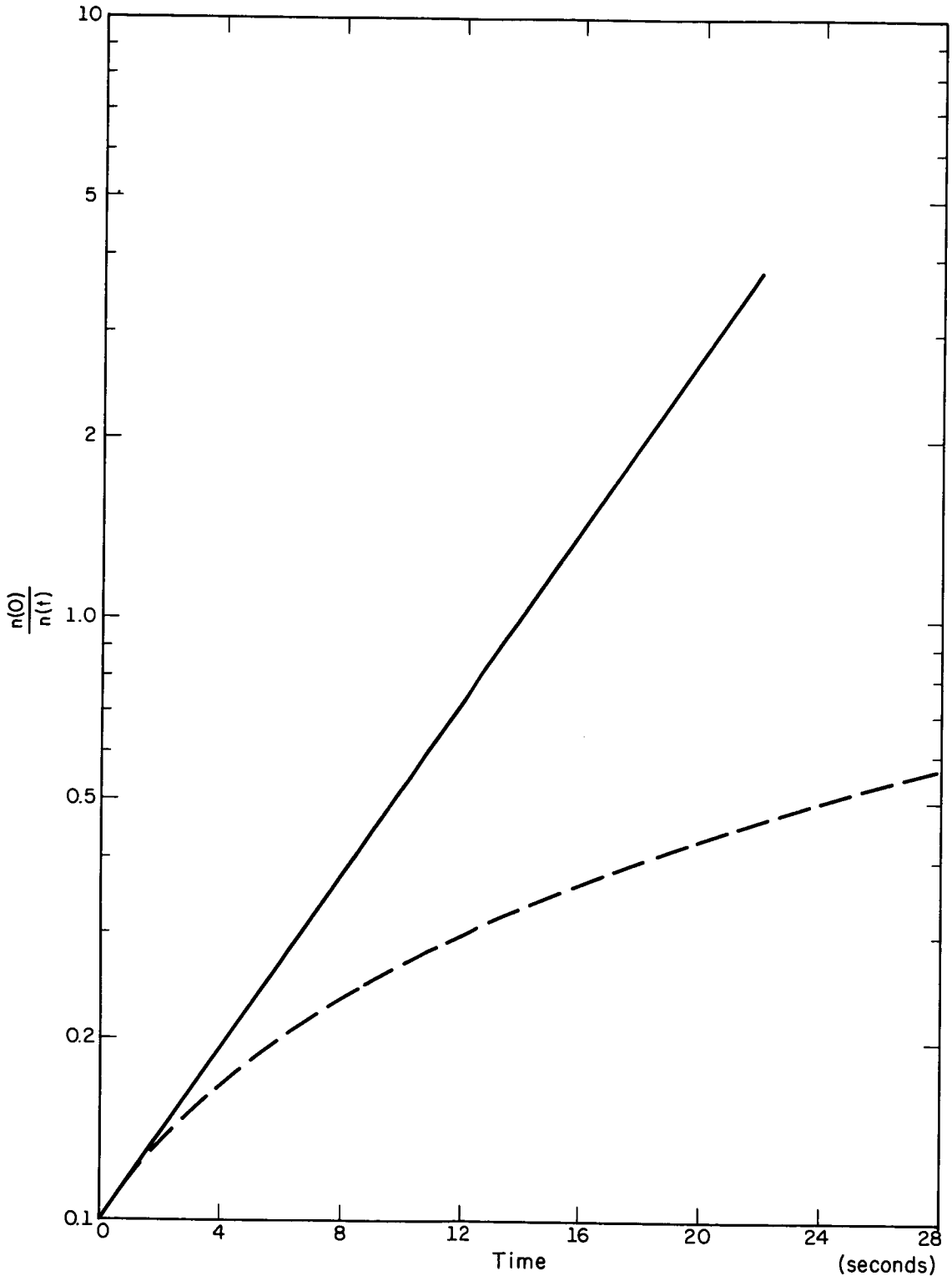

Figure 2. Logarithmic first order (——) and second order (- - - -) single state desorption rate curves with desorption constants as in Figure 1.

plotting the quantity

$$\frac{n(0)-n(t_1)}{n(t)-n(t_1)} = \frac{\text{amount of gas desorbed in } t_1 \text{ seconds}}{(\text{amount desorbed in } t_1 \text{ seconds}) - (\text{amount desorbed in } t \text{ seconds})} \qquad (6)$$

Here t_1 is a time sufficiently large for quasi-equilibrium to be established. This quantity varies from 1 to infinity as t increases from 0 to t_1. Analogously the quantity $n(0)/n(t)$ for simple state desorption increases from 1 to infinity as t goes from 0 to infinity.

We have performed numerical calculations of $n(t)$ for several distributions of adsorbed states and $t_1 = 20$ sec. Figure 3 shows plots of eq. (6) for E_j's equally spaced from 3.5 to 4.5 eV. For these calculations we have taken $\nu = 10^{13.0}$, near the experimental value for CO.[2] The first two curves are for all $n_j(0)$'s equal, with curve 1 corresponding to desorption at 1440°K and curve 2 corresponding to desorption at 1600°K. The steeply sloping parts of these curves at low times corresponds to the rapid desorption of the lowest energy (and therefore most easily desorbable) states. After this region of rapid desorption, both curves become simple exponentials. The slopes of these curves are related to the activation energy of the desorption taking place in this exponential region. Curve 1 only is shown extended beyond 14 sec so that the upward bend of the curve indicating the pole at $t_1 = 20$ sec is apparent. If t_1 is taken as longer than 20 sec, the linear portion of the curve is lengthened and

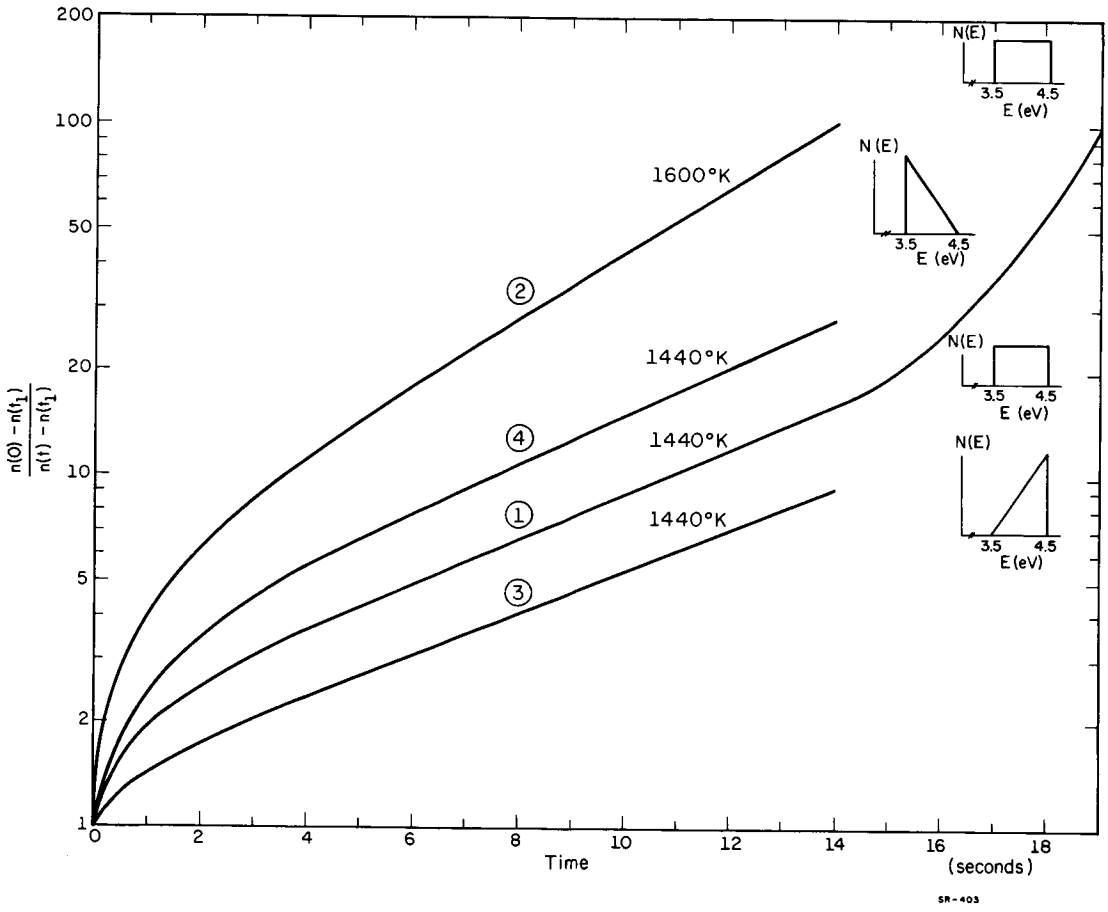

Figure 3. First order multiple state desorption curves for the temperatures and distributions of desorption energies shown. N(E) is the relative number of particles adsorbed at each energy E. $\nu_1 = 10^{13}$ sec^{-1}.

the slope decreases slightly. Qualitatively though, the form of the curve remains unchanged. Curve 3 shows the desorption that occurs at 1440°K. when the initial state density is

$$n_j(0) = j\, n_1(0) \ , \qquad j=1, ----, 10.$$

Since there are fewer molecules in the easily emptied low energy states, this curve does not rise so abruptly at low times. Curve 4 illustrates the desorption that occurs at 1440°K. when the initial state density is

$$n_j = (11-j)\, n_{10}, \qquad j=1, ---, 10.$$

Note that this curve rises more abruptly at low times than curve 3 or curve 1.

Similar curves for desorption from 10 independent second order states equally spaced in energy between 3.5 and 4.5 eV are shown in Figure 4. In this case, the variation of $n(t)$ with time is given by

$$n(t) = \sum_{j=1}^{10} \frac{n_j(0)}{1 + \frac{n_j(0)}{n(0)} [n(0)\ \nu']e^{-E_j/kT_t}} \ . \qquad (6)$$

We have chosen ν' so that $\nu = n(0)\ \nu' = 10^{13.0}$. Curve 1 represents a flat distribution of initial states. Curve 2 represents a distribution peaked, as above, at low energies, and curve 3 represents a distribution peaked, as above, at high energies. Each curve is for the

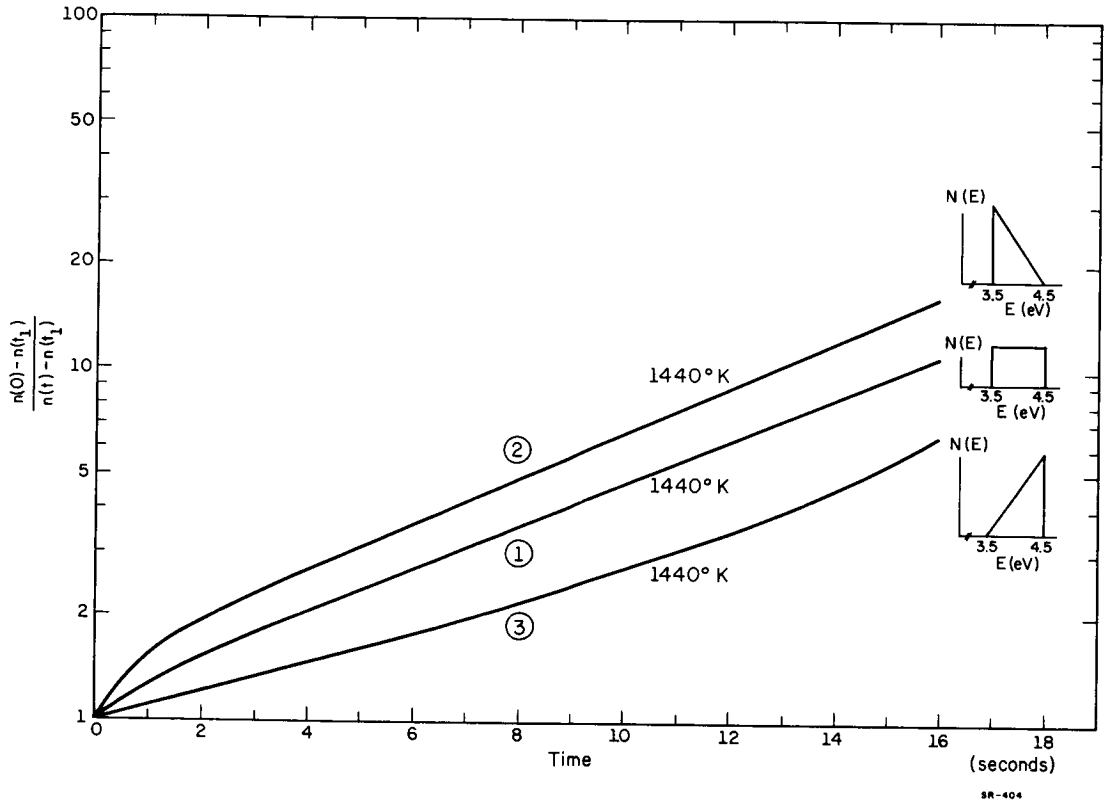

Figure 4. Second order multiple state desorption curves for the temperatures and distributions of desorption energies shown. N(E) is the relative number of particles adsorbed at each energy E. $N \nu_2 = 10^{13}$ sec^{-1}.

temperature equal to 1440°K. and t_1=20 sec. The increasing slope of curve 3 after 12 sec. is an artifact due to the small value of t_1. If t_1 is increased to 50 sec., the slope of curve 3 does not turn upward until about 35 sec.; moreover, it has a very small abrupt rise near the origin. It is clear that these curves are quite similar in form to those observed in first order multistate desorption, even possessing the same type of linear region.

It is common to assume that E is a function of the coverage[3], θ,

$$E(\theta) = E - \alpha\,\theta \qquad (7)$$

where

$$\theta = \frac{n(t)}{N} \quad ,$$

with N the saturation surface coverage in molecules/cm^2. Figure 5 shows two constant temperature second order desorption curves for $E(\theta)$ going from 3.5 eV at one monolayer to 4.5 eV for the clean surface. Curve 1 is for T=1440°K. and curve 2 is for T=1600°K. The desorption curves in this case are quite similar to those calculated for the uniform state distribution.

Thus, we have shown that desorption from first order multiple states, second order multiple states, and a second order state with coverage dependent energy yield very similar curves when plotted logarithmically as above. A simple first order state will be easily identifiable by a logarithmic plot. A simple second order state could

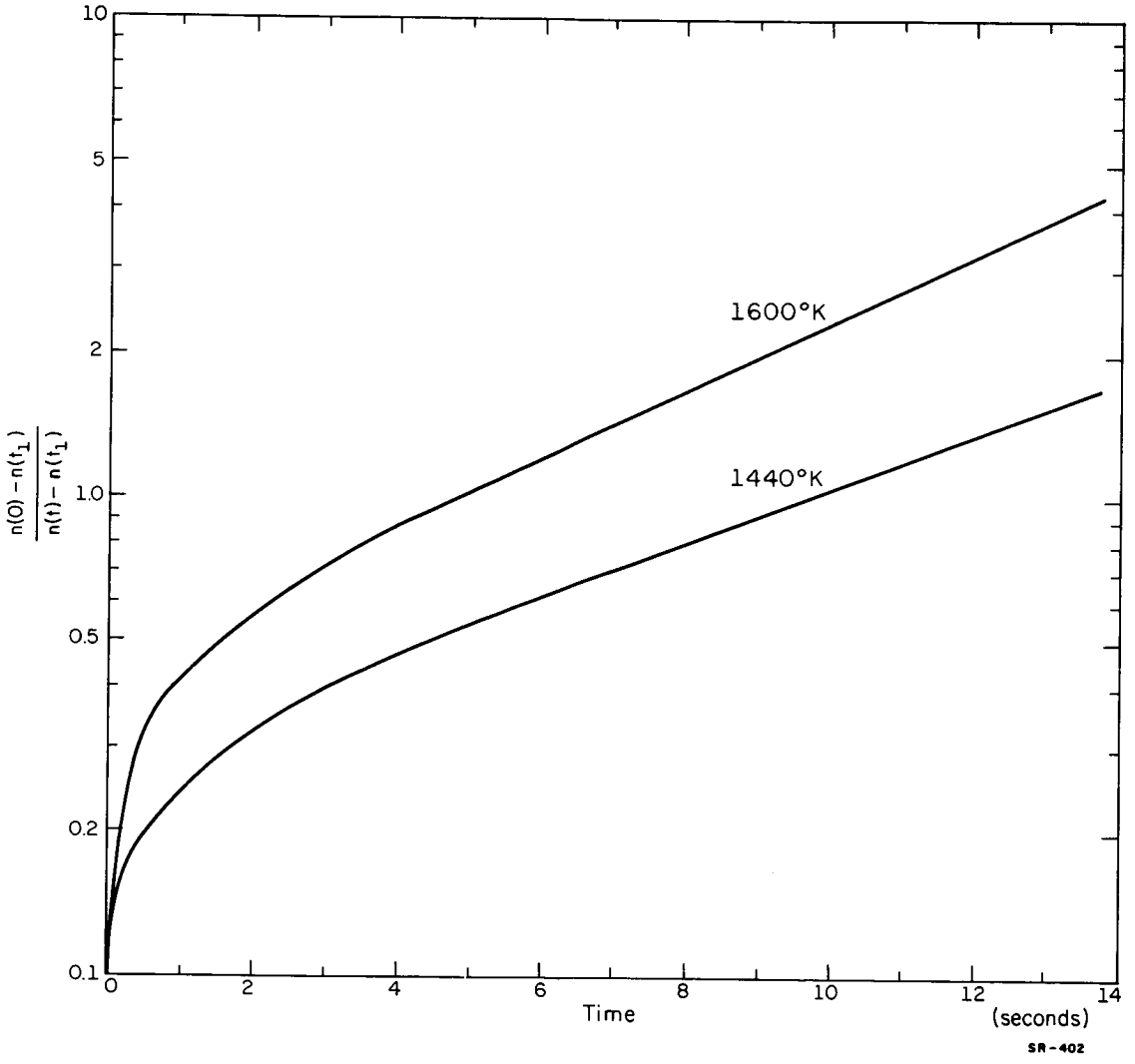

Figure 5 Second order desorption curves with $E(\theta) = E_o - \alpha\theta$, $E_o = 4.5$ eV, $\alpha = 1.0$ eV/monolayer, and $N\nu_2 = 10^{13}$ sec^{-1}.

more easily be detected by plotting $[n(0)-n(t)]/n(t)$ vs. t (eq. 4). Both types of simple state will be apparent in any experiment because of the consistency of $n(t_1)$ at different temperatures. The three types of desorption kinetics we have discussed which look similar on these charts are compared in Figure 6 for the case of identical adsorption energy ranges and desorption temperatures.

D. Conclusions

We have indicated that the order of desorption from a state with a single activation energy of desorption can be easily determined from n(t) at constant temperature. However, for multiple state desorption or desorption from a state with coverage dependent activation energy, the situation is substantially more complex, and the kinetics cannot be determined simply from the "shape" of the desorption curve at constant temperature. The failure to consider this problem must be considered a weakness in much of the published work on desorption.

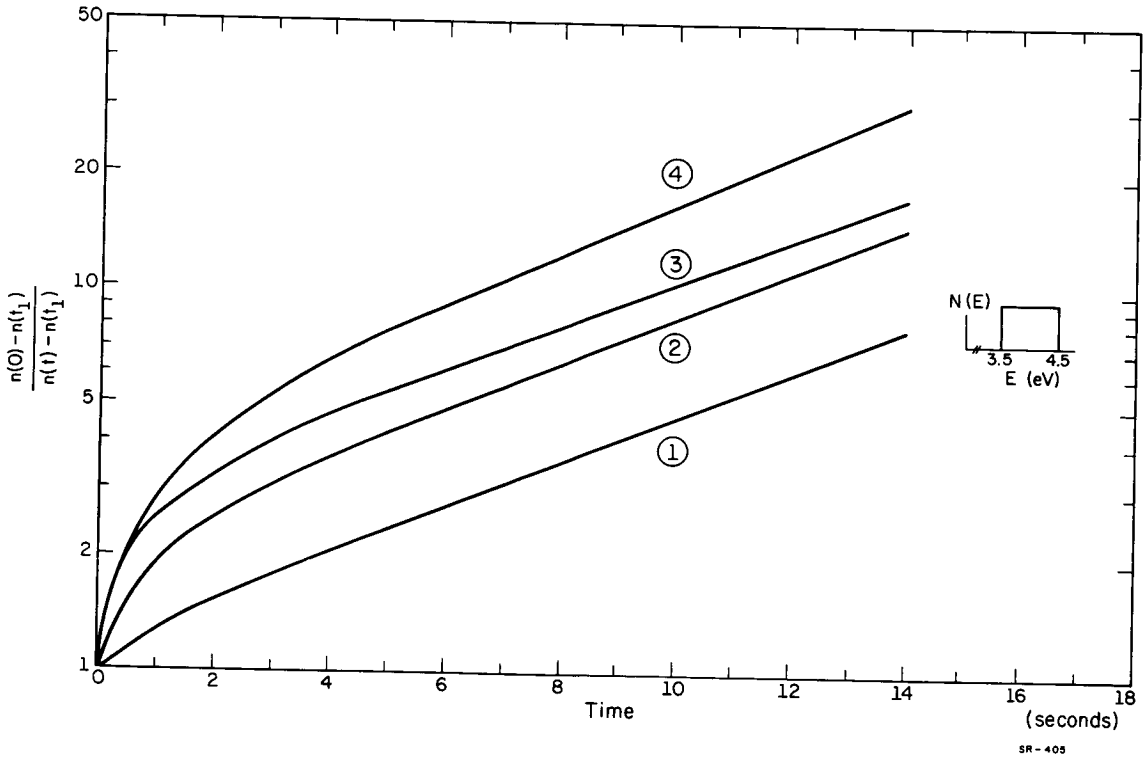

Figure 6. Comparison of four types of desorption curves with similar constants. Curve 1 corresponds to second order multiple state desorption and curve 2 corresponds to first order multiple state desorption, each having the state density pictured. Curve 3 is for the desorption energy decreasing with coverage (from Figure 5). The desorption temperature for these curves is 1440°K. Curve 4 is for desorption from the same set of states as curve 1, but at the higher temperature of 1600°K.

III. REVIEW OF DESORPTION STUDIES AND THE AUGER PROCESS

A. Introduction

The numerous techniques which have been applied to the study of the adsorption and desorption of gases on solid surfaces generally fall into two classifications.

The first type of experiment involves measuring pressure changes in a vacuum system and relating these to changes in the amount of gas adsorbed on the surface. One can observe a pressure decrease due to adsorption or a pressure increase due to desorption as the surface is heated. The latter technique, called the "flash filament" method, will be described in some detail in the next section both because it is one of the most powerful tools in desorption studies and because our work makes extensive use of it.

The second type of experiment measures the change in some property of the surface as gas adsorbs or desorbs. Desorption in these experiments may also be thermally activated and the energetics of the desorption process may be inferred from the rate of change of the property under observation. Some of the processes used in this type of study are low energy electron diffraction, field emission, field ionization, and work function changes. In subsequent sections of this chapter, these methods will be briefly discussed, indicating the type of information gained from each experimental method. The

last section of this chapter is a detailed discussion of the monitoring process used in this work: the Auger process (the potential ejection of electrons by ions). The emphasis of this discussion will be on the effect of gaseous adsorption on the Auger process and the current theory regarding this effect.

B. Flash Filament Method

Because of its relative experimental simplicity and the wide variety of information it can give on gaseous binding, the flash filament method is one of the most widely used surface tools. In a number of more comprehensive surface studies, this method is used in conjunction with other techniques, such as low-energy electron diffraction[4] and work function measurements.[5] Methods of analysis and the limitations of flash filament experiments have been discussed by Ehrlich[6,7] and Redhead.[8]

In a typical flash filament experiment, adsorbable gas is leaked into the vacuum chamber at a rate F ($\frac{\text{Torr liter}}{\text{sec}}$). Assuming the chamber is pumped at a constant speed S ($\frac{\text{liter}}{\text{sec}}$), the equilibrium pressure p_o will be

$$p_o = F/S. \tag{8}$$

The surface or "filament" to be studied is then cleaned by heating. After the filament cools, gas will adsorb until the surface

chemical bonds are saturated. The rate at which gas molecules of mass M and temperature T bombard unit surface area is given by kinetic theory to be

$$r = \frac{P_o}{(2 \pi MkT)^{1/2}} \tag{9}$$

where k is the Boltzmann constant.

The sticking coefficient, s, is defined by

$$s = \frac{dn/dt}{r} , \tag{10}$$

and the total number of gas molecules which strike the surface in time t is the exposure, E; so that

$$E = rt \left(\frac{\text{molecules}}{\text{cm}^2}\right) . \tag{11}$$

In this work we usually give this quantity in units of Langmuirs, L, where

$$L = 10^{-6} \text{ Torr sec.}$$

For N_2 at 300°K L corresponds to 3.83×10^{14} molecules/cm^2.

When sufficient time has elapsed for the coverage to reach the value at which desorption is to be studied, the filament is heated again, this time according to a specific temperature schedule. As the temperature rises, gas molecules begin to leave the filament at a rate $[-dn(t)/dt] \left(\frac{\text{molecules}}{\text{cm}^2\text{sec}}\right)$. Under these conditions the pressure, p, is given by

$$V\frac{dp}{dt} = F - pS - KA\frac{dn(t)}{dt} , \qquad (12)$$

where V is the vacuum system volume, A the filament area, and K^{-1} is the number of molecules per Torr liter at the gas temperature, or 3×10^{19} at room temperature. Actually, the right hand side should include a negative term allowing for adsorption of gas during the heating cycle, but this can be shown to be relatively small in most cases.

Letting $p' = p - p_o$, equation 12 becomes

$$\frac{dp'}{dt} - \frac{p'}{\tau} = -\frac{KA}{V}\frac{dn(t)}{dt} \qquad (13)$$

where τ is defined as V/S. Thus, n(t) may be obtained directly from pressure measurements. In particular, if the temperature of the filament is increased sufficiently slowly, so that

$$\frac{p'}{\tau} >> \frac{dp'}{dt} ,$$

equation 13 becomes

$$\frac{-dn(t)}{dt} \simeq \frac{V}{KA\tau} p' . \qquad (14)$$

In this case, the desorption spectrum (pressure vs time record) for the desorption of widely separated sets of energy states consists of widely separated pressure peaks. The number of atoms, n, adsorbed in each group of states can be found from the area under the corresponding maxima of the pressure curves;

$$n = \int \frac{dn(t)}{dt}\, dt = -\frac{V}{KA\tau} \int p\,dt. \qquad (15)$$

To relate n to the binding energy of an adsorbed molecule, knowledge of the actual kinetics of desorption is required. If, for example, we have simple first order desorption and a linear temperature sweep

$$T = T_o + bt\ , \qquad (16)$$

the desorption energy may be obtained from the temperature, T_D, at which the desorption spectrum peaks[8] by differentiating eq. (1). Thus,

$$E = kT_D \left[\ln\left(\frac{T_D\,\nu}{b}\right) - \frac{kT_D}{E_D}\right]. \qquad (17)$$

Since in cases of interest the factors in the argument of the logarithm vary only slightly compared to $\frac{\nu}{b}$, this equation is nearly a linear relation between E and T_D. Therefore, with this technique, measurements may be made of the amount of gas adsorbed on the surface, the energy with which it is bound, and the probability of adsorption of an incident molecule.

Recent advances in the art of pressure measurements have ameliorated many of the experimental difficulties faced by earlier investigators. With the advent of the new family of mass spectrometers, it is possible to observe the behavior of each gaseous species within the vacuum, partially insuring against errors due to gaseous interactions. Low temperature cathodes in these spectrometers

decrease the likelihood of reactions with the filaments. The major drawback to this method is that it has proved difficult to measure the kinetics of desorbing gases with good accuracy.

C. Electron Diffraction

Low-energy electron diffraction (LEED) studies have provided unique information about the configuration of gases adsorbed on single crystal surfaces.

Electrons having low enough energy so that their wavelengths are comparable to the lattice spacing will be diffracted before they penetrate more than the first few surface layers. The resulting diffraction patterns for clean surfaces are reasonably well understood, since they are comparable to X-ray Laue patterns for the bulk material. However, adsorption of some gases gives completely different patterns which are often more difficult to interpret. The new patterns are occasionally attributed to the rearrangement of the atoms of the substrate,[9] but usually they are found to correspond to the superposition of a regular grid of adsorbed atoms over the substrate.[10] This grid may change structure several times during the adsorption process. For instance, in the adsorption of O_2 on (100) Ni, the first noticeable spots due to O_2 adsorption are attributed to a superposed grid corresponding to .10 atoms per Ni surface atom. Continued adsorption results in rearrangements on the surface down through .25 and .50 oxygen atoms per Ni surface atom.

Though electron diffraction experiments can give detailed information in some cases, they are by no means universally applicable. Light adatoms, such as H, have such a small electron scattering cross section that diffraction spots are sometimes not visible.[10] Moreover, LEED patterns cannot generally be related to a unique surface structure, leaving an element of indeterminancy in all interpretations.

By observing the change in these LEED patterns as the surface is heated, desorption activation energies can be measured.

D. Field Emission

Field emission experiments have provided information about adsorption on single crystal planes and diffusion across single crystal surfaces.[12]

A uniform, very small hemispherical "tip" of the metal to be tested is required. The electric field on the rounded edge of this point is approximately that on a sphere. If a negative potential V is applied to a sphere of radius r within a concentric conducting sphere, the field at the interior surface is

$$E = \frac{V}{r} \quad . \tag{18}$$

Therefore, E may become very large for small r. If the tip is made small enough so that E approaches .3 V/A°, electrons can tunnel directly out of the conduction band and be accelerated linearly toward a fluorescent screen. The brightness of each area of the

screen will be indicative of the relative magnitude of the work function of the portion of the tip from which the electrons originate. By measuring the current voltage relationship of this emission, the work function can be calculated using the Fowler-Nordheim equation.

Adsorbed gases alter the work function of the surface on which they are bound and hence, can be detected and studied by use of the Field Emission Microscope.

Migration is studied by depositing adsorbable gases on one side of the tip with under good vacuum conditions. Gradually increasing the temperature for fixed periods of time gives the activation energy for diffusion. Heating the tip until clean surfaces entail allows measurement of desorption energies.

E. Field Ionization

Thus far the field ion microscope, in spite of having a greater resolution than the field emission microscope, has not yielded a great deal of information about adsorption.[13]

In the field ion microscope, atoms, usually of the noble gases, are polarized and attracted by the strong electric field near a metallic tip. When the atoms strike the positive tip, the field of $\sim \frac{2V}{A^\circ}$ is great enough to strip off outer electrons, so that the ions are repelled from the tip. As the ions strike a fluorescent screen, a pattern showing on which areas of the tip the rate of ionization is highest becomes visible. In some cases, individual surface atoms are recognizable.

Because of the large fields required, no adsorption is possible during the ion imaging. If the field is applied after gas has been allowed to adsorb, the field alone will quickly break all but the strongest chemisorption bonds. For this reason, this method can be used to study O_2 adsorption in some cases.[14]

F. Other Methods

Many other methods are based on detecting work function changes during chemisorption. These range from the photoelectric method[15] to the vibrating reference surface (Kelvin) method.[5] However, the evidence they produce is indirect. This method is chiefly useful only when coupled with other studies.

The method of isotope mixing has been useful in determining whether diatomic molecules are dissociated on adsorption.[16, 17]

Tables I and II summarize recent data on the binding of H_2, N_2, and CO on the tungsten surfaces studied in the present work.

G. Auger Review

The potential or Auger ejection of electrons by ions at metal surfaces has been studied for some years, both theoretically and experimentally. Oliphant and Moon[23] were first to suggest that the tunneling of a metallic electron into an excited ion level, called resonance neutralization, followed by de-excitation into the neutral ground state, could account for the high energy secondaries observed.

TABLE 1. Adsorption of H_2 and CO on W Near Room Temperature

	H_2				CO								
State	α	β	α	β	α	β_1	β_2	β_3	α	β_1	β_2	β_3	
Order	2	2	1	2	1		1						
N	4		4			4.5			1.1	3.6			
E	1.53	1.05	1.35	.87	.87		3.26	4.35	1.0	2.74	3.35	3.91	
ν	2.10^{-3}		5.10^{-3}				3.10^{13}						Poly-crystal
s					.5								
Ref.	Mimeault and Hanson[17]		Hickmott[18]		Ehrlich[21]					Rigby[22]			
State													
Order													
N													
E													(111)
s													
Ref.													
State									α	β_1			
Order									1	1			
N									5.6	7 ?			
E									1.0	2.61			
s									1.0				(110)
Ref.									May and Germer[4]				

E is given in eV, ν in sec^{-1} or sec^{-1} $molecule^{-1}$, N in 10^{14} molecules/cm^2.
?: Normalized on the basis of s=1.2.

TABLE 2. Adsorption of N_2 on W

State	α	ξ	η	α	β_{21}	β_{22}	β_1	α	β_1	β_2	
Order	2	1	2		1	2	1		1	2	
N	.12	.65	.75		.375	.375	2.25		3		
E	.78	3.65	3.00		3.87	3.57	3.48		3.17	3.26	Poly-crystal
ν					10^{13}	.014	10^{13}				
					(Trial Model)						
s	.2										
T	300°K					300°K			300°K		
Ref.	Oguri[19]					Madey and Yates[16]			Rigby[20]		

State	γ	α	β_1	β_2	
Order		1	2		
N		.89	(75%	25% of β)	
E	.39	.70	3.52	3.87	
s		.007			(111)
T		110°K			
Ref.	Ehrlich and Delchar[5]				

State	γ
Order	2
N	
E	.39
T	110°K
Ref.	Ehrlich and Delchar[5]

(110)

T is the adsorption temperature.
E given in eV, ν in sec^{-1} or sec^{-1} $molecules^{-1}$, N in 10^{14} molecules/cm^2.

These high energy secondaries would be excited by an Auger process (called Auger de-excitation) directly from the conduction band. This two step process is pictured in Figure 7 for electrons 1 and 2.

Pertubation calculations of this effect were made by Cobas and Lamb,[24] and Shekhter.[25] Shekhter was first to recognize the possibility of the direct neutralization of the ion to the ground state by a conduction band electron, with a second conduction band electron receiving the excess energy (Figure 7, electrons 1' and 2). This process is called Auger neutralization.

Varnerin[26] extended the theory by closely examining the relevant energy balances. For instance, for the case of He^+ bombarding W, the system used in this work, he showed that in the region of high transition probability the image forces acting on an incoming He^+ ion are sufficient to lower the initial energy of the tungsten + He^+ system below the energies of all possible resonance states. Therefore, resonance neutralization is rendered energetically impossible, and Auger neutralization is the only process by which low energy He^+ ions are neutralized on tungsten.

These Auger and resonance processes are surface phenomena and are unusually sensitive to contamination. Therefore, really consistent experimental results were not available until the development of modern ultra-high vacuum technique. The experimental work of Hagstrum is especially notable, as he studied the neutralization of

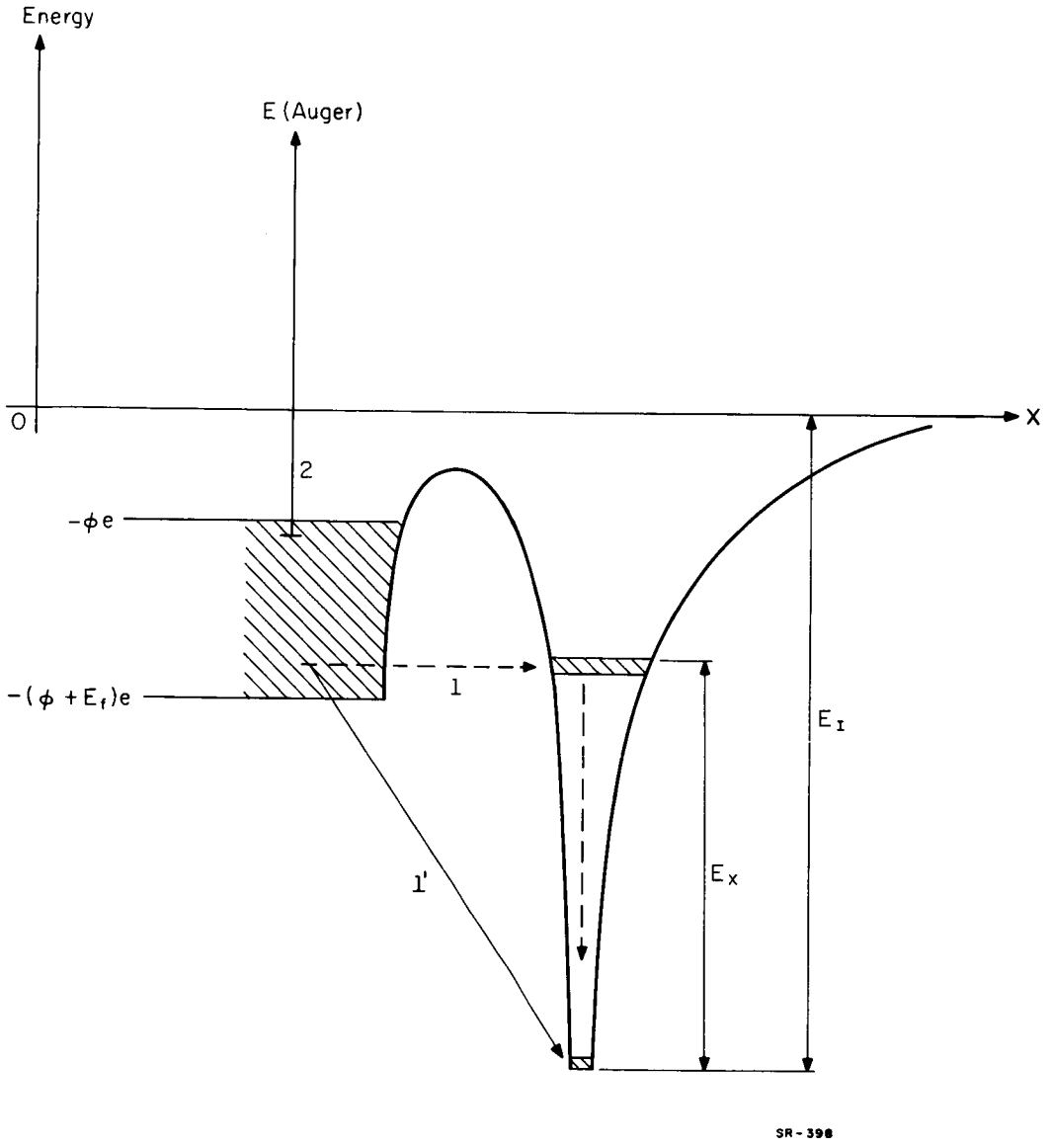

Figure 7. Schematic illustrating an ion being neutralized at a metal surface.

noble gas atoms on W,[27,28] Mo,[29] Ta,[30] Si,[31] and Ge.[31] Hagstrum also expanded previous theory by developing phenomenological models which incorporate the effects of the escape probability for excited electrons,[32] the specific shape of the conduction band,[33] and atomic level broadening.[32] Hagstrum also first studied the effects of specific adsorbed gases on Auger neutralization.[34] He found that chemisorption of the diatomic gases N_2, H_2, and CO on W, monotonically decreased Auger yield for both He^+ and Ne^+ by as much as 40%. Auger yield, γ, is given by

$$\gamma = \frac{\text{electrons ejected}}{\text{incident ions}} \quad . \tag{19}$$

The plots of yield versus coverage have a clearly detectable slope change at the point where the surface has one monolayer of adsorbed gas on it (Figure 8). Moreover, the maxima in the energy distributions of Auger electrons consistently shift to lower energies as gas adsorbs (Figure 9).

Hagstrum considered several mechanisms which might account for these changes. He showed that the large change in yield could not be attributed solely to the work function change upon adsorption. The width of the electron distribution secondary to He^+ is 16 eV, far too broad to be affected so much by shifting the work function by less than 1 eV. Hagstrum also considered the possibility that the presence of adsorbed particles on the surface would alter the Auger yield by their effect on the atomic energy levels. He concluded that

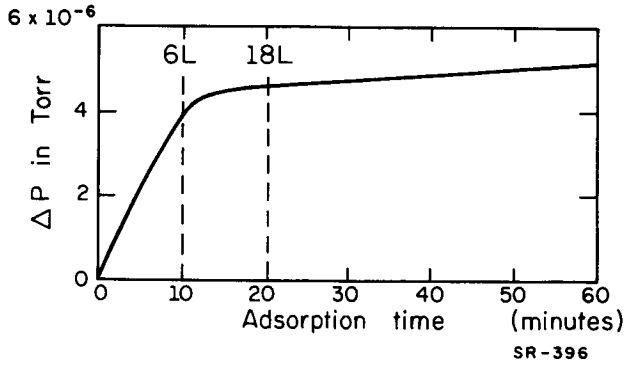

Figure 8a. Pressure rise upon target flash plotted against time of exposure to CO. The target is polycrystalline tungsten and the pressure and temperature are as below.

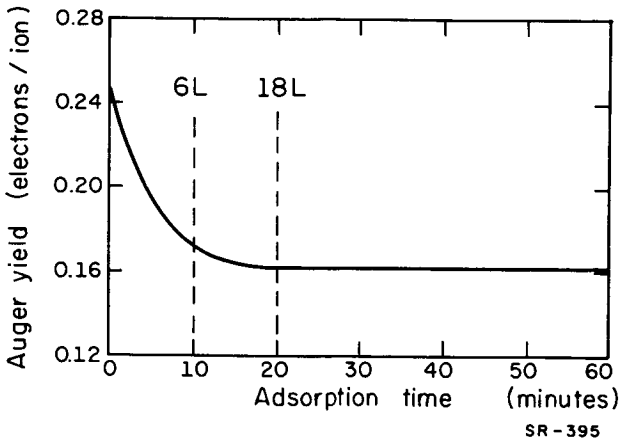

Figure 8b. Decrease in yield of 200 eV He^+ on polycrystalline W at room temperature with exposure to 2.1×10^{-8} Torr of CO (Hagstrum[34]). During the first part of the adsorption curve, the target pumps strongly and reduces the pressure to 1×10^{-8} Torr. Our estimate of the exposure in Langmuirs is marked on the abscissa.

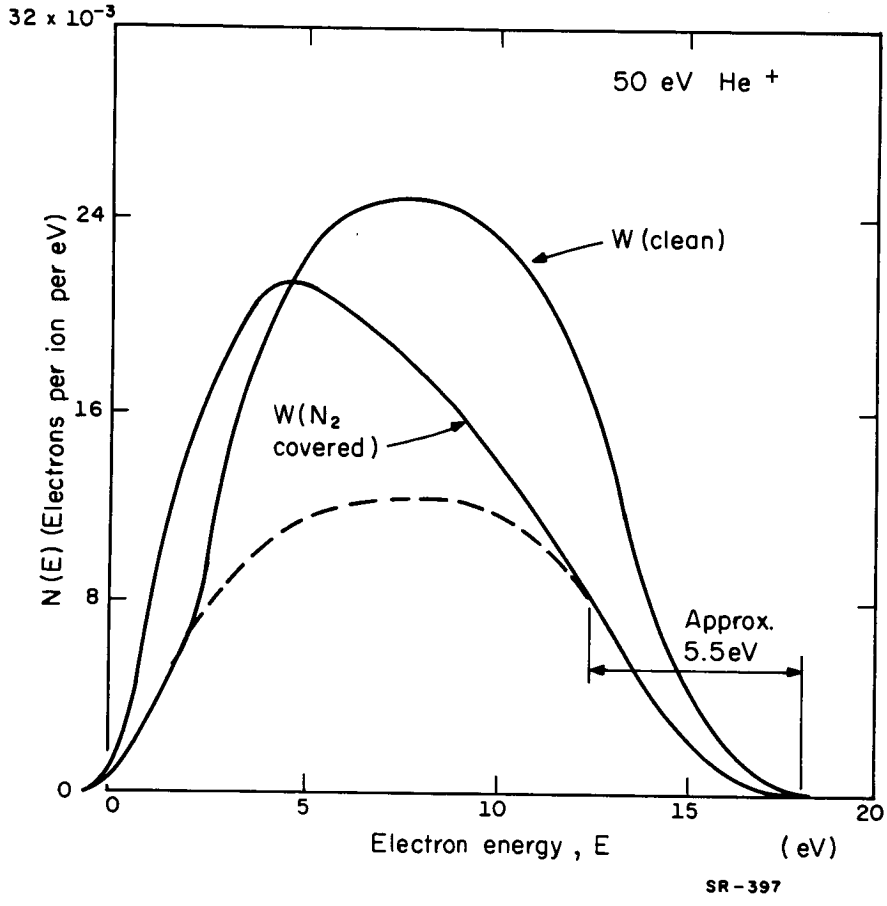

Figure 9. Comparison of Auger electron energy distribution for clean polycrystalline tungsten and tungsten covered with 1 monolayer of N_2. The broken curve is 0.5 of the distribution for clean W (Propst and Luscher[36]).

this could not explain the observed behavior.

Propst and Luscher[36] developed a model for the alteration in the Auger yield change and energy distribution with surface coverage. They assumed that some of the Auger electrons could be inelastically scattered by surface states induced by adsorbed atoms. These surface states were assumed to have excited levels at an energy W above the ground state. Therefore, Auger electrons could lose a minimum amount of energy, W, during inelastic collision with the localized states, and no electrons which have inelastically scattered could be present in the energy distribution between E_{max} and E_{max}-W (the 5.5 eV range in Figure 9). Assuming that the scattering cross section is not a strong function of energy, this model requires that the covered surface energy distribution be proportional to the clean surfaces distribution between these two energies. Propst and Luscher found this to be true for each of the adsorbed layers studied, and were able to approximate the complete energy distribution for the covered surface from the clean surface energy distribution and the fractional scattering from the high energy tail.

Later Hagstrum[37] postulated another mechanism which attributed the change in yield with adsorption to the creation of a band of adsorbate electronic states which partially overlaps the conduction band as in Figure 10. This band of adsorbate states would have its highest energy states below the Fermi level of the metal. Since the

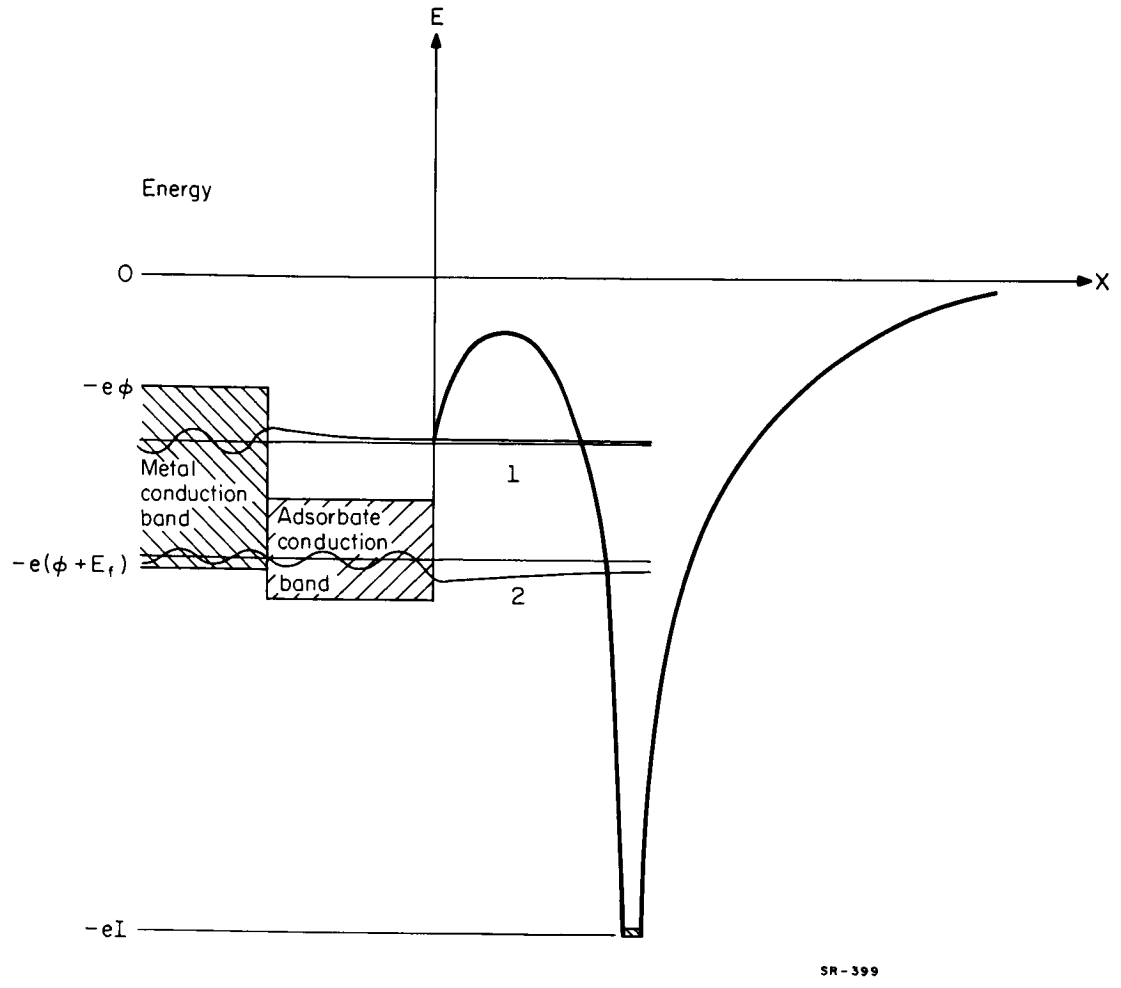

Figure 10. Schematic illustrating the relative values of electronic wave functions at the ion core. The energy of conduction band electron 1 does not lie in the band of adsorbate states. The energy of conduction band electron 2 does lie in the band of adsorbate states.

probability of the Auger transition is proportional to the probability that a conduction band electron can penetrate to the ion, the electron with energy low enough to be conducted through the adsorbate will have a much higher likelihood of undergoing an Auger (or resonance) neutralization. Thus, the number of high energy secondaries would be reduced. Another effect altering the energy distributions of this model would be the relative growth of processes involving electrons of lower energy from the surface band. Hagstrum has published no calculations in support of this model.

In a general discussion of the uses of the study of Auger processes, Hagstrum suggested its use as an indicator for surface coverage.[38] Using Auger yield measurements, Hagstrum[39] determined the sticking coefficient of O_2 on Si and Ge. He also determined its approximate desorption temperature by successively heating to higher temperatures and then measuring the Auger yield at the end of the heating period. He repeated this until the clean surface yield was obtained.

In summation, the experimental results of Hagstrum lead us to expect that the change in Auger yield with adsorption will be roughly proportional to coverage. It is easy to see that the scattering theory of Propst and Luscher will predict that this proportionality will hold if the scattering cross section is independent of coverage. Suppose n(0) molecules are initially adsorbed on the surface and lower the Auger yield by an

amount $\Delta\gamma_o$. If molecules are desorbed from the surface until the coverage is reduced to $n(t)$ and the corresponding yield change reduced to $\Delta\gamma$, then, to the approximation of contant cross section,

$$\frac{n(t)}{n(0)} = C \frac{\Delta\gamma}{\Delta\gamma_o} \quad , \tag{20}$$

where C is a constant near unity. Thus, the equations derived for different types of desorption kinetics in Chapter I would be as valid for $C \frac{\Delta\gamma}{\Delta\gamma_o}$ as they are for $\frac{n(t)}{n(0)}$. Therefore, we would hope to be able to distinguish the kinetics of the desorption of individual states by measuring change in yield with time using methods analogous to those of Chapter I. However, as the coverage increases to the point where the electronic orbitals of the adsorbate molecules begin to interact, we would expect the scattering cross section to change. Thus, the approximation indicated above is probably valid only at low coverage. Furthermore, we would expect different adsorption states to exhibit different scattering cross sections. In any case, it is reasonable that over small regions of Auger yield change the approximation of eq. 20 may be used. We shall consider this point further in the discussion of our experimental results.

IV. APPARATUS

A. Motivation for this Experiment

A thermal desorption experiment designed to measure changes in Auger yield and relate these to changes in coverage has certain distinct advantages. Primarily, the experiment can continuously measure the total gas coverage on a macroscopic sample in one small area of the surface under various conditions of temperature and pressure. By careful construction, the temperature gradient can be made very small across this point so that for reasonable values of diffusion coefficients of adsorbed molecules, effects due to diffusion will not be present. Since Auger yield can vary by a factor two or so when the coverage varies from 0 to 1, the relative sensitivity of this method is quite high in many cases. Such an experiment can yield different and complimentary information as compared to other methods, since it is not keyed to pressure or work function changes, but to a different type of electronic interaction.

In this experiment a different type of heating schedule can be used. As we have already said, it would be most interesting to study the desorption equation (1) at constant temperature. This can be accomplished by recording the response of the secondary electron current to step function temperature increments. Analogous methods have not been too successful when applied to flash filament experiments.

B. General Description

An experiment of this type requires an ultra-high vacuum system. In order to perform experiments lasting 500 sec on surfaces less than 5% contaminated by the residual gases in the system, the residual gas pressure must be less than 1×10^{-9} Torr. Even under these conditions, adsorption characteristics at very low coverage and constant temperature cannot be accurately measured because of the time required for the target to reach temperature equilibrium.

The surface to be studied must be mounted so that its temperature can be measured and controlled. Because of its relative ease of cleaning, we have chosen tungsten for our target material and heated it ohmically.

Simultaneously, the target must be bombarded by a beam of low energy ions. If the total secondary electron current is Ie and the ion current striking the target I_i, the Auger yield γ is

$$\gamma = \frac{I_e}{I_i} \quad . \tag{21}$$

Since the target is ohmically heated during most of the experiment, it will be difficult to measure I_i at the target. Therefore, in order to facilitate the measurement of γ, it will be necessary to hold the ion current constant in the ion source itself. In this case, the secondary electron current is proportional to the yield. We chose to use He ions since He^+ has a large Auger yield on tungsten because of its large ionization potential. Furthermore, He does not adsorb on

tungsten. Finally, the secondary electron current must be collected and measured. A block diagram for this system is shown in Figure 11. Each of the components of this system are described in greater detail in the following sections.

C. Vacuum System

The stainless steel vacuum system shown in Figure 12 was constructed for this experiment. The oil diffusion-pump (NRC HK-750), using DC-705 silicone-base pumping fluid, produces an ultimate pressure of about 3×10^{-10} Torr (approximate nitrogen equivalent) in the vacuum chamber. The liquid nitrogen trap (Granville-Phillips 6" Cryosorb) was never allowed to warm up during the course of the experiment. The water baffle was installed when it was discovered that the pumping fluid was contaminating the target.

RCA feedthroughs were used to provide the voltages for the ion source, grid, and secondary electron collector. A specially constructed glass and hollow Kovar tube feedthrough was used as a thermocouple feedthrough. Ceramic and Kovar feedthroughs made by the Alberox Corp. were used to support and insulate the target cooling reservoirs.

D. Ion Source

A diagram of the cylindrically symmetric ion source is shown in Figure 13. All electrodes are made of stainless steel and are

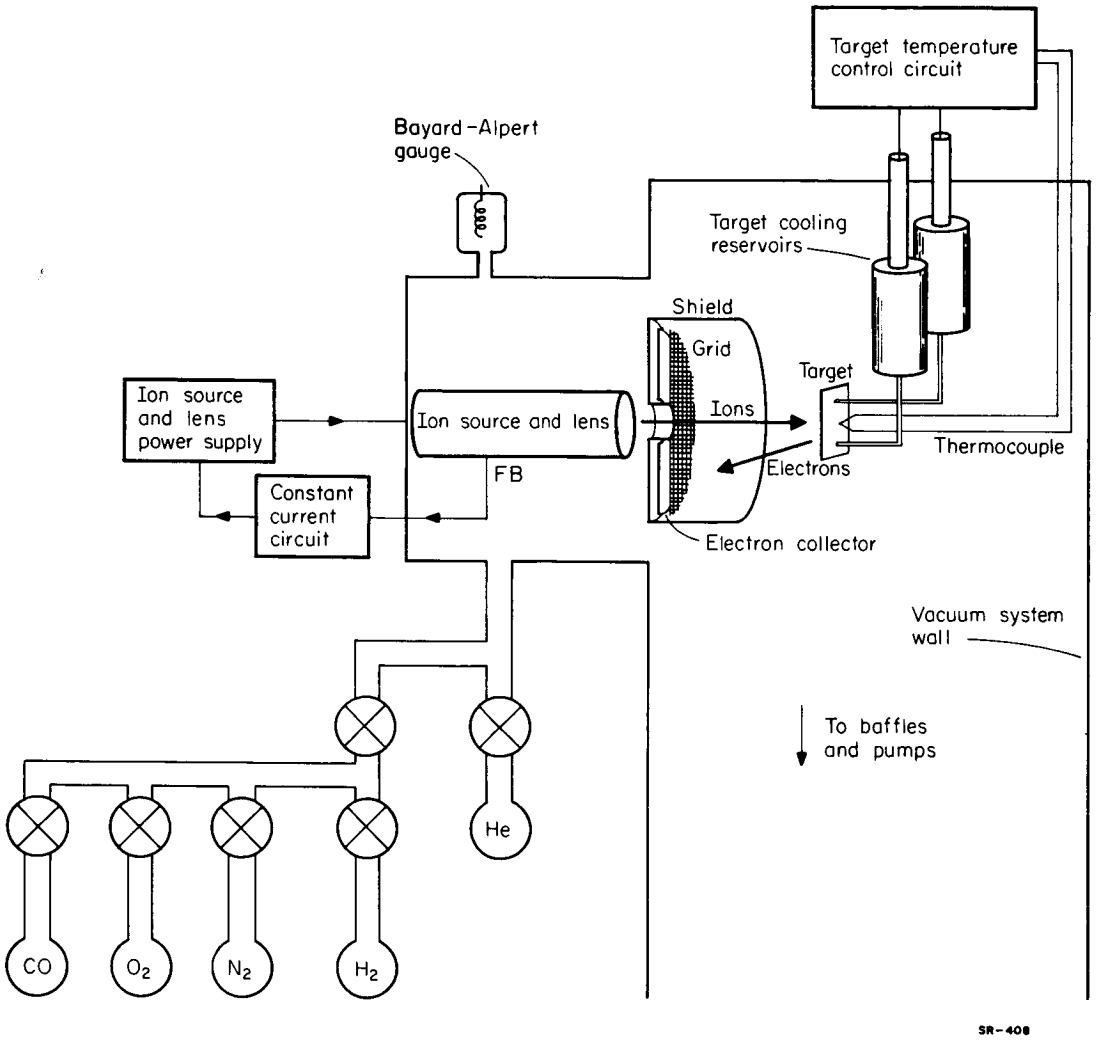

Figure 11. Schematic of the apparatus.

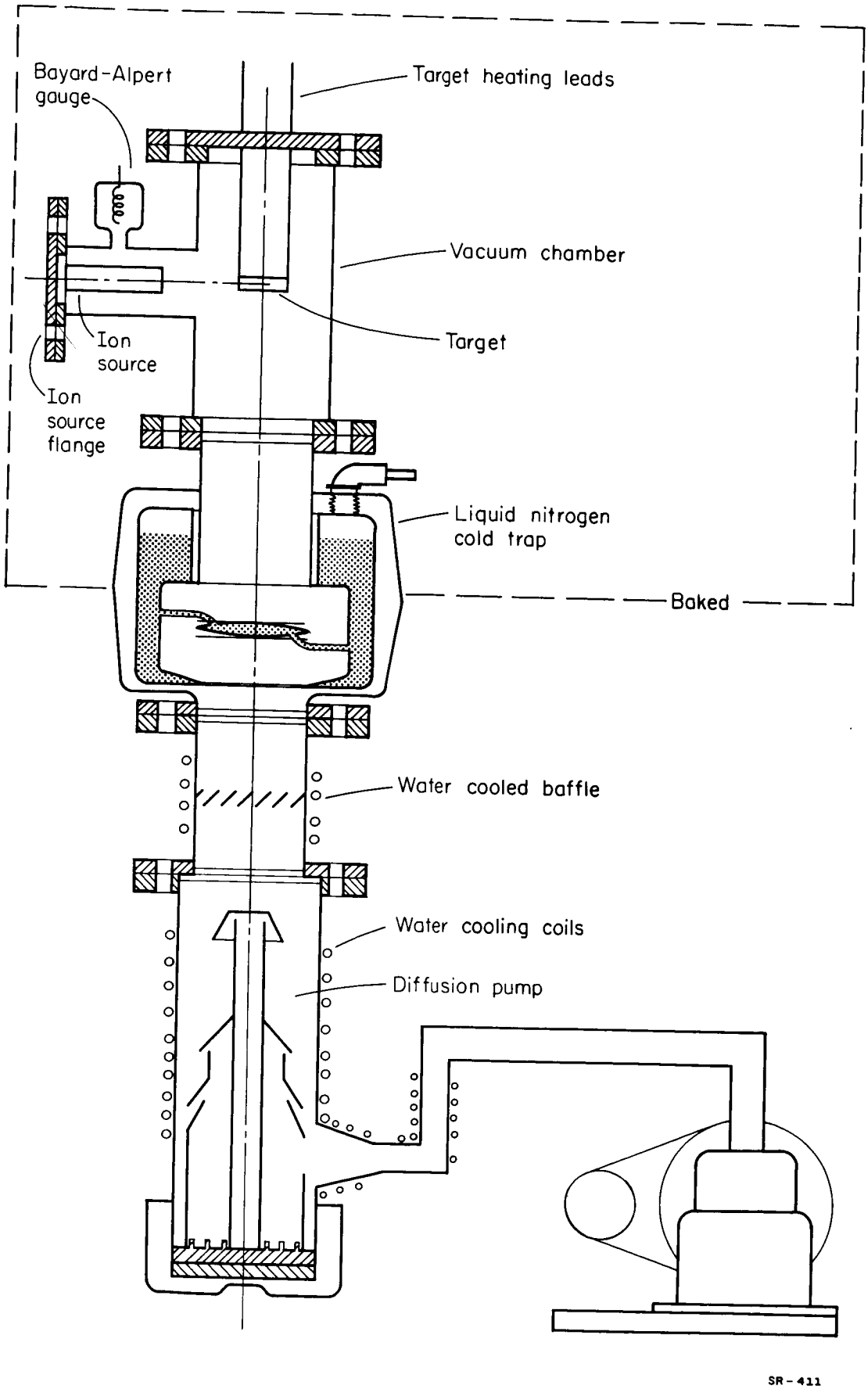

Figure 12. Diagram of the vacuum system.

Electrode	IC	V_1	V_2	V_3	FD	FA	FB	K	L	F
Aperature diameter (cm)	.64	.32	.47	.32	1.59	.32	.1	1.59	1.59	
Voltage	103	99	95	99	95 +15 V square wave	20	0	84	0	16

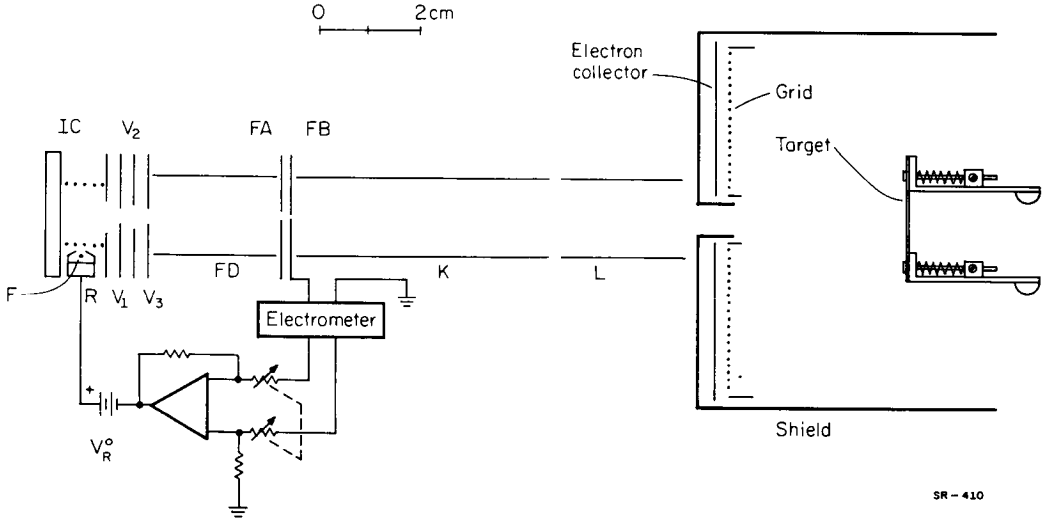

Figure 13. Ion source schematic including lenses, target mounting system, electron collector, and current control circuit. The electrometer is a Keithley 410 picoammeter, and the operational amplifier is a Philbrick P65AU.

mounted on four alumina rods. These rods are held by spring clamps screwed to the ion source flange, and the electrodes are positioned by alumina spacers telescoping over the alumina rods.

Ions are formed by electronic impact with He atoms inside the wire-cage, ionization chamber IC, and are drawn into the focusing systems by a small electric field applied with electrode V1. Electrodes V1, V2, and V3 comprise, approximately, an Einzel lens which focuses the ions onto the aperture system FA and FB, at the end of a relatively low field region FD. By making the voltage on FD larger than that on IC, the ion beam can be completely retarded out.

The purpose of the aperture FA is to screen off the nonparaxial ions from FB so that the current striking FB will be directly proportional to the current transmitted by FB. Since these electrodes are located at the crossover point of the ion focusing system, their potentials are of only secondary importance for focusing.

Ions passing through the aperture system are focused by the co-axial cylindrical accelerating lens K-L onto the target. The image size on the target can be determined by deflecting the beam across the target with the split-cylinder, L, while measuring the ion current to the target. The shape of these curves indicates that the image is about 1 mm in diameter, much smaller than the 1/4" target width. This is consistent with the fact that the co-axial cylinder lens images a 1 mm aperture and has a calculated magnification of .75.

A system which has been constructed to hold the ion current constant in spite of pressure and emission current fluctuations is also shown in Figure 13. This system holds the ion current to FB constant by controlling the potential of the electron focus electrode, V_R. The potential of R controls the emission current from the filament F and the trajectories of the electrons as they enter the ionization chamber; hence, it controls the total ion current. A plot of this relationship is shown in Figure 14.

When the ion source is operating in the feedback mode, say at operating point P corresponding to a current of 1×10^{-9} A and electron focus potential 0 V, an increase in ion current causes an increase in the electrometer output voltage. Thus, a larger voltage is applied to the negative input of the operational amplifier, pushing the amplifier out of its balanced state and giving a negative instead of a zero output voltage. This negative voltage will drop the focus electrode potential from its steady state value thereby reducing the ion current and bringing the amplifier back into balance. A decrease in ion current will produce the convere result.

This system holds the current intercepted by FB constant. Because of the slight focusing action near this electrode, the current transmitted by FB is not exactly proportional to the current intercepted by FB. It is at times difficult to adjust the potentials in this region and the amplifier gain so that good operation is insured. However, we have been able to hold the ion current to the target to within 1% for many

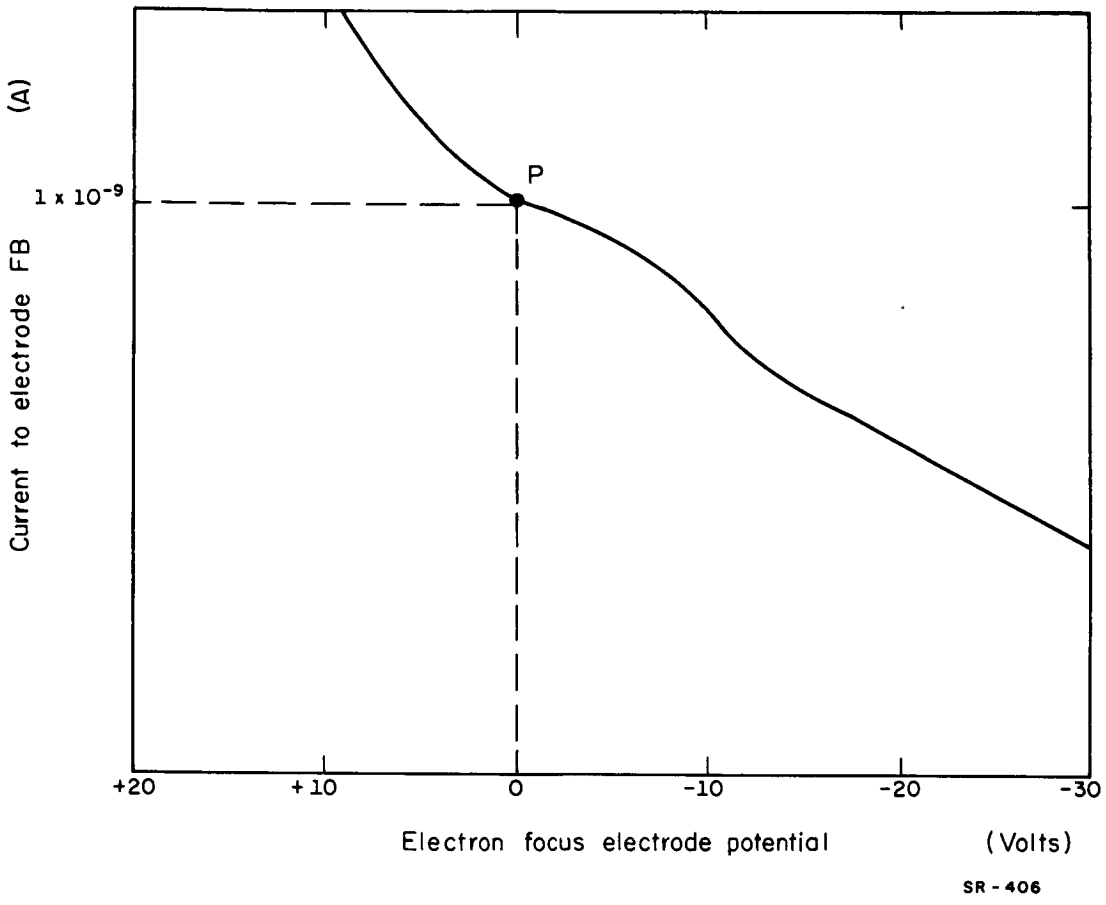

Figure 14. Ion current vs. electron focus electrode potential, V_R. P is a typical operating point.

hundreds of seconds.

E. Grid and Collector

The grid and electron collector are mounted in a separate assembly, as shown in Figure 15 and in schematic form in Figure 3. All electrons emitted at the target with trajectories between 12° and 47° of the target normal are collected if there are no retarding voltages. If the electrons were emitted with a cosine distribution from the surface, 50% would be collected, and, if as it is suspected, the distribution is even more strongly peaked than this, an even greater fraction would be collected.

The collector and grid were made in disk form purely for ease of construction. This makes it, of course, impossible to measure accurate energy distributions of secondary electrons because the electron trajectories will be bent away from the grid when it is more negative than the target. The grid and collector shield protect the collector from all currents but those which are transmitted through the grid.

F. Target System

The target and its supporting pieces are shown in Figures 13 and 15. The target is pinned to thick tungsten supports by tungsten pins and warp-preventing clamps so that only tungsten pieces are in contact with it. This is important when the target is to be heated for

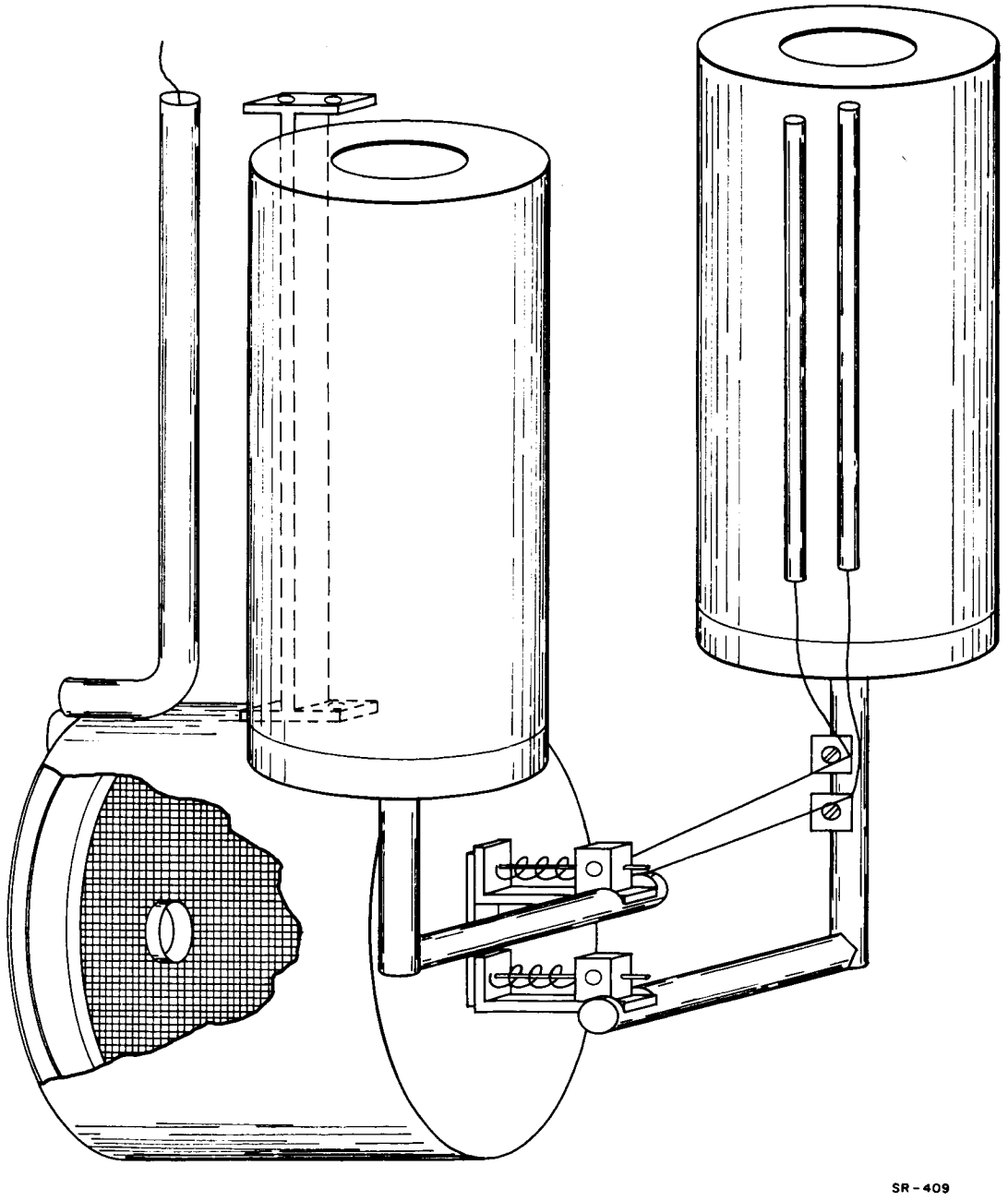

Figure 15. Pictorial of the target and electron collecting system.

a long time at high temperature, for the metallic surface atoms can become quite mobile and diffusion can occur.

This assembly is in thermal contact with the cooling reservoirs through 1/4" diameter copper rods which attach to the reservoir bases. Copper rods of the same thickness, screwed into the bottom of the atmosphere side of the cooling reservoirs, allow a large electrical current to be passed through the target. The reservoirs can be filled with liquid nitrogen without excessive thermal stresses, since the brazed ceramic to Kovar junction is relatively far away from the cold portion of the reservoir.

The tungsten 26% rhenium vs. tungsten 5% rhenium thermocouple is attached to a .030" hole at the side of the target near the center. Each wire is spot welded to a nickel "binding post" as near as possible to a similar tungsten rhenium wire (Figure 15). These secondary wires are then passed out of the vacuum system via the thermocouple feedthrough to the exterior reference junction.

Currents as high as 60 A are required to heat the target to above 2000°K. The magnetic field associated with this current would bend the electron trajectories away from the collector so that the measured secondary current would drop by about one half. To avoid this problem, the target is heated with half cycle alternating current. During each 1/120 sec period that the target heating current is flowing, the ion beam is shut off at FD, and the thermocouple electrometer input

is shorted. Conversely, during each 1/120 sec period that the target heating current is not flowing, the beam is turned on and electrometers measure the thermocouple voltage and the Auger electron current to the collector.

Figure 16 is a diagram of the target temperature control system. The temperature sensing signal provided by the thermocouple is chopped as above so that it may be measured and recorded. The chopped signal is compared with the voltage developed across control potentiometer P1, and the difference signal must again be chopped. An audio transformer provides isolation so that the target may be biased to any value. The signal is amplified by the high gain amplifier, phase detected, and used to trigger the silicon controlled rectifiers in a "Labac" power controller. Finally, an autotransformer and a low voltage transformer adjust the target voltage to the appropriate range. Power diodes in the target circuit convert the full wave ac to half wave ac.

The potentiometer P1 may either be motor driven to provide a linear heating cycle of the target, or it may be manually adjusted. During manual operation of P1, this circuit allows the target to be heated quickly from room temperature to any preset value and then to be held to within 10°K for as long as required. For instance, the target may be heated from room temperature to a steady 1500°K in 1.5 sec.

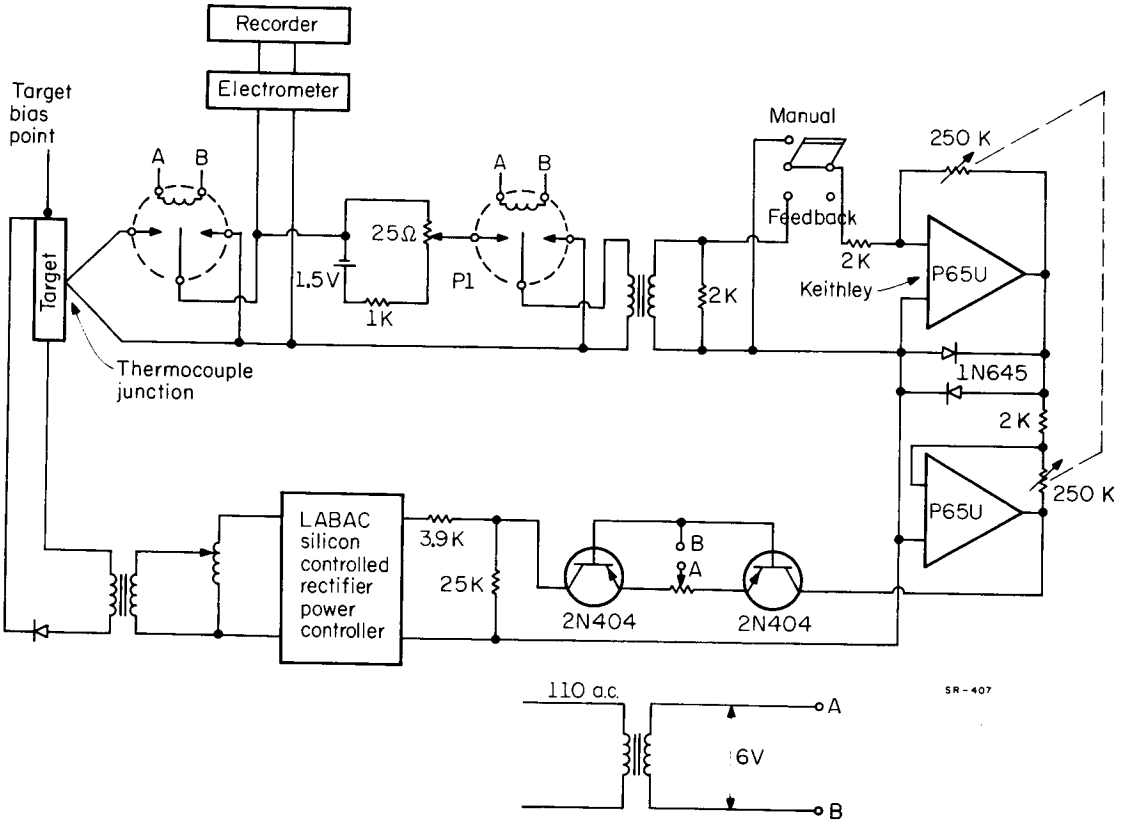

Figure 16. Temperature control circuit.

V. EXPERIMENTAL PROCEDURE

A. Temperature Calibration

Two independent temperature indicators were used in this work for the purpose of calibrating the thermocouple. Because the thermocouple leads are so effective in conducting heat away from the junction, the junction itself is cooler than the target surface. The solution to the equation of thermal conductivity shows that the temperature of the thermocouple junction T_{tc} is approximately linearly proportional to the true surface temperature T.

Temporary installation of a glass window allowed pyrometer observation of the target surface. It was possible to verify that the thermocouple junction was cooler than the heated target surface and to confirm that the temperature gradient across the target was less than 5°K in 1.2 cm at high temperatures. "Pyrometer temperature", T_p, was obtained by making the standard corrections to the actual pyrometer reading to compensate for the fact that the target is not in equilibrium with its radiation. However, since the target is nearly surrounded by partially reflecting surfaces, this correction could be too high. For the range of temperatures high enough to be studied by the Micro-Optical Pyrometer, it was found that $T_p = 1.13T_{tc}$. This proportionality, coupled with the reasoning above, implies that the pyrometer temperature scale should be proportional to the true temperature scale.

The electron thermal emission current j may be expressed in terms of the work function φ as

$$j = AT_e^2 \exp\left(\frac{-e\varphi}{kT_e}\right) , \tag{22}$$

where T_e is the "emission temperature", k the Boltzmann constant, and A a constant. If now,

$$T_p = T_e/d , \tag{23}$$

then

$$j = Ad^2T_p^2 \exp\left(\frac{-e\varphi}{kT_pd}\right) , \tag{24}$$

and

$$\frac{d(\ln j/T_p^2)}{d\left(\frac{1}{kT_p}\right)} = -\varphi/d . \tag{25}$$

Since many investigators[15,40,41] have obtained for polycrystalline tungsten $e\varphi = 4.50\text{-}4.54$eV, it was felt that this value could be assumed. Equation 25 then yielded d so that $T_e = .954\ T_p$. Since this was in accord with our belief that T_p values were slightly too high, we used this emission temperature scale in our work. The proportionalities we have derived give for the final temperature calibration:

$$T = T_e = 1.08\ T_{tc} . \tag{26}$$

B. Target Preparation

The polycrystalline foil target was prepared from .013 cm sheet tungsten. A typical analysis supplied by the manufacturer (Kulite Tungsten Co.) indicates a tungsten purity of 99.95% minimum with

carbon present at 30 parts per million and hydrogen at 6ppm. After mounting holes were cut by electro-erosion, the polycrystal was electro-polished to half its initial thickness.

Single crystal ribbons were cut by electro-erosion from cylindrical single crystal tungsten ingots obtained from the Linde Company. The manufacturer specifies the tungsten purity at $99.99^{+}\%$, with carbon at 5 ppm, and no measurable hydrogen. These ingots were oriented by using back reflection Laue patterns. After cutting, the ribbons were electro-polished to remove damaged crystal structure and foreign atoms sputtered into the volume. We have already described this process in detail.[42]

The (110) target was electro-polished from .038 cm down to .010 cm. Since only one side was polished, one side of the target consists of highly damaged area.

The (111) target was electro-polished from a .043 cm slab down to .012 cm so that the experimental face is .021 cm from each damaged surface. This insures that crystal structure on the bombarded face is practically undisturbed.

All targets were 1" by 1/4", but the clamp edges overlap the target edges so that the heated portion of the target is 1/2" x 1/4".

Each target is cleaned by heating for an hour or more in vacuo to over 2200°K. After this heating period, the target may be repeatedly flashed to high temperature with the accompanying pressure bursts being much less than 1×10^{-9} Torr.

The targets were then heated for several hours to over 2200°K

in 1×10^{-6} Torr of O_2 to remove surface contaminations[43] due to the outward diffusion of interstitial C and to contamination by the pumping fluid. Finally, the oxygen is removed by heating to 2200°K. In all cases we found reasonably reproducible results after this heat treatment.

As an added check on surface cleanliness at the end of each series of experiments, each target was heated to a temperature above that used in the initial cleaning. Repetition of some experiments showed no change in the results for the polycrystal, and changes small enough to be attributed to thermal etching for the single crystals.

C. Biasing

At elevated temperatures a metal surface will emit both electrons from its conduction band and positive ions from impurities or adsorbed gases. Both currents may be retarded out by biasing the target positively, the grid at the (ground) potential of the chamber walls, and the collector more positively than the target.

Referring to Figure 9, it is clear that the fractional change in Auger yield with monolayer coverage is greater at the high energy end of the distribution. The experiment was begun with the target biased at +4.5V, but it was found desirable to increase this value to 7.5V in order to increase the sensitivity enough to study H_2 and N_2. All of the data presented here were taken with 96 eV He^+ ions striking the target and secondary electrons with energy below 7.5 eV retarded out. The measured yields then refer only to those electrons in the Auger energy

distribution whose energies are greater than 7.5 eV. We shall continue to use the symbol γ for this quantity. The electron collector emf was +8.4 V with respect to the grounded grid.

D. Operation During Experiments

Immediately after a 4 hour bakeout at 400°C, the residual gas pressure drops to below 1×10^{-9} Torr, and, in another day, to 4×10^{-10} Torr. However, in order to have pressure in the 10^{-10} Torr range during the experiment, the ionization chamber must be outgassed at well above operating temperatures for many hours. The target is then outgassed as above. When this outgassing procedure is completed, contamination in experiments lasting several hundred seconds is very slight. The addition of 7.0×10^{-6} Torr of Linde He to the system to create the ion current does not greatly degrade the vacuum. The Linde He used specifies less than 30 ppm impurities, so the impurity pressure should be less than 2×10^{-10} Torr, slightly less than the residual gas pressure of the system itself. The adsorbable gas pressure is usually adjusted to around 2×10^{-8} Torr so that the adsorbed layer should be better than 95% pure (assuming reasonable sticking coefficients).

Flash filament measurements were generally made by the "slow flash" method ($p'/\tau \gg dp'/dt$), so that eq. 14 holds. The temperature control feedback system is used with a variable speed motor driving potentiometer P_1. The target is heated to 2000°K with the thermocouple voltage linearly proportional to the time. A complete sweep

usually takes about 30 sec. According to the theory presented in Chapter III, the pressure and temperature data allow the number of gas molecules bound to the target in each group of adsorption states and the corresponding range of desorption energies to be calculated. V/τ for the system is calculated to be 89.7 liter/sec by observing the exponential decay time of pressure bursts in the vacuum chamber. This measurement could be in error by as much as 50%, although from the agreement of our measurements with those made by other workers, we suspect it is much closer than this. Errors in V/τ would change our measurements of the numbers of gas molecules bound on the surface in different states. However, the relative magnitudes of number of adsorbed molecules should be accurate in any case.

Auger desorption measurements are made in a manner analogous to flash filament measurements. The surface is allowed to adsorb a fixed amount of gas by being held at low temperature for a fixed period. With the ion beam held at constant current, the temperature is manually increased until the collector current begins to rise due to the onset of desorption. Then the target temperature is held constant until the collector current reaches a steady state, implying that the surface coverage has reached equilibrium at that target temperature. In practice this usually takes from 5 to 30 sec and the degree of equilibration varies greatly with the binding states under observation. This process is continued until the surface is completely cleaned by heating to over 2000°K, at which time the target heating current is shut off and the

next adsorption period begun.

Since the experiment is performed for convenience sake at a constant pressure of adsorbable gas, we must verify that the desorption endpoints observed are not the result of equilibria between adsorbing and desorbing gas at a high coverage. If this occurred, sharp changes in the sticking coefficient could be confused with desorption states. Equilibrium results when

$$-\frac{dn}{dt} = \beta n - \frac{ps}{(2\pi mkT)^{1/2}} = 0 , \qquad (27)$$

where $p/(2\pi mkT)^{1/2}$ is the arrival rate in molecules/cm^2 sec, usually around 1 monolayer in 300 sec in our experiments. If there were N molecules in a monolayer, the equilibrium fractional coverage would then be given by,

$$\theta = \frac{n}{N} = \frac{p}{(2\pi mkT)^{1/2}} \frac{s}{\beta N} \sim \frac{s}{300 \cdot .3} \sim \frac{s}{100} . \qquad (28)$$

But, as s must be less than 1, we see that such equilibria are found only at very low coverage. Therefore, n must approach a real equilibrium closely at every desorption state.

There are two effects which decrease the quality of these data. The first is due to the operation of the ion beam control system. As molecules of gas are desorbed into the system, some are ionized in the ion source so that the fraction of the ion beam composed of He^+ decreases. Since the Auger yield for He is much larger than for the adsorbable gases, the collector current dips somewhat until the

pressure burst diminishes. This effect usually amounts to less than 1% of the collector current and lasts only 1 sec. It could be completely obviated by containing the ion gun and He gas in a separate pressure chamber.

Second, at temperatures over 1600°K a spurious negative current appears at the collector. This could be due to photoelectrons from the grid. As this current increases uniformly and disappears as the heating current is shut off, it cannot be mistaken for the desorption of gas molecules.

E. Calculation of Desorption Energies

For most of the experiments, both flash filament and Auger, the measureable kinetic quantity is desorption temperature, T_D. Since calculation of the desorption energy from $\beta(T)$ requires T_D and ν, we must estimate the pre-exponential ν to calculate E from eq. 2,

$$E = kT_D \ln \frac{\nu}{\beta} . \qquad (29)$$

However, as this quantity occurs only in logarithmic form, small errors will not affect the answer greatly. As in Chapter II, we shall assume $\nu = 1.6 \times 10^{13}$ cycles/sec for our calculations. This implies a quantum energy in the vibrational mode of the adsorbed molecule of .065 eV, a result comparable to values observed in electron scattering experiments.[2]

F. Pressure Measurements

The Bayard-Alpert gauge, Westinghouse 5966, was not especially calibrated for this experiment. For any gas at true pressure p, the sensitivity S at gauge emission current i_{em} and gauge ion current i_{ion} is defined as

$$S = \frac{i_{ion}}{i_{em} x\ p} \quad . \tag{30}$$

Assuming the nominal calibration of 10 $Torr^{-1}$ for this gauge for N_2, the relative sensitivities for the other gases used may be obtained from Lewin.[44] Thus, the sensitivities for the other gases used in this work are 11.3 mm^{-1} for CO, 4.34 mm^{-1} for H_2, and 2.09 mm^{-1} for He. Merely as a means of designating O_2 pressure, 10.0 mm^{-1} is taken as the sensitivity for O_2.

Measurements of N_2 pressure are, as far as is known, free of artifacts. However, the measurement of CO and H_2 pressures is more difficult.

Two effects may be encountered in measuring H_2 pressure because of the production of atomic hydrogen by the high temperature filament of the ion gauge.[45] Firstly, atomic hydrogen may react with the walls of the vacuum chamber releasing other gases, primarily CO, into the working volume. This effect would certainly have been noticed here, but it was never observed. Secondly, the pumping speed for atomic hydrogen may be different from that for molecular hydrogen.

This would result only in small errors in measuring the surface coverage of H_2.

Errors in measuring CO pressure are present due to dissociative ionization of CO by electron impact on the ion gauge's grid surface. However, since the gauge was well outgassed before experiments and was operated at 10 mA emission current, this effect should be small.[46]

VI. EXPERIMENTAL RESULTS

A. Introduction

In order for the Auger process to be conveniently applicable to the study of the desorption of gases, it should have two properties:

(1) It must have no strong intrinsic temperature dependence.

(2) Change in yield, $\Delta\gamma$, must be a known single valued function of n, the density of adsorbed molecules.

Our experiments indicate that there is no temperature variation of the Auger yield. For the portion of Auger electrons collected with energies above 4.5 eV or 7.5 eV, no change in yield from 100°K to 1700°K could be detected, though we could have measured a change as small as 1%. Above this temperature, the effect attributed to the collection of photo-electrons made measurements less precise. However, there again appeared to be no yield dependence on temperature up to 2300°K, although the possible error is large in this range. This property of the Auger yield means that surface coverages at different temperatures may be compared without any temperature correction.

B. Auger Cross Section

With respect to the second condition, we mentioned in Chapter IV that previous experimental results would indicate that the yield decrease per adsorbed molecule should be approximately constant. We define the "Auger cross section", $\sigma(n)$, as

$$\sigma(n) = \frac{10^{14}\text{molecules/cm}^2}{\gamma_{CL}} \quad \frac{d[\Delta\gamma(n)]}{dn} \qquad (31)$$

for a surface whose clean Auger yield γ_{CL} is decreased by $\Delta\gamma$ because of the adsorption of n molecules/cm^2. The quantity $\sigma(n)$ will describe this relative yield change per adsorbed molecule. Note that $\sigma(n)$ is a dimensionless quantity. How will $\sigma(n)$ vary with n?

Figure 17 shows the normalized change in yield $\frac{\Delta\gamma}{\gamma_{CL}}$ due to the adsorption of β state CO on a polycrystalline tungsten target as a function of the exposure of the target to CO. The normalized surface coverage $\frac{n}{n_{6L}}$ of β CO on the target determined by flash filament technique from eq. 15 is also plotted vs. exposure. It can be seen that the shapes of these two curves are similar. Figure 18 shows the normalized yield change plotted against the normalized coverage. Because of the difficulty of measuring these two quantities under comparable experimental conditions, the exact shape of this curve is really difficult to determine. However, the derivative of this experimental curve, also shown in Figure 18, should give a reasonable indication of the behavior of the Auger cross section, $\sigma(n)$. The significance of this curve is that $\sigma(n)$ tends to decrease as the surface coverage increases, and we again emphasize that this curve has not been determined with sufficient accuracy to merit detailed conclusions.

Figure 19 shows both normalized yield change and normalized surface coverage as a function of exposure of a polycrystalline tungsten target to H_2. Figure 20 shows the normalized yield change and the derivative of the normalized yield change plotted against coverage.

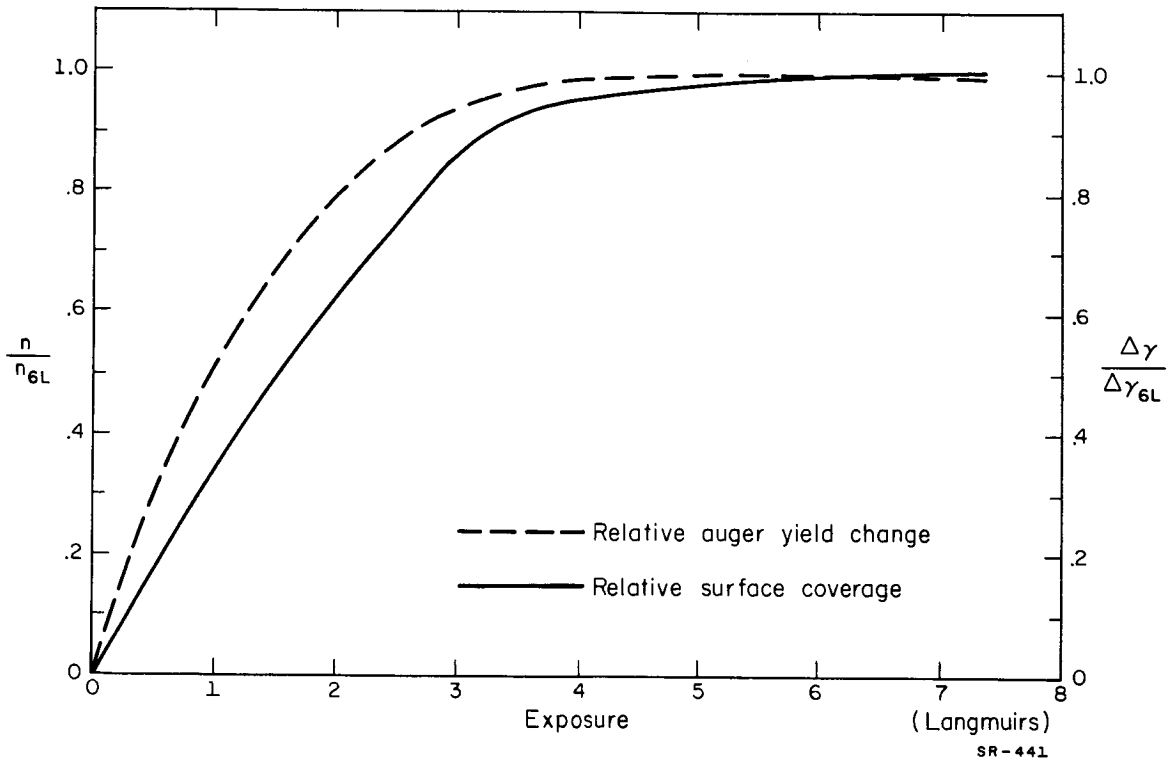

Figure 17. Comparison of the relative change in Auger yield (dashed curve) with the relative number of CO molecules adsorbed on polycrystalline W (solid curve) as a function of exposure. The solid curve is from flash filament measurements.

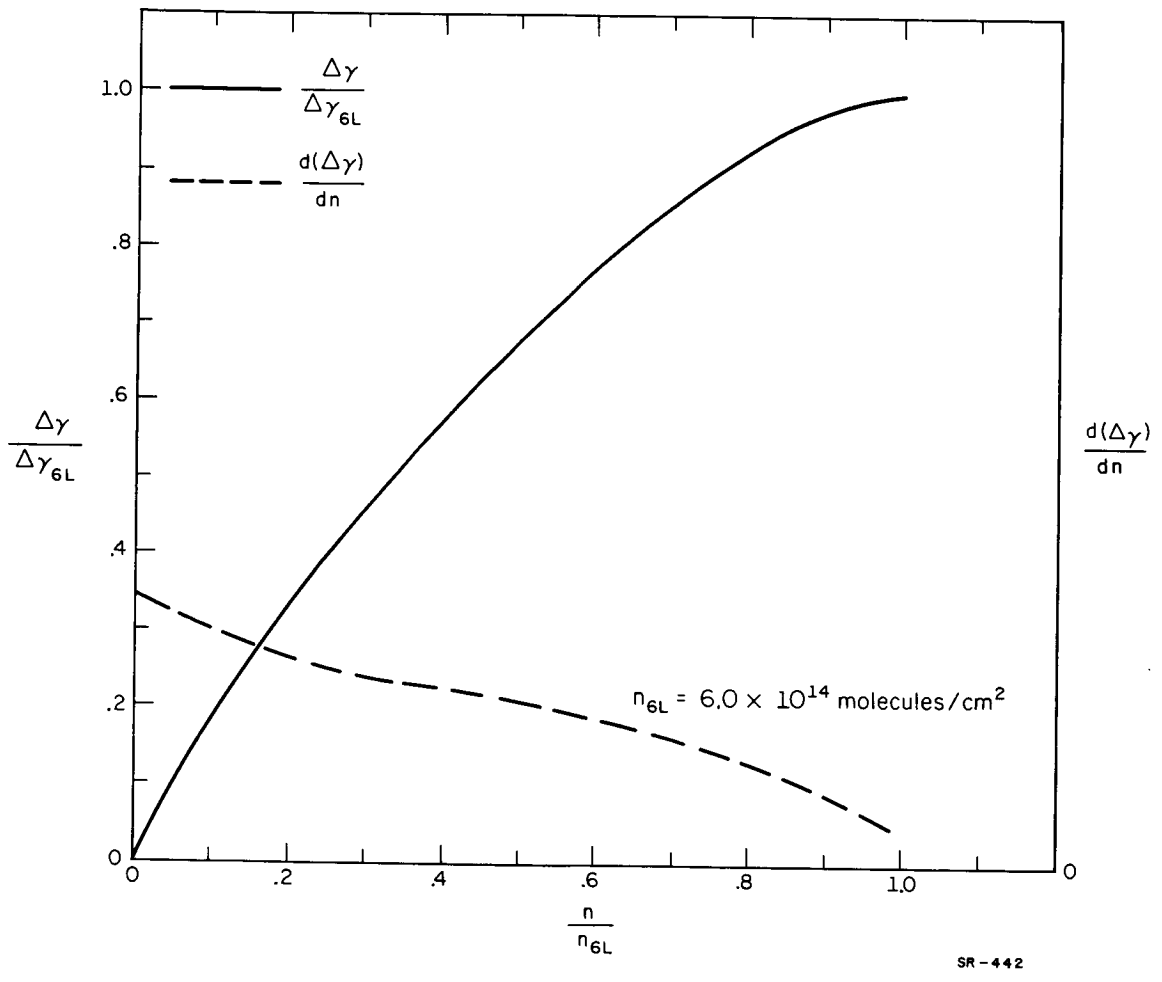

Figure 18. Relative yield change from Figure 17 (solid curve) versus relative surface coverage. The dashed curve is the derivative of the solid curve and is proportional to the Auger cross section of CO.

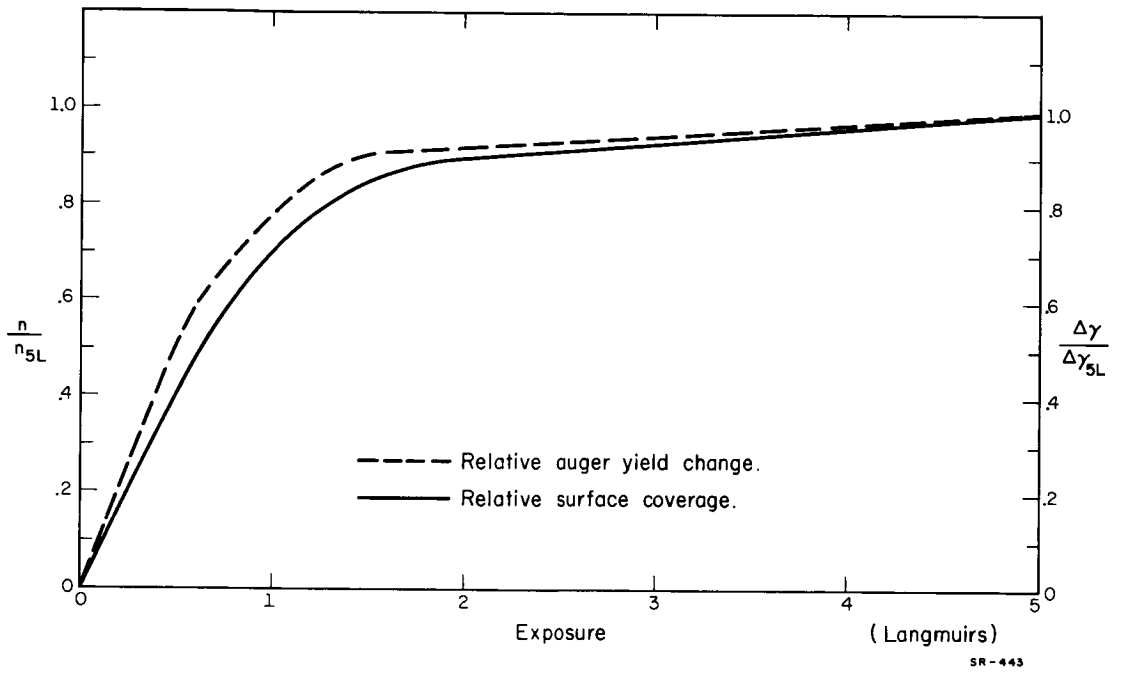

Figure 19. Comparison of relative change in Auger yield (dashed curve) with relative number of H_2 molecules adsorbed on polycrystalline W (solid curve) as a function of exposure. The solid curve is obtained from flash filament measurements.

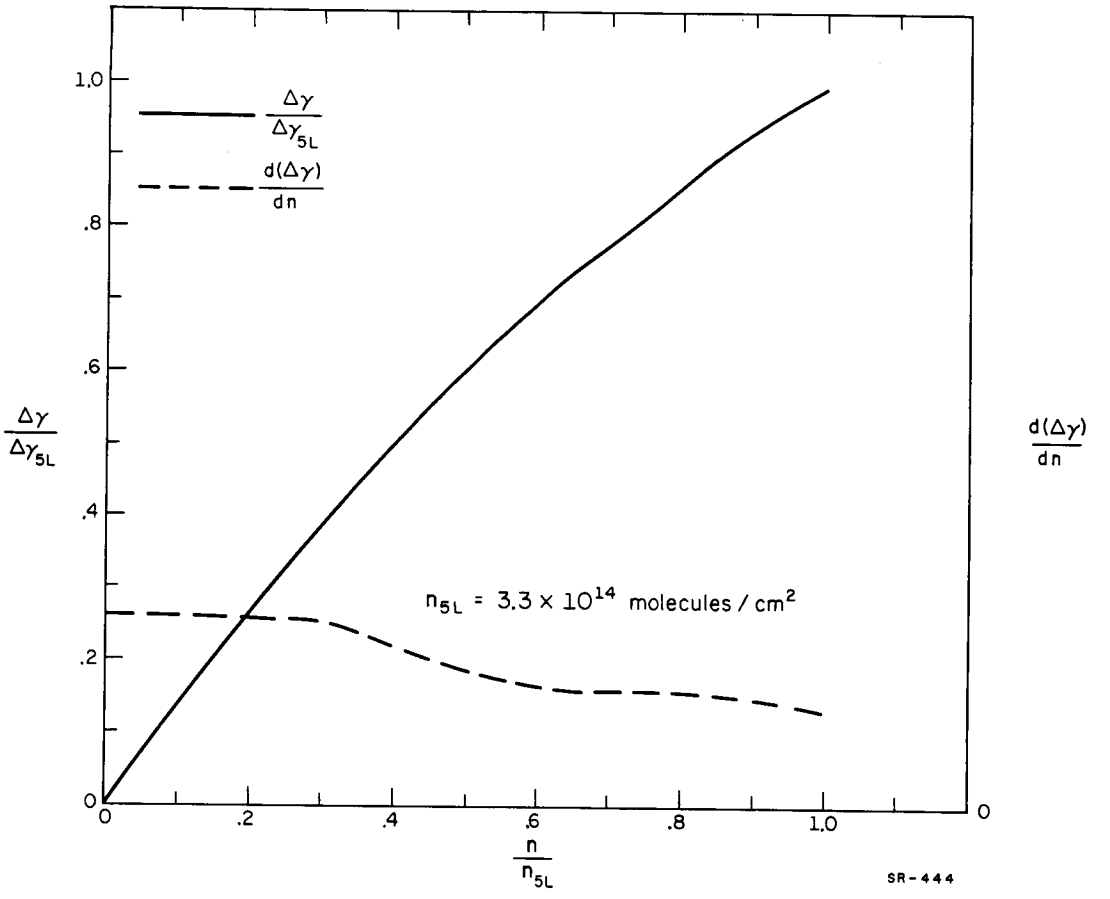

Figure 20. Relative yield change from Figure 19 (solid curve) versus relative surface coverage of H_2. Dashed curve is the derivative of the solid curve and is proportional to the Auger cross section of H_2.

Since this data has accuracy similar to the CO data, we merely note the decrease of the cross section with coverage.

One simple explanation of this proceeds from the results of the following chapter, where we will show that there is a great multiplicity of binding states involved in the adsorption of CO and H_2 on polycrystalline W. We will also show that these molecules tend to desorb from the highest energy states available to them. Thus, if the Auger cross sections of molecules bound in the high energy states were higher than the Auger cross section of particles bound in the low energy states, a continuous decrease in Auger cross section would be measured as the surface adsorbs gas. In this case, the mathematical treatment of Chapter I will be as valid for $\Delta\gamma$ as for n. We need only modify it by using in place of initial state densities, initial state densities multiplied by Auger cross sections. For instance, the form of eq. 5 will be modified to

$$\Delta\gamma = \sum_{j=1}^{10} n_j(0)\times 10^{-14}\, \sigma_j\, \gamma_{CL}\, e^{-(e^{-Ej/kT})t\upsilon} \quad , \quad (32)$$

where σ_j is the Auger cross section of molecules in the state $n_j(0)$.

In most cases studied here, only a small fraction of the gases held on the surface are desorbed during one temperature increment. If, in a small region of coverage n, $\sigma(n)$ can be approximated as a power of n, say

$$\sigma = Dn^m \quad , \quad (33)$$

the equation of first order desorption (eq. 1 with x=1) will become, in terms of $\Delta\gamma$,

$$\frac{-d(\Delta\gamma)}{dt} = (m+1)(\Delta\gamma)\,\beta(T)\,. \qquad (34)$$

Thus the form of the equation is really unaltered. Therefore, in this region the solutions to the first order Auger desorption equation are the same in form as in a region of constant cross section.

Both of these arguments indicate that the change in cross section with coverage will not seriously affect the use of Auger measurements in determining the kinetics of desorption of gases by a first order process. The case of second order desorption does not reduce in as simple a manner. However, no effects solely attributable to second order desorption were observed in this work.

The Auger cross sections of molecules bound in different types of states, however, can be vastly different. To compare these, in the next sections we will tabulate the average value of cross section for a given state i determined for complete coverage of N_i molecules/cm^2. In that state, the average cross section σ_i will then be given by

$$\sigma_i = \frac{10^{14}\ \frac{\text{molecules}}{\text{cm}^2}}{\gamma_{CL}}\ \frac{\Delta\gamma_i}{N_i} \qquad (35)$$

C. Gaseous Desorption

1. CO on Polycrystalline Tungsten

Flash filament studies of the adsorption of CO on polycrystalline W at $\simeq$ 350°K are shown in Figure 21. These curves suggest that there are three major groups of adsorbed states, one held with small binding energy, and two more strongly bound overlapping

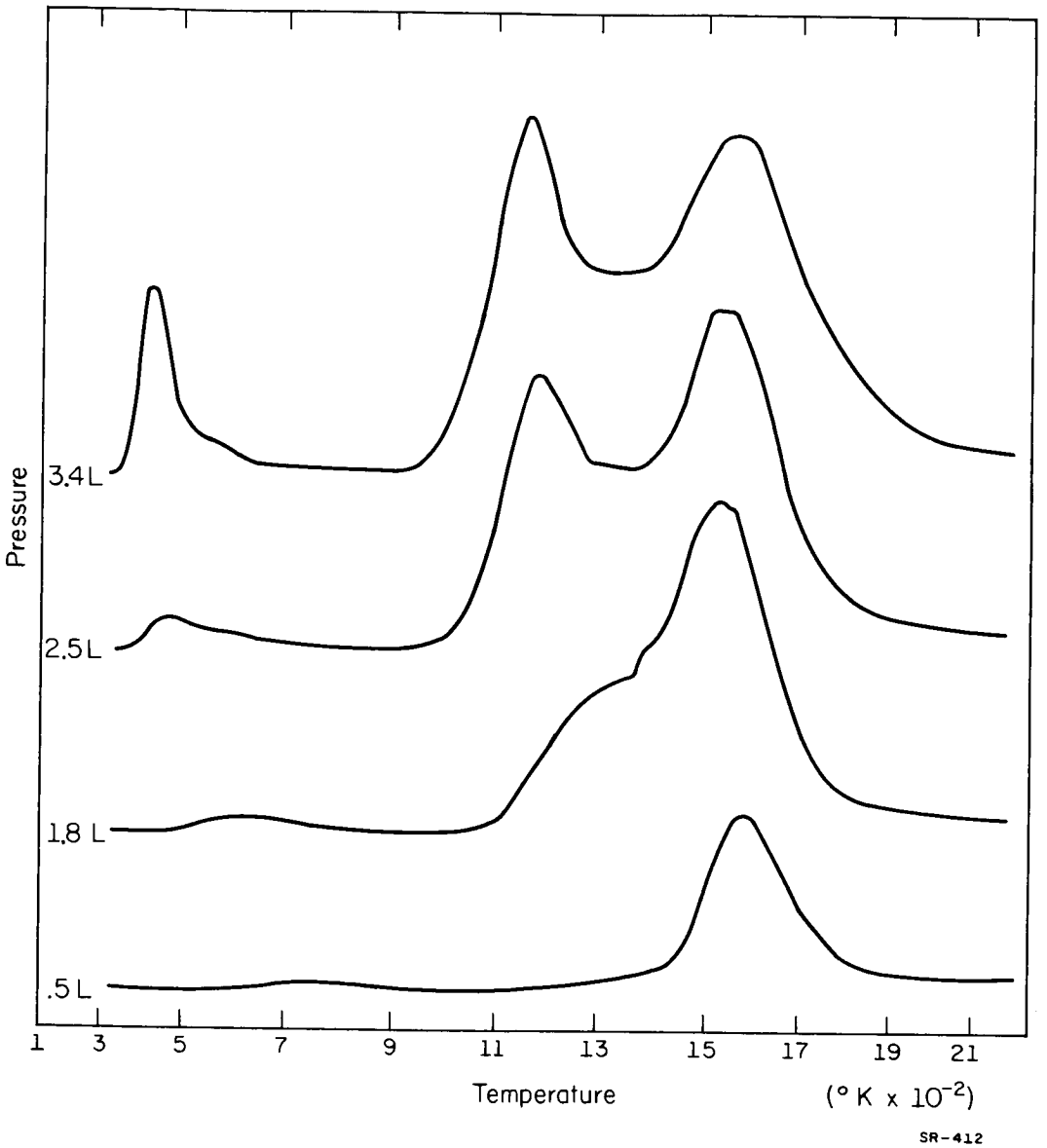

Figure 21. Flash filament desorption spectra of CO adsorbed on polycrystalline W at 350°K

groups. If, as is believed, CO desorbs with first order kinetics and the vibrational mode normal to the surface has 0.065 eV energy[2] ($\nu = 1.6 \times 10^{13}$ sec^{-1}), the binding energies of these states obtained from eq. 17 are:

$$E_{\alpha} = 1.31 \text{ eV},$$

$$E_{\beta_1} = 3.00 \text{ eV},$$

and

$$E_{\beta_2} = 3.92 \text{ eV}.$$

We have followed the custom of referring to the lowest energy state when a gas is bound in a series of states as α.

Referring to Figure 18 again, the equilibrium surface β coverage of the polycrystalline W target at 350°K is 6.0×10^{14} molecules/cm^2. The sticking coefficient at low coverage is 0.46.

Figure 22 is a recording of an Auger desorption experiment performed in the manner described in the last chapter. The temperature (dashed line) is raised until the Auger yield (solid line) begins to change because of desorption. The temperature is then held constant until the yield again reaches equilibrium, at which a new value of Auger yield corresponding to a less covered surface results. Figure 23 shows a similar experiment carried out at higher initial coverage. If there were only a small number of desorption states such as the three proposed by Ehrlich, this would be immediately apparent in the reproducibility of the equilibrium values of the Auger yield. However, equilibria may be found almost at will by making the temperature increments very small. This result strongly indicates a continum of desorption energies.

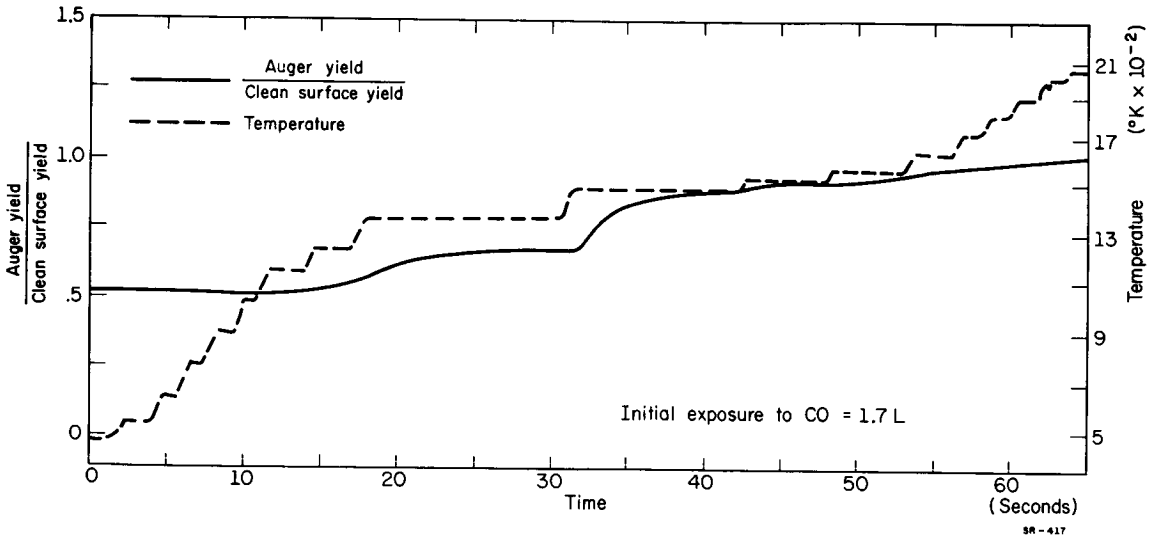

Figure 22. Auger desorption experiment at low initial coverage for CO adsorbed on polycrystalline W at 350°K. The temperature scale (dashed curve) is at the right. The Auger yield scale (solid curve) is at the left.

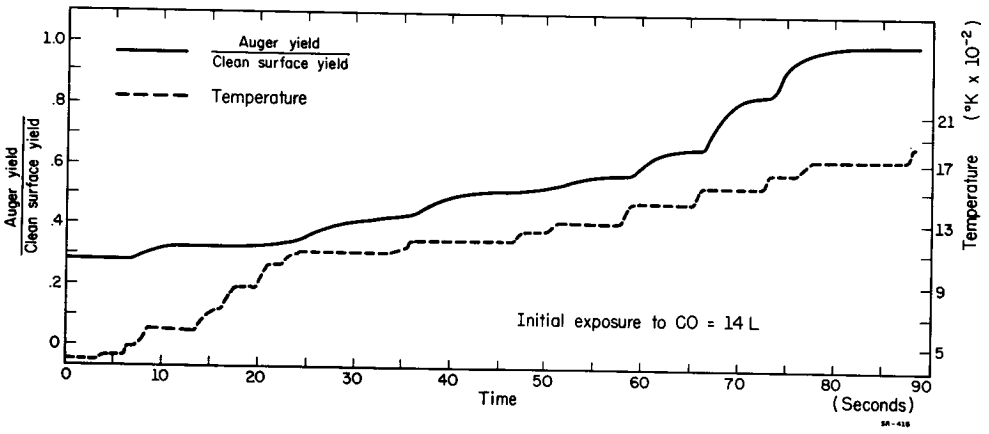

Figure 23. Auger desorption experiment at high initial coverage for CO adsorbed on polycrystalline W at 350°K.

In Figure 24 the relative yield changes at constant temperature $\frac{\Delta \gamma_o}{\Delta \gamma}$ are plotted on a log scale against time for two different sets of desorbed states. $\Delta \gamma_o$ is the maximum Auger yield change during the isothermal desorption under question. If these yield changes corresponded to the emptying of pure first order states, the plots would be straight lines having slopes equal to the desorption constants, β (T). Since these curves have steeper slopes at low values of time, they correspond to a distribution of desorption states. This indication of a distribution of states is consistent with the fact that the yield changes do not show unique endpoints.

One of the experimental desorption rate curves of Figure 24 is compared with a calculated curve (dashed line). The calculation was made using an approximate state distribution derived from Auger experiments such as Figure 23. For this calculation, molecules bound with energies of less than 4.2 eV are assumed to have been previously desorbed. The desorption rate curve for the molecules left on the surface is then calculated as in Chapter I for 1620°K (the temperature of desorption for the experimental curve). It is seen that the agreement is good, considering the probable error at large times in the experimental curve.

Other experiments[21] have confirmed that there is no C contamination of a W target after CO desorption, indicating desorption should be first rather than second order. All of these observations are consistent with the picture of a quasi-continuous range of first order

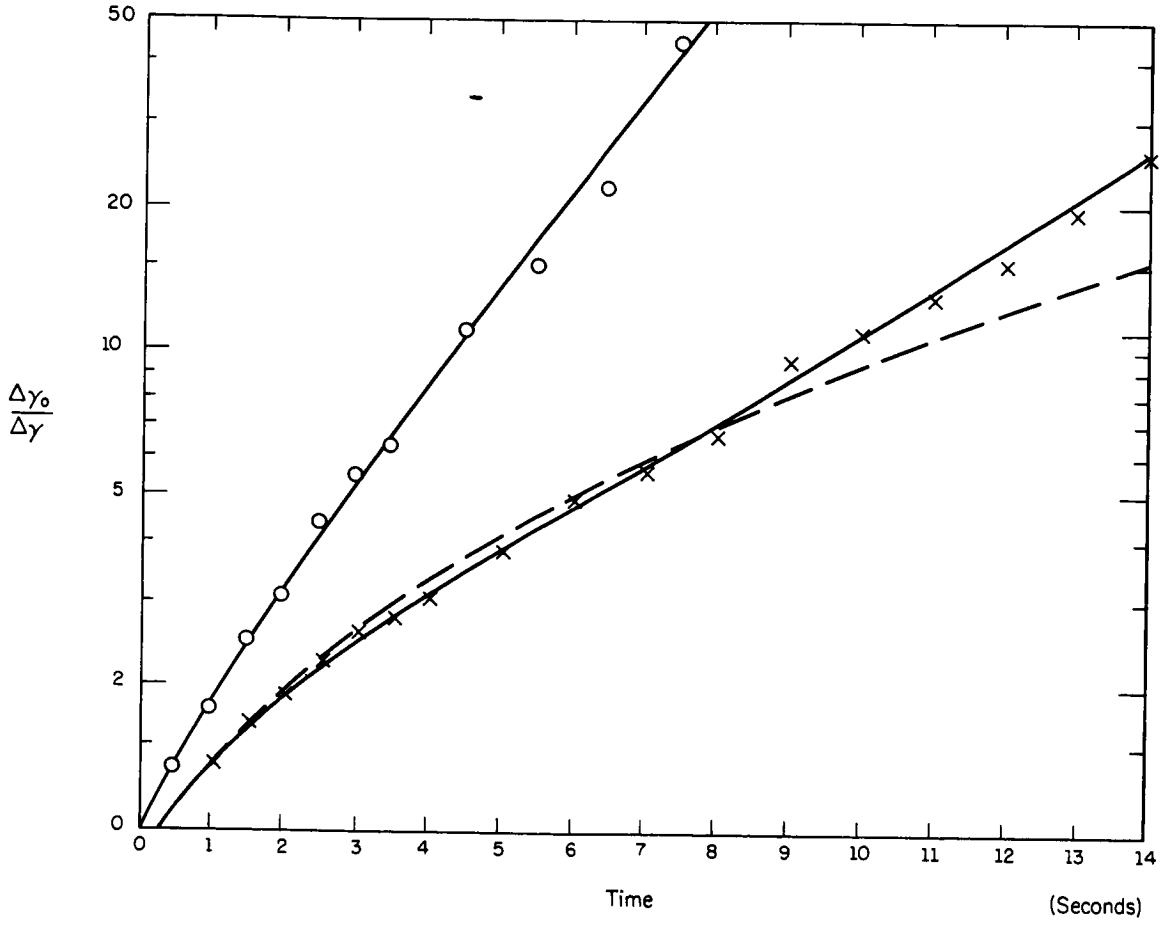

Figure 24. CO desorption rate curves for some groups of states desorbing from polycrystalline W showing multiple state behavior. The dashed curve is a theoretical curve.

adsorption states, with adsorption into the highest energy states first so that the energy of the total system is always a minimum.

Because of this range of energies, analysis of the structure of the desorption constant β (T) is not simple. In particular, plotting ln β vs $\frac{1}{T}$ will not produce a straight line, because at any given temperature molecules will desorb from various states with correspondingly different rates. Hence, we have continued to assume that the ν in eq. 29 is 1.6×10^{13} in order to calculate desorption energies from β and T.

Figures 25, 26, and 27 compare the results obtained with flash filament and Auger desorption experiments. In Figure 25, the Auger current is measured while the target is heated with the temperature schedule used in flash filament desorption. Figure 25 was made under relatively low current conditions, so that the frequency response was poorer than usual, but the temperature scale has been compensated for this poor response. Under the approximation of constant Auger cross section, the relative number of molecules left on the surface is indicated during the temperature sweep by the decreasing value of $\Delta\gamma$. For the magnitudes of pumping speed and temperature sweep rate we are using, the flash filament equation is just eq. 14.

Thus, assuming σ(n) is constant, the Auger sweep curve can be differentiated in order to obtain the equivalent of a flash desorption spectrum for our system. The bottom part of Figure 25 shows $\frac{d\gamma}{dt}$ and can be compared with a high exposure flash filament curve of Figure 21. It can be seen that the two results are quite similar, but

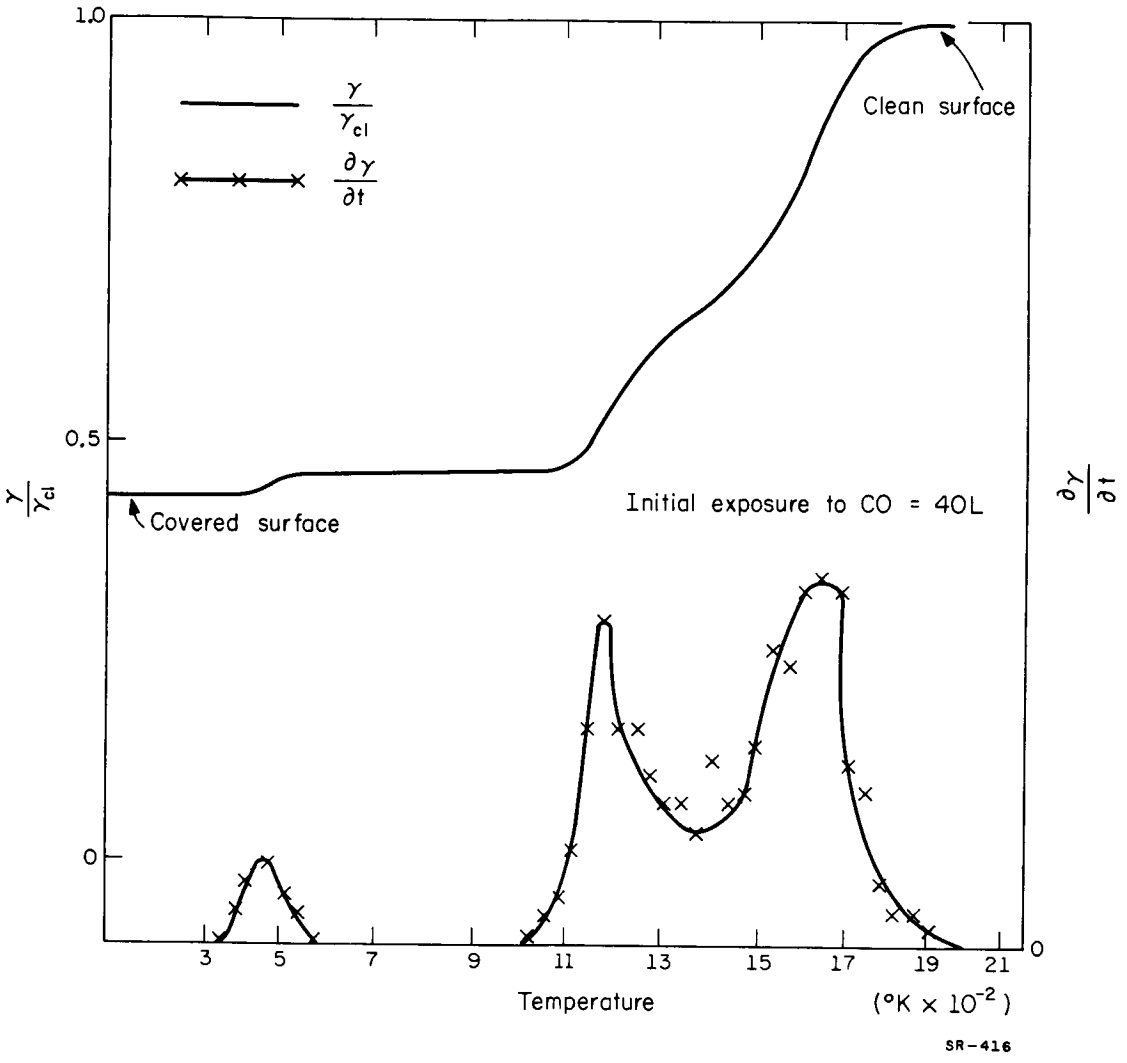

Figure 25. Change in yield associated with desorption of CO from a covered polycrystalline tungsten surface during a linear temperature sweep. The lower curve is the derivative of the upper curve. The CO was adsorbed at 300°K.

since this is not the most profitable way to do the Auger experiment, it was not used extensively.

Figure 26 compares a flash filament spectrum and an Auger desorption experiment performed at nearly the same coverage. The yield changes observed between equilibria in the Auger experiment are plotted at the temperatures at which the equilibria were reached. Figure 27 compares the two types of experiments in the same way for a higher coverage.

It can be seen in Figure 27 that the change in Auger yield associated with the α state is considerably smaller than that associated with the β state. The Auger cross section measured for the β state at room temperature is 0.105. For the α state, the smaller value of 0.01 is measured.

When the polycrystalline target is cooled to $\simeq$ 120°K, the α state is radically extended on the low energy end. The β states remain unchanged. The saturation value of α goes from $\sim 2.3 \times 10^{14}$ molecules/cm^2 to 15×10^{14} molecules/cm^2, assuming the α cross section does not vary. Thus, the coverage for a saturated W polycrystal at 120°K increases to 20×10^{14} molecules/cm^2.

2. CO on (110) Tungsten

The flash filament study of Figure 28 shows that CO adsorbs on (110) tungsten in a low energy α state, and a relatively small but broad higher energy β state. Assuming the usual value for υ and

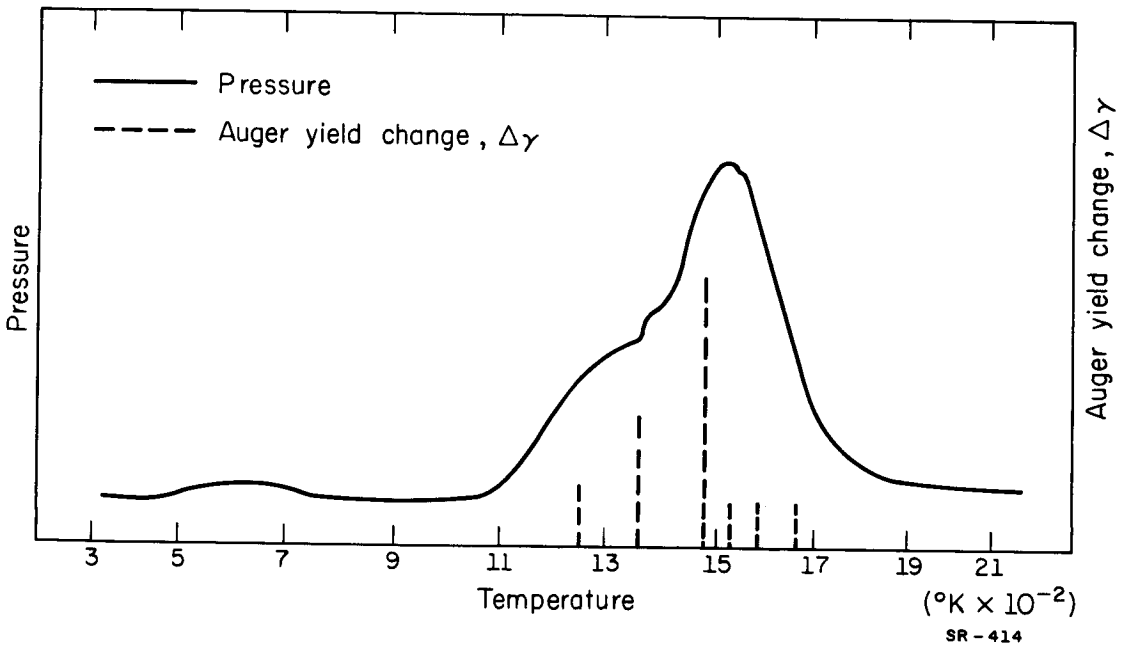

Figure 26. Comparison of flash filament desorption spectrum with Auger yield spectrum at ≃ 1.8 L exposure of polycrystalline W to CO.

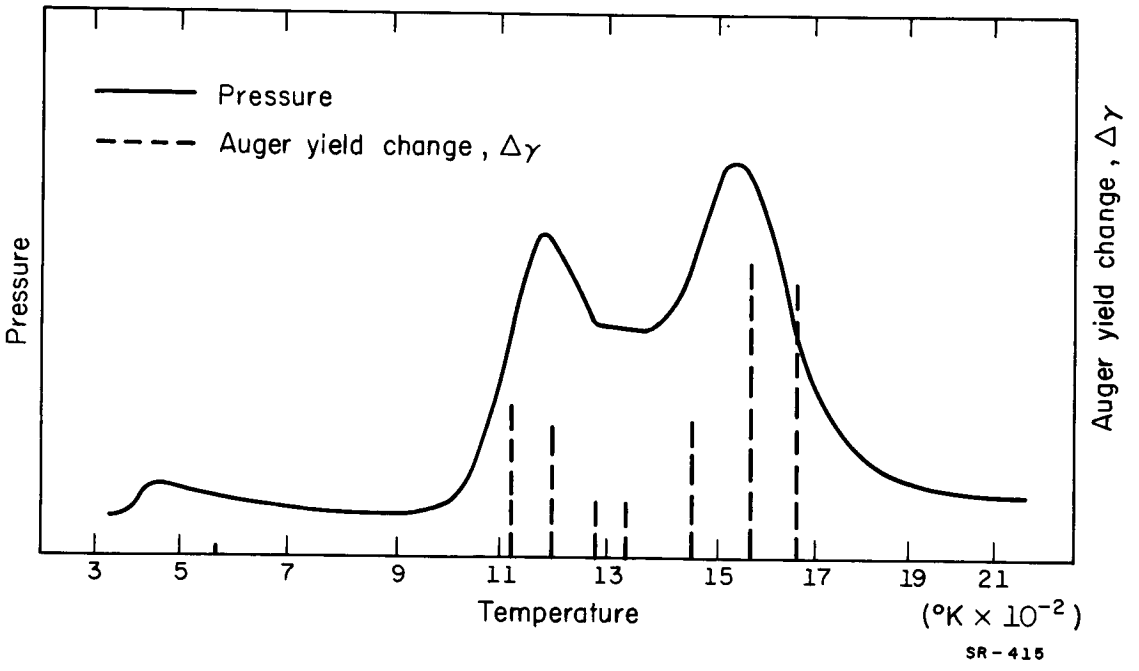

Figure 27. Comparison of flash filament desorption spectrum with Auger yield spectrum at $\simeq 2.4$ L exposure of polycrystalline W to CO.

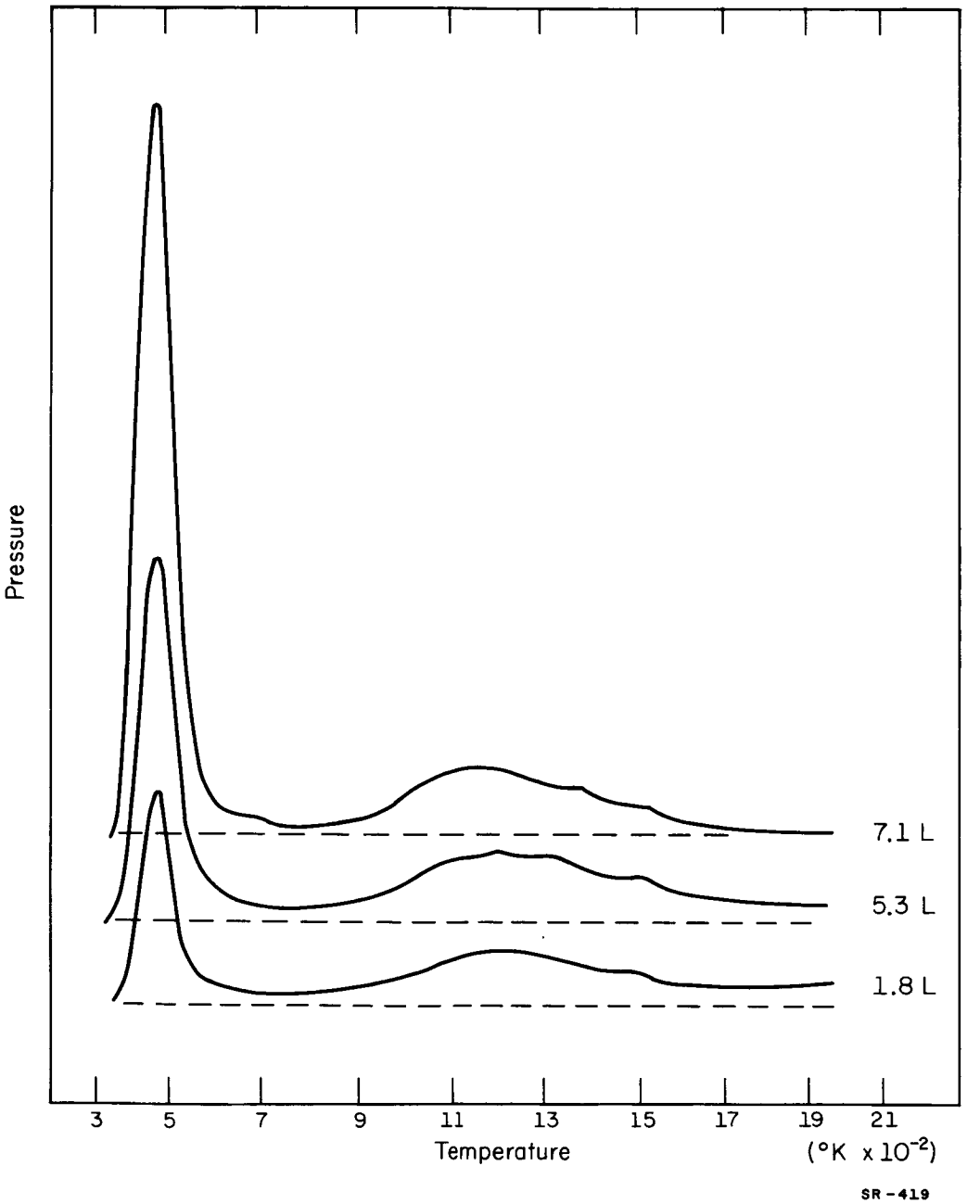

Figure 28. Flash filament desorption spectra of CO adsorbed on (110) W at 350°K.

first order desorption, we find that the α state peak is at 1.30 eV and that the desorption energies for the β state range from 2.7 to 3.9 eV.

The β state adsorbs quite rapidly up to 0.8×10^{14} molecules/cm^2. The α state adsorbs more slowly because its desorption temperature is rather close to the temperature of the target just after flashing. The α state saturation coverage at 350°K, 2.4×10^{14} molecules/cm^2, is shown in the top curve of Figure 28. The sticking coefficient of the α state is $\simeq$ 0.09 at low coverage.

As the target is cooled below room temperature, the amount of gas adsorbed in the α state gradually increases. The picture we have is that there is intrinsically a range of low energy α states available for adsorption, but that, for the target held at room temperature, only a fraction are available for filling. It proved difficult to get accurate flash filament data at 120°K as the pressure peaks are broadened so that exact desorption energies could not be measured (Figure 29). That this effect is caused by the liquid nitrogen cooled reservoir surfaces in the vacuum system is shown by doing a flash filament desorption experiment with the reservoirs cooled while holding the target at 350°K with the Joule heating circuit during the adsorption period. This spectrum shows a much smaller amount of gas desorbed from the α state, but still exhibites the same damped curve shape.

This phenomenon could be accounted for by the formation of a pressure dependent adsorbed layer of gas on the liquid nitrogen reservoir surfaces. The amount of gas adsorbed on these surfaces, then,

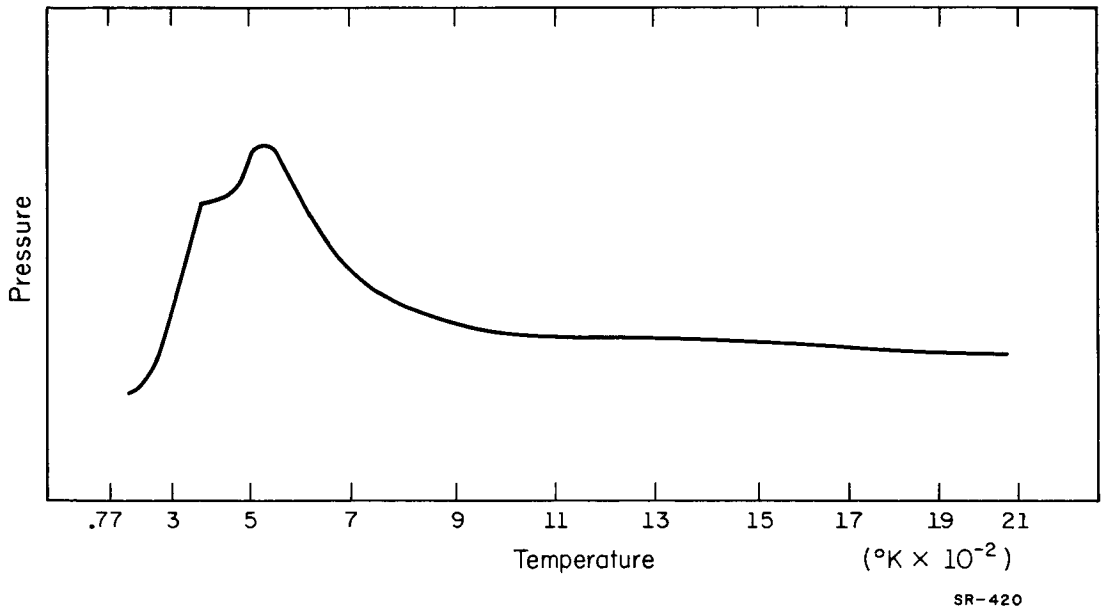

Figure 29. Flash filament desorption spectrum of CO adsorbed on (110) W at 150°K.

would tend to increase as gas was desorbed from the target. Therefore, this CO layer would act to filter all system pressure changes. Another experiment implying that a large adsorbed layer is being formed is the leaking of CO into the clean system with cooled reservoirs. In this case it takes much longer for the pressure to come to equilibrium than it does when the reservoirs are warm.

Such a pressure dependent layer can be easily explained. The number of molecules adsorbing per second in a state of order x with non-zero desorption constant $\beta(T)$ will be given by,

$$\frac{dn}{dt} = \frac{ps}{(2\pi mkT)^{1/2}} - n^x \beta(t). \tag{36}$$

Hence, the equilibrium coverage will be given by,

$$n^x = \frac{ps}{(2\pi mkT)^{1/2}\,\beta(T)} \quad . \tag{37}$$

This quantity has strong pressure dependence for either $x=1$ or 2. If, during the desorption of a set of states, the pressure in the system starts at some equilibrium value and, after the associated pressure burst, concludes at the same equilibrium value, then the amount of gas adsorbed on the reservoir can have neither increased nor diminished. Thus, to the first approximation, the effect of the trap will be to smear out the pressure burst, but not to change $\int p\,dt$. Therefore, the number of particles adsorbed on the W surface may be measured in the same manner as before.

The population in the α state at 120°K is measured to be 17×10^{14}

molecules/cm^2. Since this is very much larger than the β state, β is lost in the tail from the α state, and its population cannot be measured. Assuming the β population remains the same, the total population on the cooled surface will then be 18×10^{14} molecules/cm^2.

Because the β state is present at relatively low coverages and is well spread out, Auger measurements reveal little of interest at room temperature. The α state has a rather low Auger cross section, 0.027, compared to 0.1 for the β state, and we can determine little more than that the set of α states is relatively dense, but definitely not a simple state.

However, as we have seen above, when the target is cooled, the surface concentration of α vastly increases. Auger measurements show a range of states from 0.7 to 1.2 eV, followed by a flat group of states to 1.6 eV (Fig. 30). The logarithmic plots of relative yield changes $(\frac{\Delta\gamma_o}{\Delta\gamma})$ for some of these states are very similar in form to those for the densely packed sets of states in Chapter I. Several of these taken from different portions of the desorption spectrum are plotted in Figure 31.

Because of the poor quality of the flash filament data due to the cooled surfaces, we again performed the Auger experiment with a uniform temperature sweep, to give the analogue of the flash filament desorption spectrum. In these measurements the response of the system is much better than in Figure 25. Figure 32 shows γ and $\frac{d\gamma}{dt}$ for the desorption of the α state of CO from a (110) target cooled

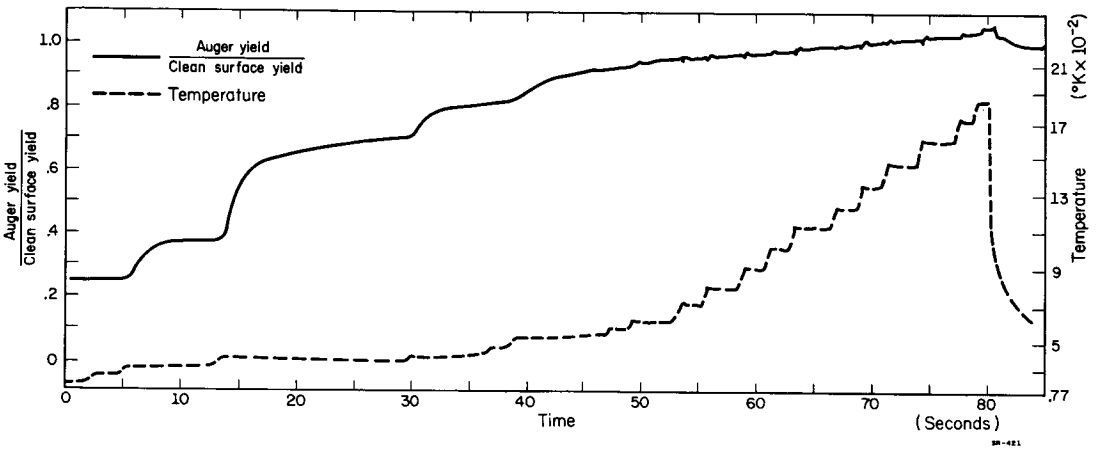

Figure 30. An Auger desorption experiment showing desorption of CO from a cooled (110) tungsten surface (T $\simeq$ 120°K).

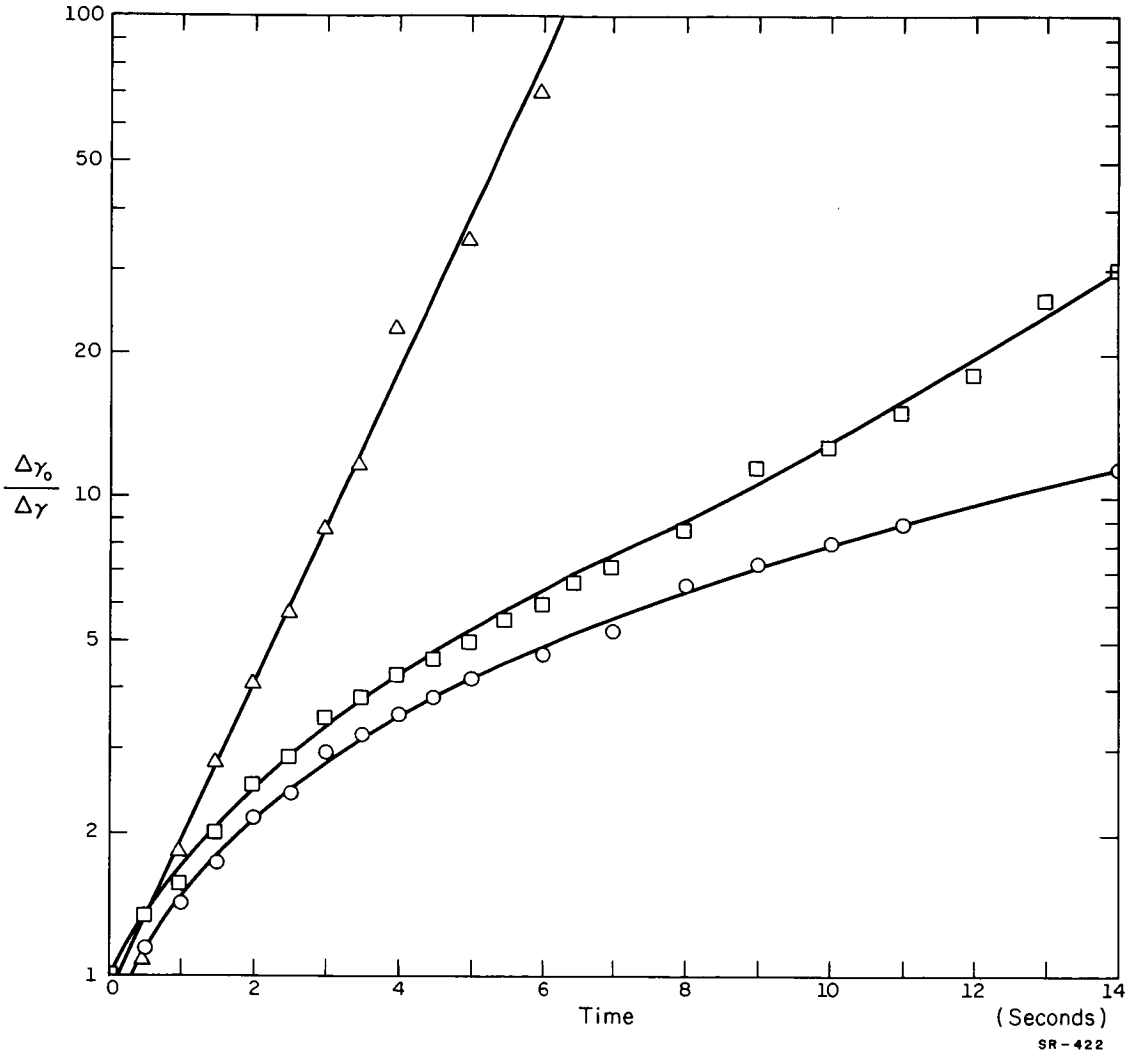

Figure 31. CO desorption rate curves for α state desorption from (110) W.

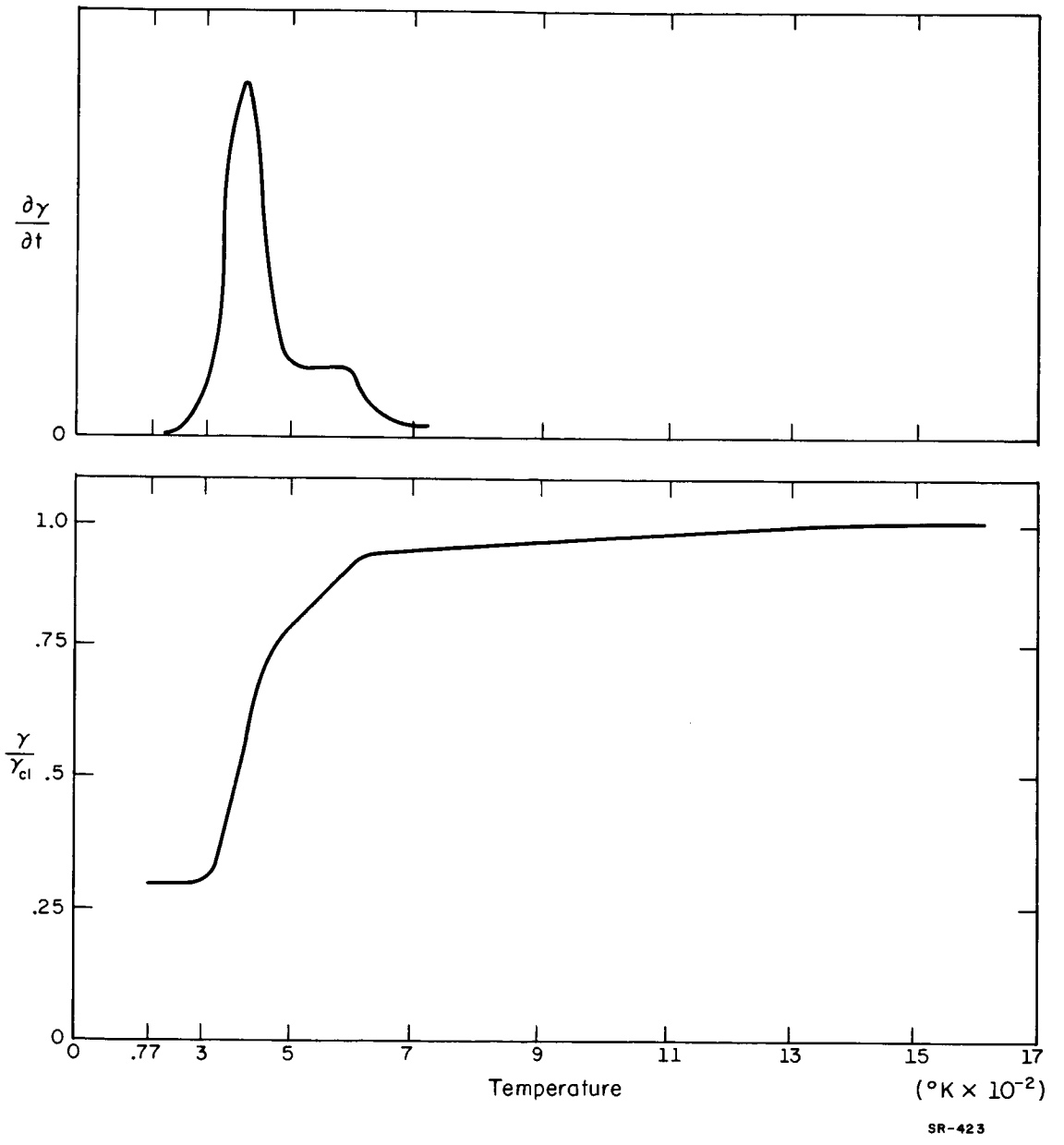

Figure 32. Change in yield associated with desorption of CO from a (110) W surface during a linear temperature sweep. The upper curve is the derivative of the lower curve. The CO was adsorbed at 120°K.

to 120°K. This plot of $d\gamma/dt$ shows clearly the distribution of states indicated above.

3. CO on (111) Tungsten

CO desorbs from (111) tungsten in three different energy regions as shown by the flash filament measurements in Figure 33. A sharply defined set of states at 3.60 eV is followed by a set of distributed states whose maximum lies around 2.8 eV and which extends down to 2.4 eV. There is also a small α state present, again developing after the target is fairly cool, which desorbs at about 1.30 eV. During adsorption, as always, the high energy state fills first. At saturation, about 2/3 of the CO is adsorbed in the highest energy states. The total coverage is 6.4×10^{14} molecules/cm^2 at this coverage, though the α state is relatively small, depending on the exact target temperature.

When the target was cooled to liquid nitrogen temperatures, the quasi-equilibrium situation observed above with the (110) surface again prevented making accurate measurements, as the flash filament peaks are very strongly damped. The areas under the individual peaks of the pressure spectra could not be measured.

On the (111) face of W, the cross section of CO adsorbed in the β state is about 0.09, close to the value of the β cross section for the other faces. Desorption of the distributed β state follows the pattern observed on the polycrystalline face. Many Auger endpoints may be observed, and the individual $\frac{\Delta\gamma_o}{\Delta\gamma}$ curves have the

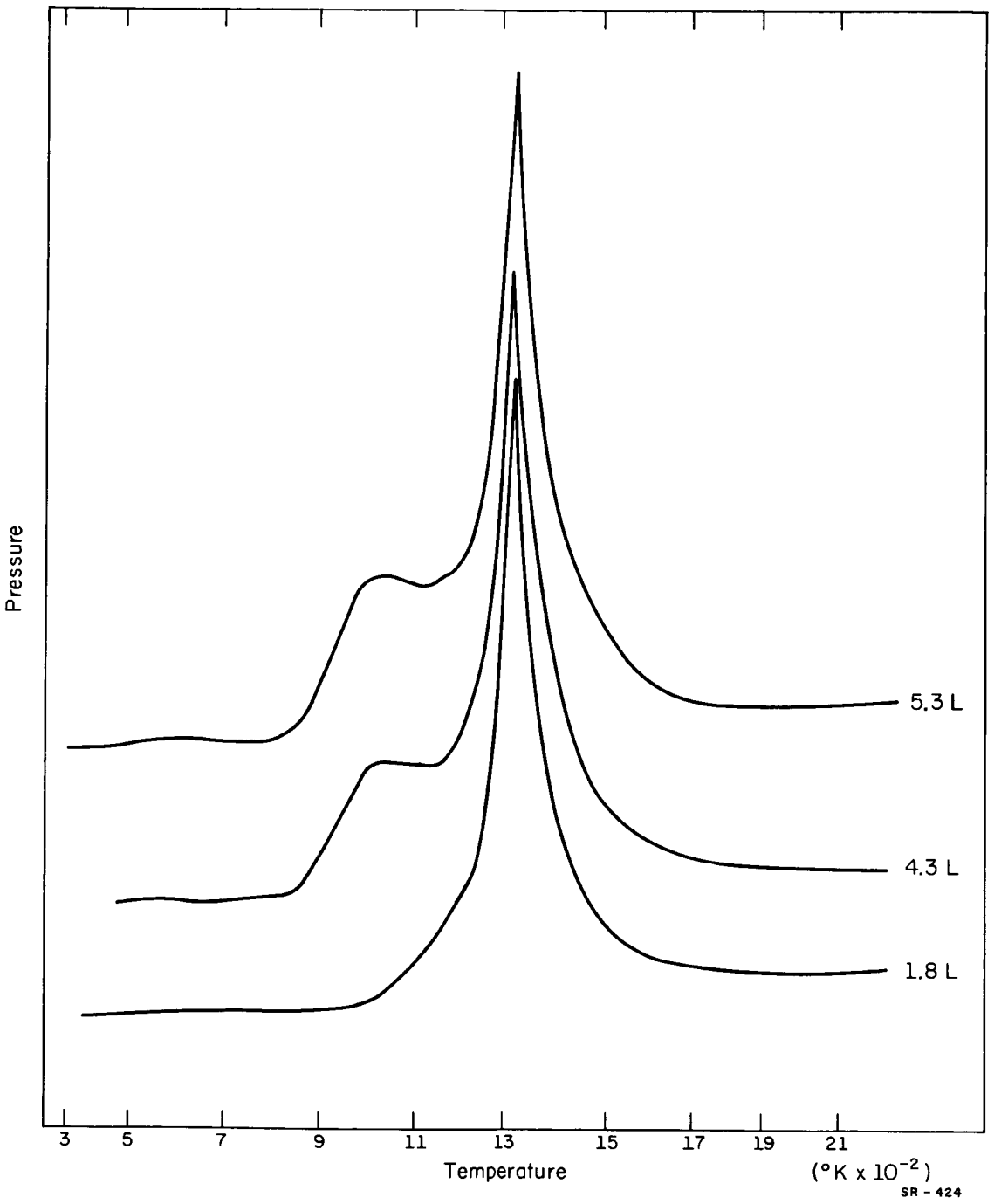

Figure 33. Flash filament desorption spectra for various coverages of CO adsorbed on (111) tungsten at 350°K.

slightly convex upward behavior associated with multiple desorption states.

In contrast to this, desorption at constant temperature of the highest energy state revealed a unique curve shape (Figure 34). Even from the raw data, it was obvious that the collector current approached its asymptote far faster than a first order desorption curve. The anomalous behavior was even more apparent when $\ell n \frac{\Delta\gamma_o}{\Delta\gamma}$ is plotted vs time (Figure 35). It was established in Chapter II that even for a density of states distribution peaked at high energy, the first order desorption plots are never concave downward. The effect of multiple states can never be to distort the initial part of the curve convex downward.

Since this relatively sharp state does not exhibit separate equilibria, it seems to be a simple state. Acting under this assumption, the desorption order is calculated to be somewhat more than +1/2. Figure 36 shows these desorption curves plotted as +1/2 order desorption, i.e.

$$-\frac{dn}{dt} = n^{1/2}\,\beta(T) \tag{38}$$

If now,

$$\Delta\gamma = Dn \tag{39}$$

then

$$\left(\frac{\Delta\gamma}{\Delta\gamma_o}\right)^{1/2} = 1 - t\,\frac{\beta(T)}{2}\,\frac{D^{1/2}}{\Delta\gamma_o{}^{1/2}} \tag{40}$$

Figure 36 plots $\left(\frac{\Delta\gamma}{\Delta\gamma_o}\right)^{1/2}$ vs t, and shows that reasonably straight lines are obtained.

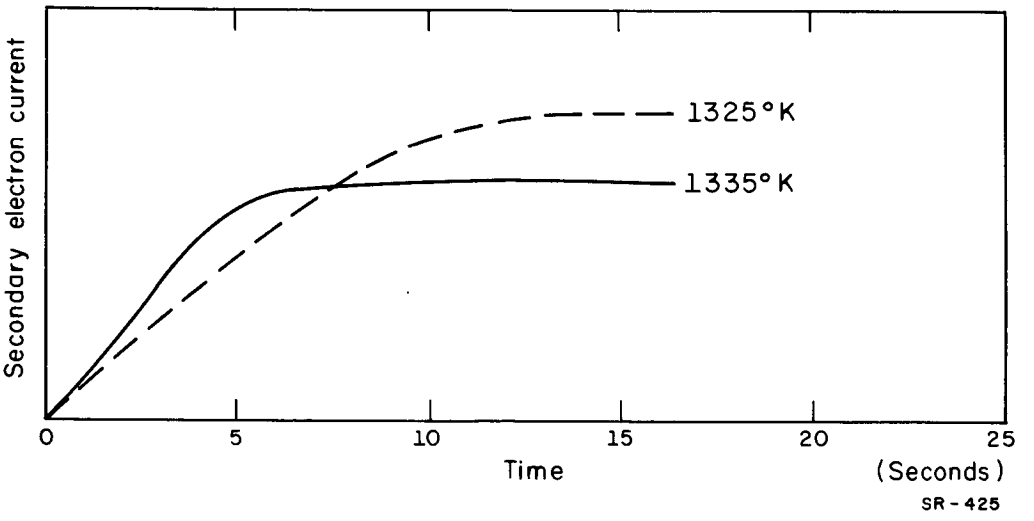

Figure 34. Isothermal Auger yield change during desorption of the highest energy state of CO bound on (111) W.

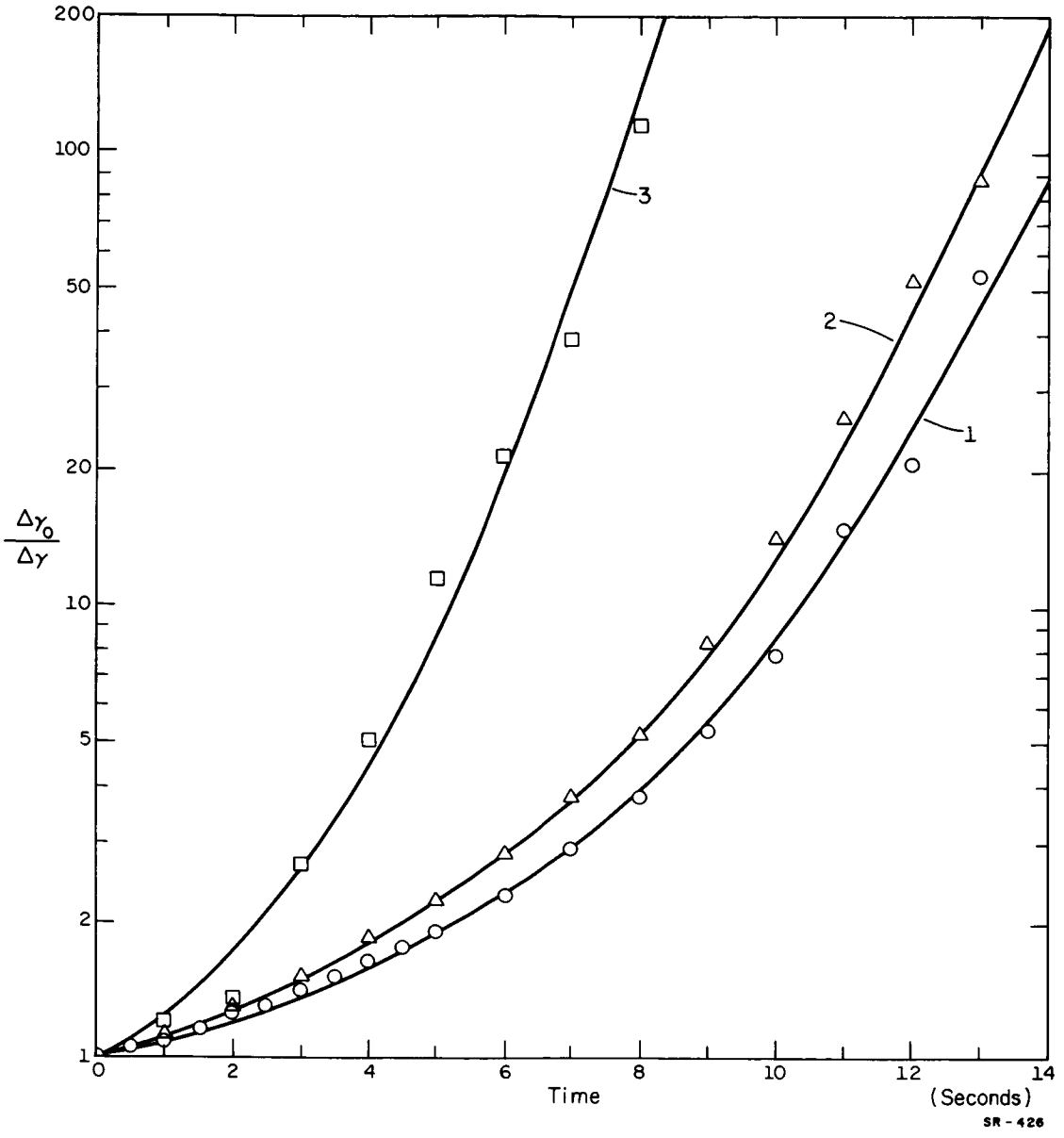

Figure 35. Desorption rate curves for the high energy state of CO on (111) tungsten. These three curves were taken at progressively higher temperatures.

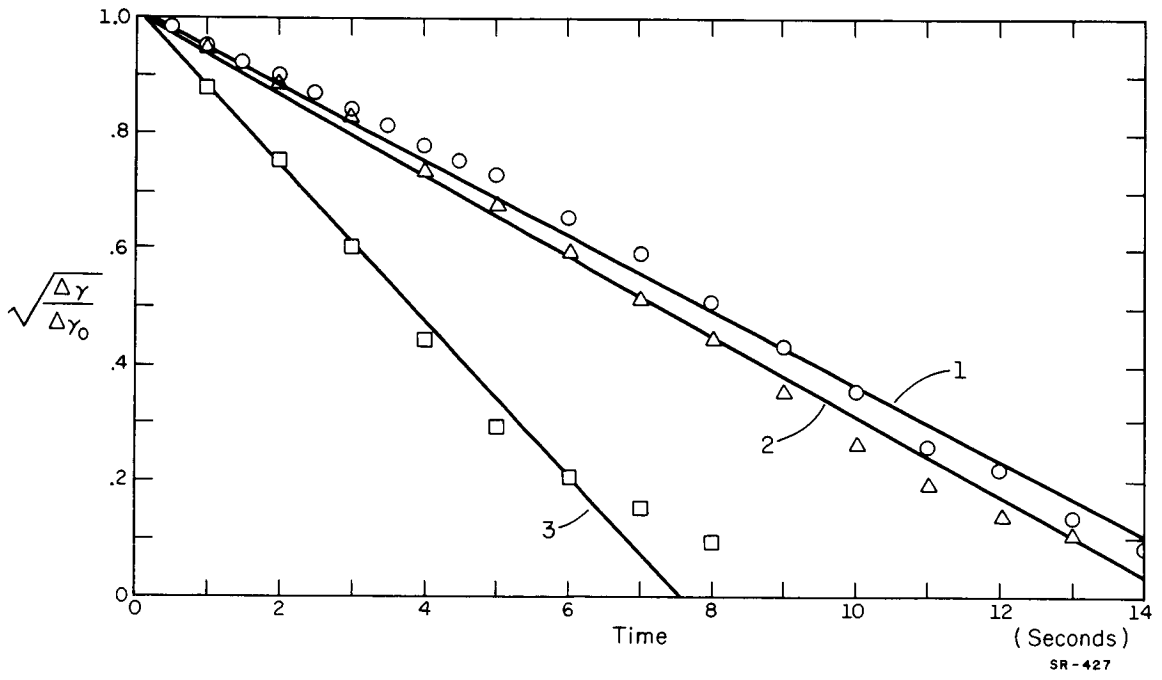

Figure 36. CO desorption rate curves for the high energy state of CO on (111) W plotted on a 1/2 order diagram. These curves are taken at progressively higher temperatures.

In searching for the reason for this behavior, one would be inclined to question the validity of eq. 39 before questioning eq. 1. For instance, it is conceivable from Figures 17 and 18 that, for some region of values, the yield change could vary as,

$$\Delta\gamma = An^m . \tag{41}$$

Here we would not expect m to be too much different from unity. However, for a first order desorption process, for all m,

$$-\frac{d(\Delta\gamma)}{dt} = m\Delta\gamma\ \beta(T) , \tag{42}$$

and as we have already seen in section B, the form of the first order desorption equation remains essentially unchanged. For a second order process, and any m.

$$-\frac{d(\Delta\gamma)}{dt} = m\frac{(\Delta\gamma)^{(\frac{1}{m}+1)}}{A^{1/m}}\ \beta(T) . \tag{43}$$

Therefore, in order to observe $+1/2$ order desorption kinetics, $m = -2$, and

$$\Delta\gamma = \frac{K}{n^2} , \tag{44}$$

which would imply that $\Delta\gamma$ would increase as n decreases, in clear conflict with experimental data.

The β state of CO on (110) W is thus composed of a high energy pure state which appears to desorb with $\simeq 1/2$ order kinetics and a set of lower energy first order states.

Auger experiments show that the target cooled to 120°K has the same β states available for occupation as the target at room temperature. The α state vastly increases in population on the cooled target. Assuming that the Auger cross section for this state has the value measured for the polycrystalline W, the α state has a population of 18×10^{14} molecules/cm^2 at 120°K. The energies of these α states are very similar to those observed on (110) W. The total surface population at 120°K will then be 24×10^{14} molecules/cm^2.

4. N_2 on Polycrystalline Tungsten

Figure 37 shows a series of flash filament experiments illustrating the growth of the adsorbed β state of N_2 on polycrystalline W. These results indicate that there is a compact adsorption region with a saturation coverage corresponding to 2.7×10^{14} molecules/cm^2 on the surface. Assuming, for purpose of comparison only, first order desorption and $\nu = 1.6 \times 10^{13}$, the peak desorption energy is 3.91 eV.

The center curve of Figure 38 is the relative surface coverage determined by the flash filament technique with adsorption at room temperature, made at a pressure of about 2×10^{-8} Torr of N_2. The sticking coefficient at low coverage calculated from this curve is 0.37.

For N_2, no Auger yield change curve was made under conditions comparable to those for the flash filament curve above. However, the two other curves of Figure 38 compare relative changes in Auger yield for the surface held at different temperatures and exposed to N_2.

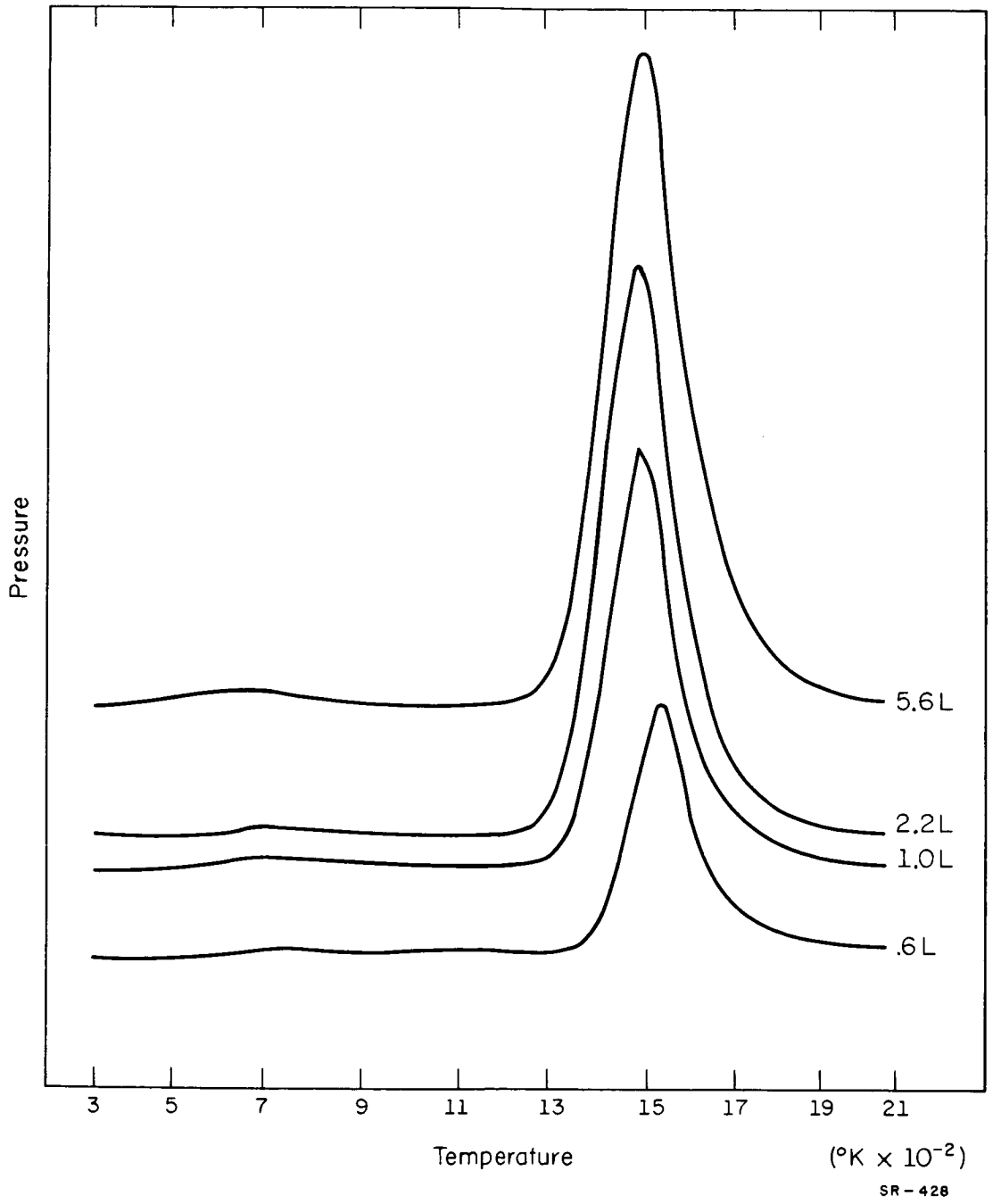

Figure 37. Flash filament desorption spectra of N_2 adsorbed on polycrystalline W at 350°K.

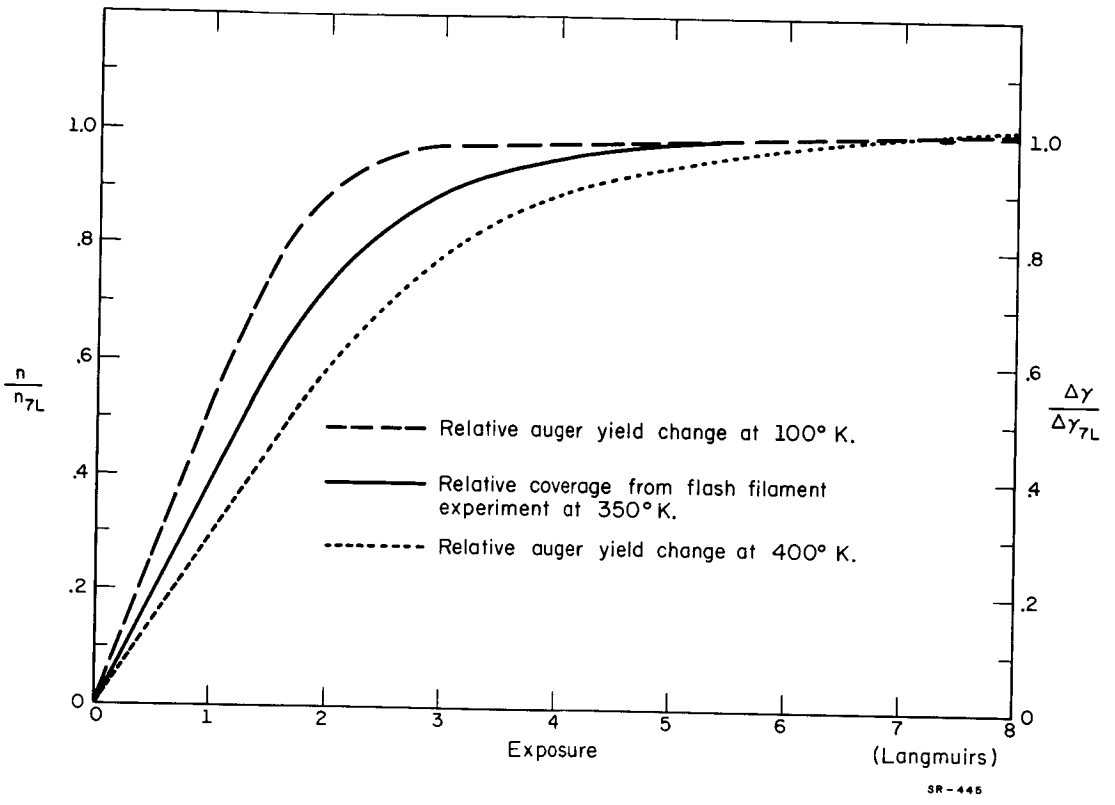

Figure 38. Comparison of relative coverage and relative Auger yield changes at two different temperatures for the adsorption of N_2 on polycrystalline W.

The top curve was made for the target held at $\sim 100°K$, and the bottom curve was made by flashing the target (with empty cooling reservoirs) in $1x10^{-7}$ Torr of N_2 and continuously measuring the yield decrease over a period of 100 sec after the flash. During this time the target continued to cool and had a higher average temperature than for the flash filament curve. The differences in slope of these curves represent differences in the sticking coefficient of N_2 on W at the different temperatures. An Auger yield change curve made at a temperature comparable to that of the flash filament curve would lie somewhere between these two extreme curves, and would give an Auger cross section similar to those observed for CO and H_2.

Auger experiments also show that most of the β desorption takes place in a small temperature region. However, just as for CO on the polycrystal, a multiplicity of Auger endpoints is found, indicating a continuous band of states over this small range. When the individual yield changes are plotted on the first order diagram, they show the convex upward characteristic of closely spaced multiple states. The average Auger cross section of the β state is 0.15.

When adsorption occurs on the target held at 120°K, the β state has identical desorption energies. However, the Auger yield change associated with β adsorption increases, indicating that the population in the β state increases at saturation to about $3.7x10^{14}$ molecules/cm^2 compared to $2.7x10^{14}$ at room temperature.

A new set of adsorbed states, which we shall call the α

states, also appear at very low energies. Although the Auger yield change associated with the desorption of this set of states is small, pressure bursts in the system indicate that it consists of a large number of molecules. Auger desorption spectra show they are bound with energies of .5-.9 eV. If the Auger cross section is assumed to be 0.01, the same as that measured for a similar state of N_2 on (111) W, the coverage of this phase of adsorbed N_2 could range to 6×10^{14} molecules/cm^2.

5. N_2 on (110) Tungsten

To within the limit of detection of this apparatus, there is no discernible adsorption of N_2 on (110) W at 300°K. Figure 39 compares the desorption spectra of the target after exposure to 5.2×10^{-8} Torr of N_2 for 650 sec, and after exposure for 650 sec to the background gases. The spectrum made at high pressure has more noise than the one made at background pressure. The maximum coverage may be calculated to be $< 10^{+13}$ molecules/cm^2. This is in close agreement with the results of Ehrlich.[5] This observation is confirmed by Auger measurements.

If the target is cooled to 120°K, N_2 begins to adsorb in a very low energy, very sharp state (Figure 40) which we shall call the γ state. The γ state can form in layers with density higher than 7×10^{14} molecules/cm^2 with a sticking coefficient 0.11. It possesses an Auger cross section of 0.10.

When the Auger current is observed during desorption (Figure

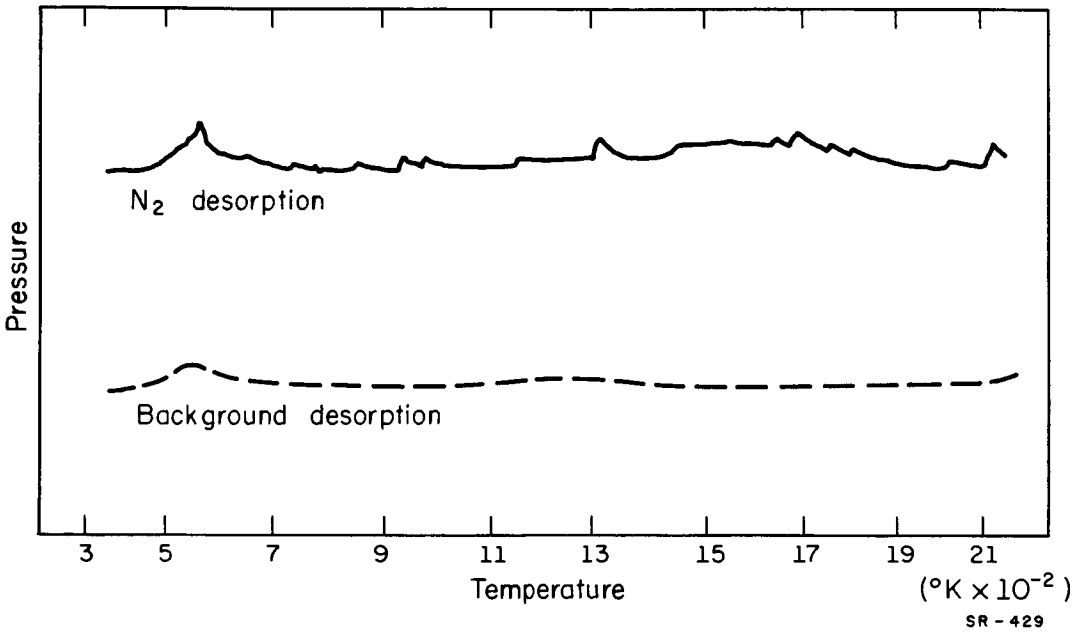

Figure 39. Flash filament desorption spectra of (110) W exposed to N_2 at 5.2×10^{-8} Torr for 650 sec (full line), and to the background gases for 650 sec (dashed line).

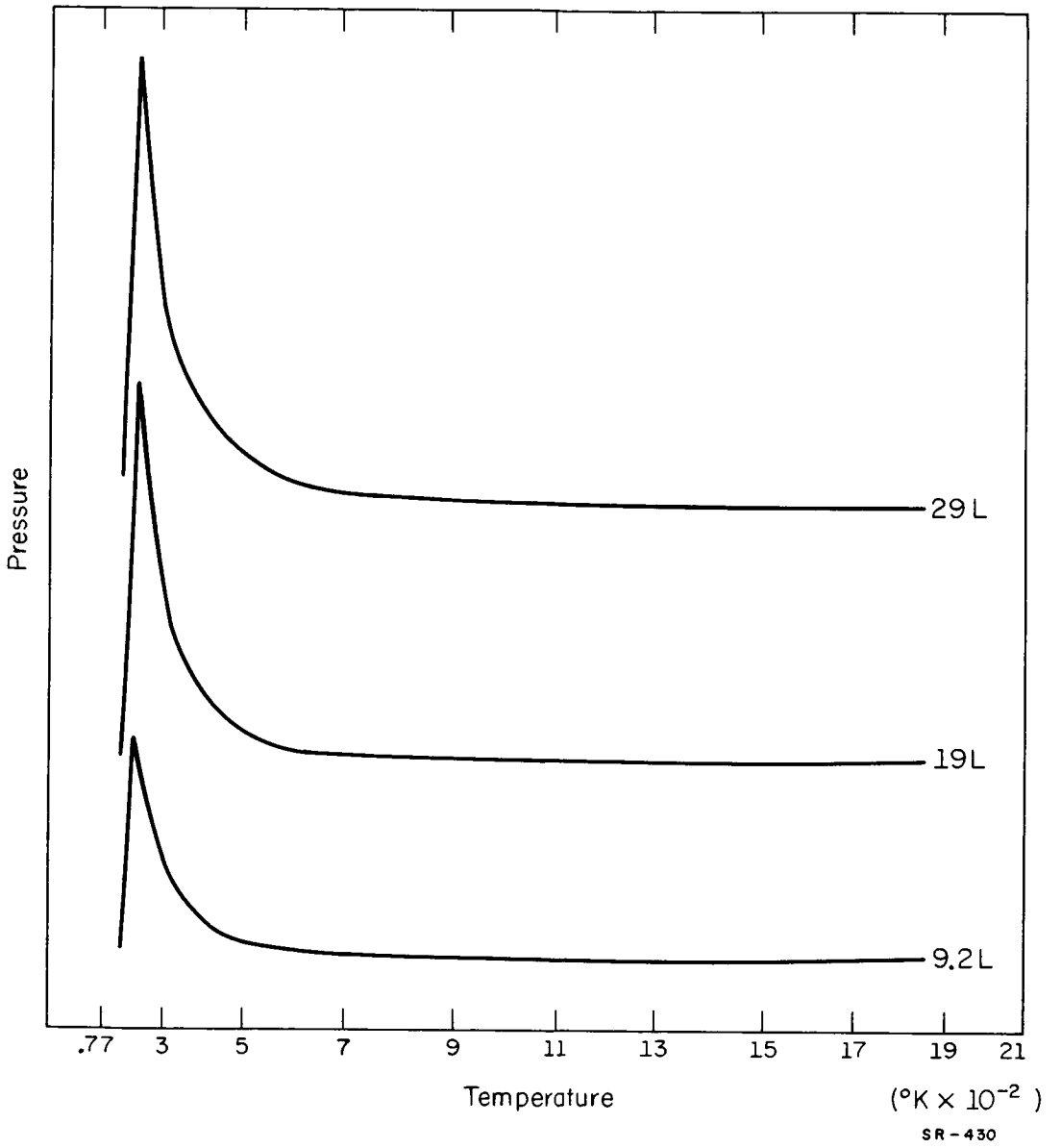

Figure 40. Flash filament desorption of γ N_2 adsorbed on (110) W at 120°K.

41), it is seen that the γ state is simple, no matter how slowly desorption proceeds. That is, no equilibria can be obtained other than that for complete desorption, no matter how small β is for the desorption temperature selected.

When the relative yield changes are plotted against time for several of these desorptions, straight lines result on the logarithmic plot of Figure 42. This implies a pure first order desorption. Assuming $\upsilon = 1.6 \times 10^{13}$ cycles/sec, the desorption energy is 0.61 eV. The same energy is calculated from the flash filament peak.

Since the desorption constant β depends on the ratio of binding energy and T, both of which are very small in this case, a given variation in T affects β more strongly than at higher temperatures. For this reason we were not successful in measuring β consistently as a function of T in this simple desorption state.

Since the exponential drop of the flash filament spectrum high energy tail has a time constant larger than τ, the vacuum system time constant, there is obviously some damping present, although not nearly so much as was observed with CO. This is consistent with the fact that the freezing point of CO is 5°K higher than that of N_2, and the vapor pressure of N_2 is slightly higher than that of CO at any low temperature.

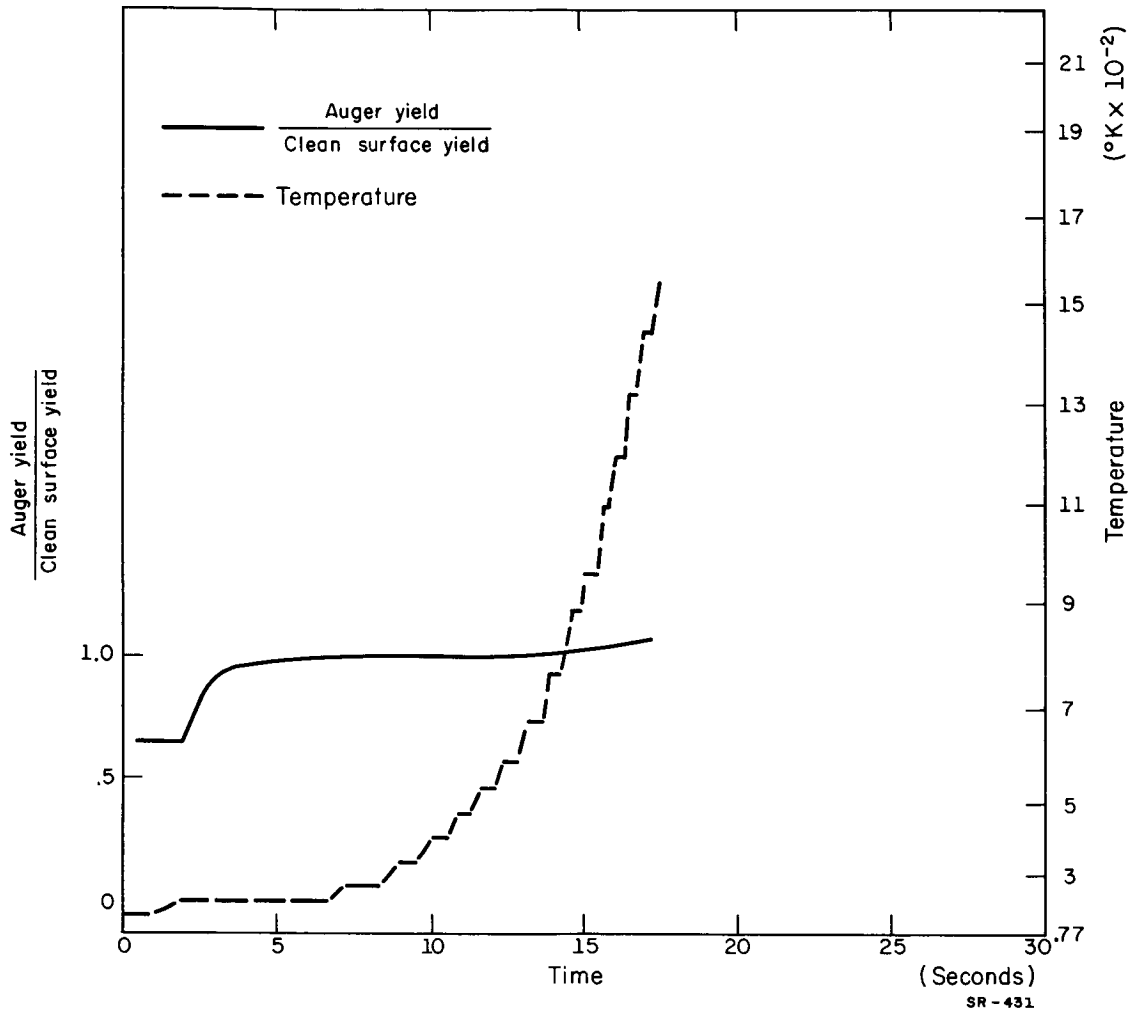

Figure 41. An Auger desorption experiment: N_2 adsorbed on (110) W at 120°K.

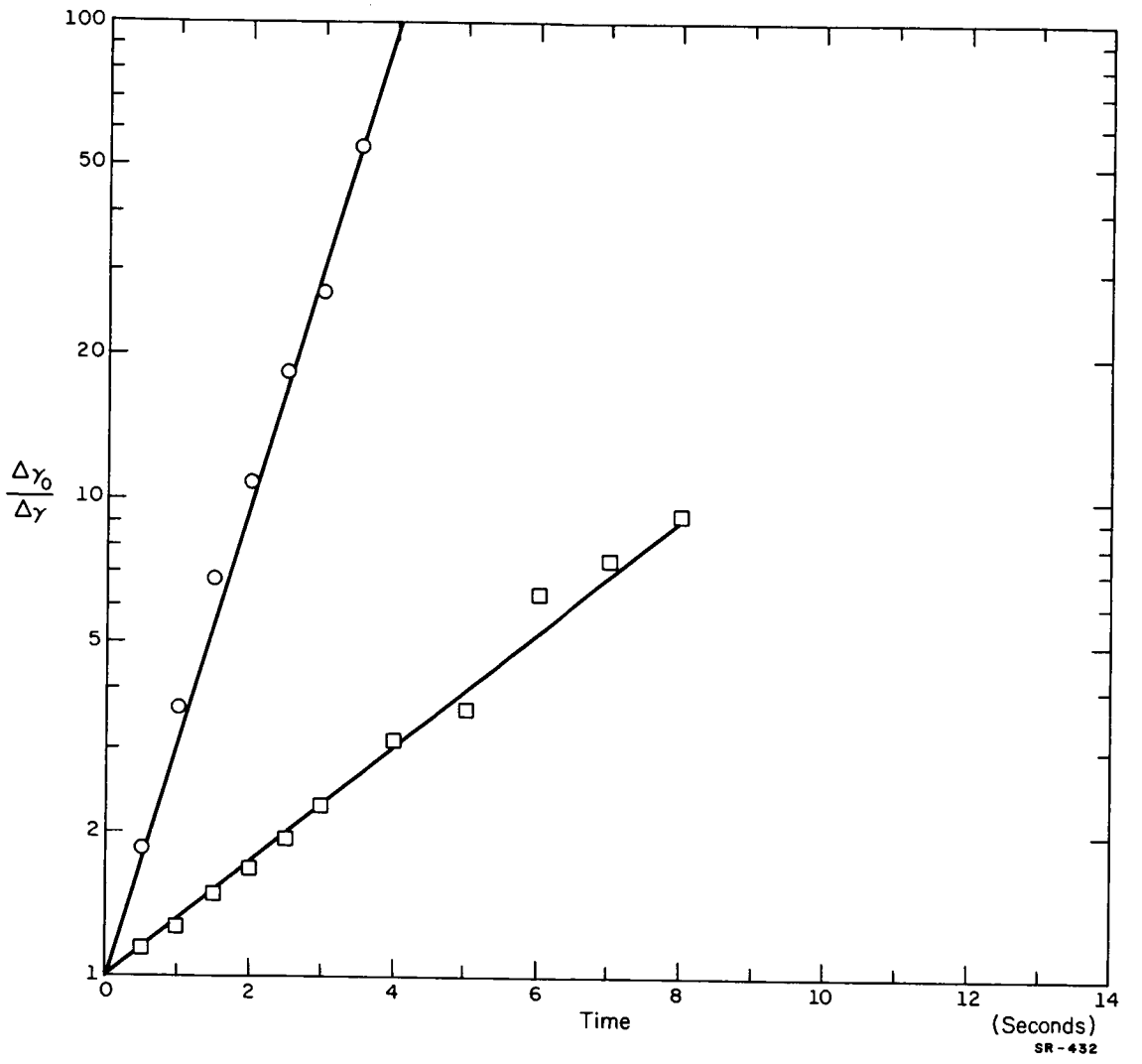

Figure 42. Desorption rate curves for the γ state of N_2 on (110) W.

6. N_2 on (111) Tungsten

N_2 adsorbs on the (111) face of W with an unusually low sticking coefficient. At 300°K, a monolayer, instead of being completed after 6L, requires 600L. Figure 43 shows flash filament desorption curves taken at several initial coverages. One sharp desorption peak at 3.65 eV is the only β state observed. It covers the surface to a density of 6.6×10^{14} molecules/cm^2 at saturation and adsorbs with a sticking coefficient of 0.0038. Some of these charts show a small background H_2 desorption state at 1.65 eV, whose Auger cross section is equal to that observed for H_2 adsorbed on (111). Also, growth of the α state of N_2 can be seen at even lower temperatures, peaking around 0.74 eV. Both of these states are made visible by the long time required for β adsorption on this face allowing the target to cool to very near ambient room temperature.

In the highest coverage spectrum, both these states have merged, due to the filling of the H_2 distributed state (see section 7 below).

The Auger cross section for N_2 adsorbed in the β state is 0.085, about half that for the polycrystalline target. All experiments indicate that this β state desorbs as a single state, since there is never a termination of isothermal desorption (Figure 44) except when all β-sorbed gas has left the surface. When this yield change is plotted (Figure 45) on a logarithmic $\frac{\Delta\gamma_o}{\Delta\gamma}$ plot, a very nice straight line results, indicating first order desorption from a simple state.

This experiment can be performed at several different

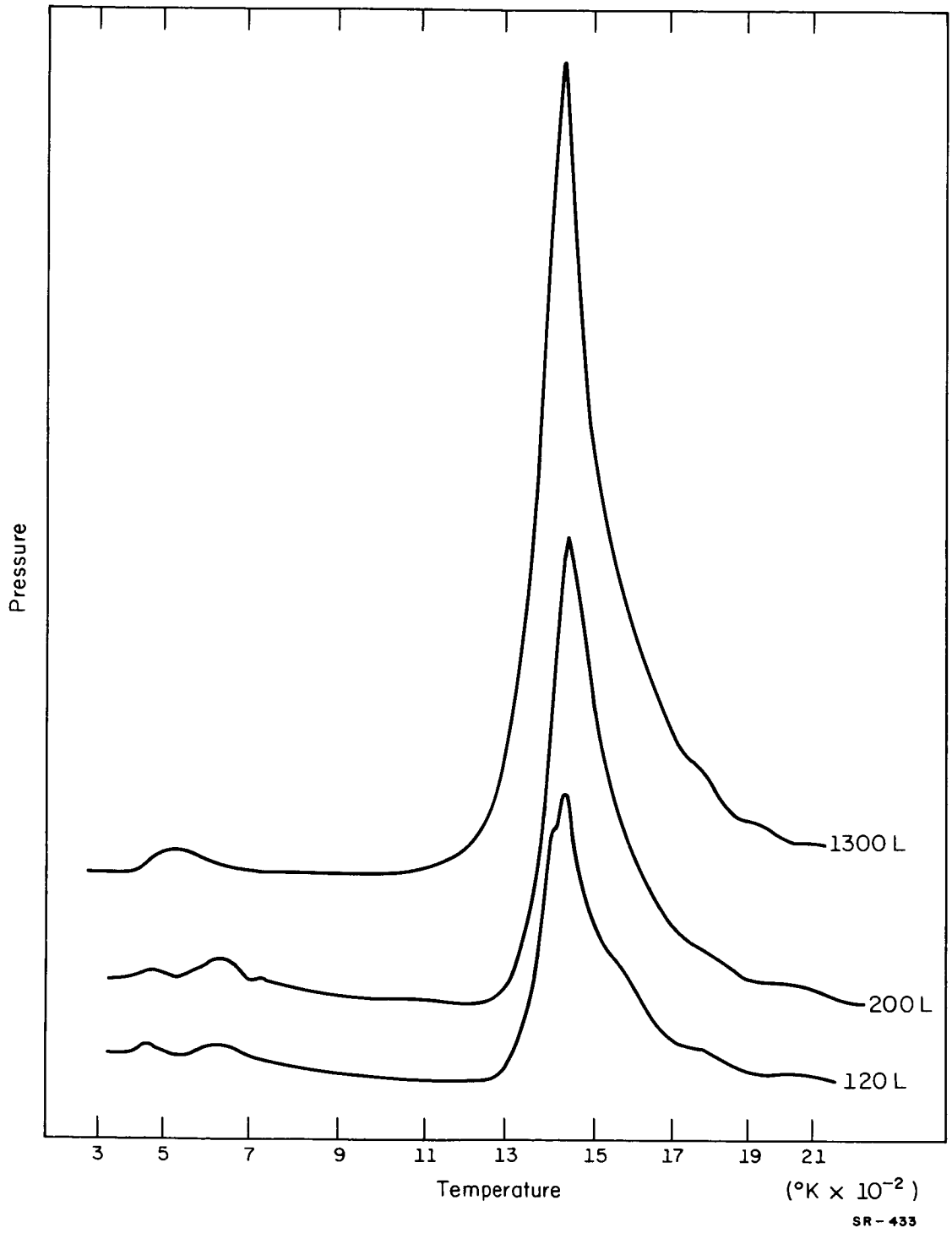

Figure 43. Flash filament desorption spectra for N_2 adsorbed at 300°K on (111) W.

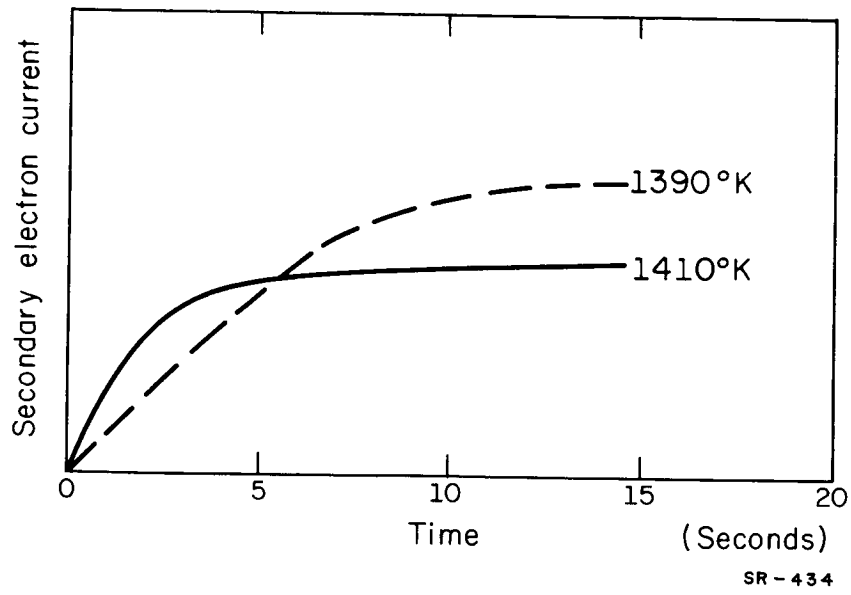

Figure 44. Isothermal Auger yield change during desorption of β N_2 from (111) W.

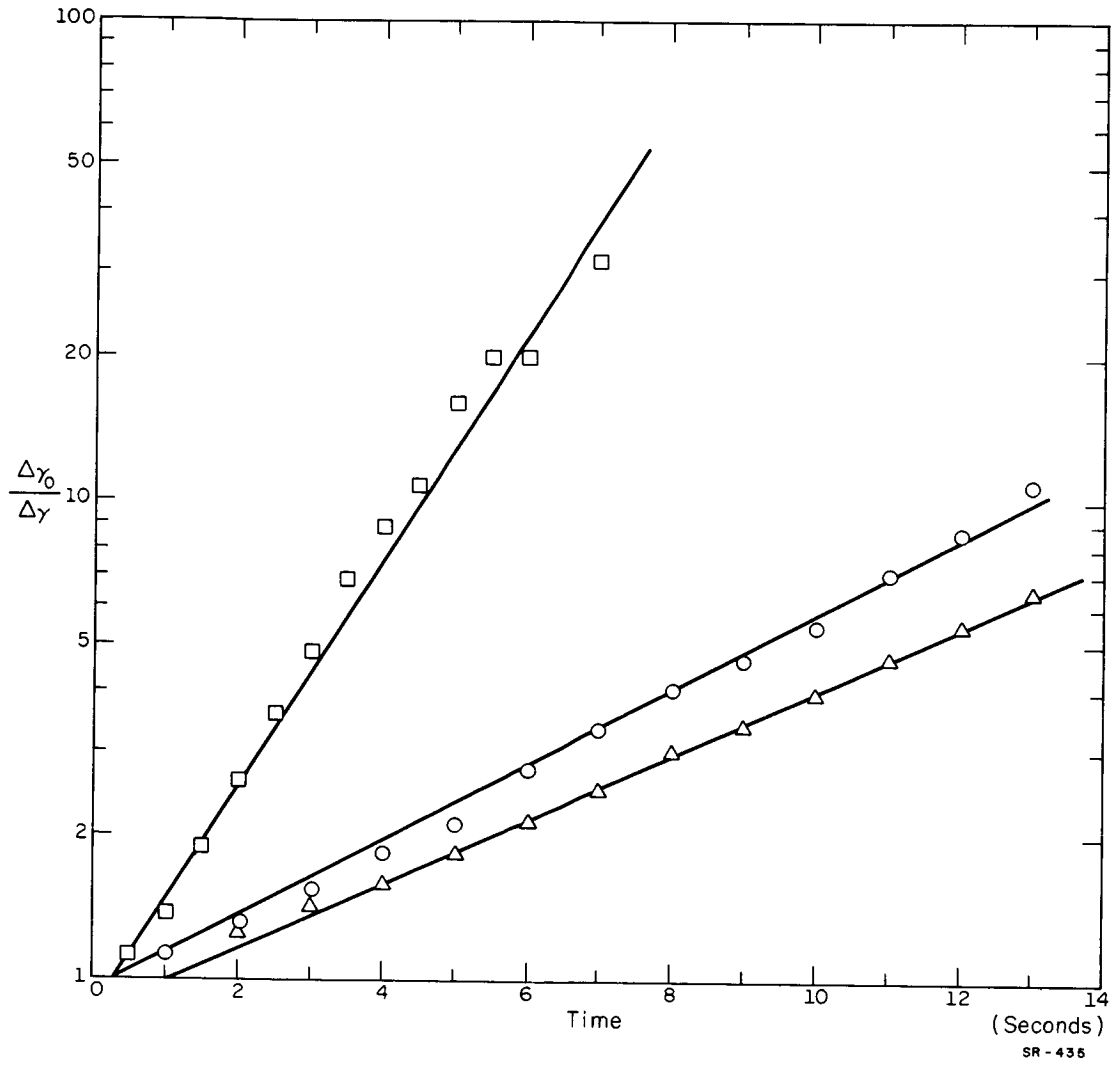

Figure 45. Desorption rate curves for β N_2 on (111) W.

temperature values so that β can be determined as a function of T. When log β is plotted vs. $\frac{1}{T}$, (Fig. 46), it can be seen that a straight line results. This indicates a constant value of activation energy in this region, i.e.

$$\beta = \nu e^{-E/KT}. \tag{45}$$

Since the response of the collector electrometer is 1.65 sec^{-1}, the electrometer response to a square current pulse will be,

$$I = I_o (1 - e^{-(1.65)t}). \tag{46}$$

Because of this electrometer response time, the measured values of β at the high frequency end of this chart will be slightly smaller than the true values. The values corrected for the electrometer response are indicated. These corrected points are used with the other points to calculate the slope and y - intercept of the least-mean-square deviation straight line. From these values we obtain

$$E_\beta = 3.62 \text{ eV}$$

and

$$\nu = 1.88 \times 10^{12} \text{ sec}^{-1},$$

values in very close agreement with what we could expect.

Auger experiments on the target cooled to 100°K reveal the appearance of a low temperature α' state similar in energy range and fractional Auger yield change to the α state of N_2 on the polycrystal. There is no indication of a sizeable simple γ state of large Auger cross section. Figure 47 shows flash filament spectra which indicate

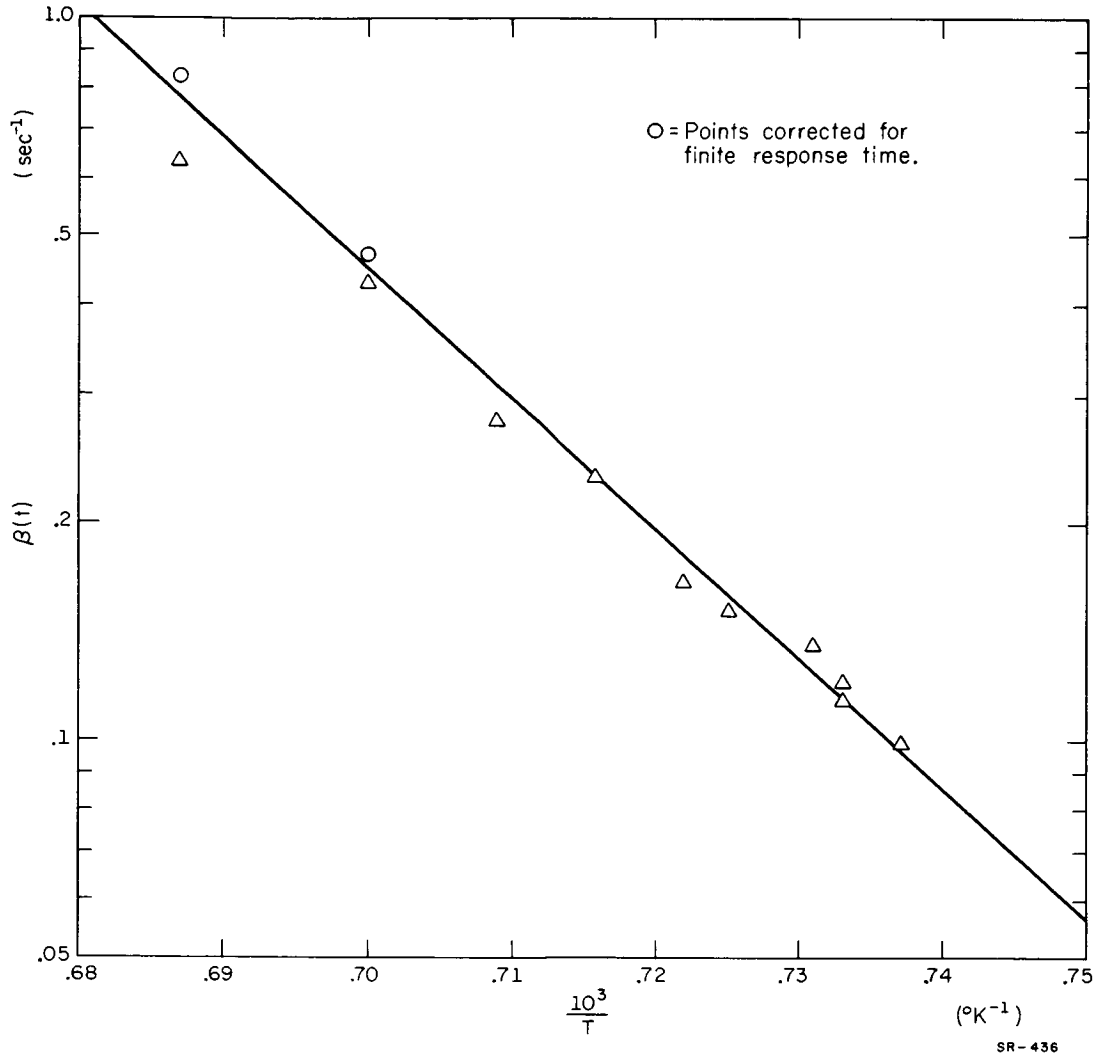

Figure 46. Temperature variation of the desorption constant of β N_2 from (111) W.

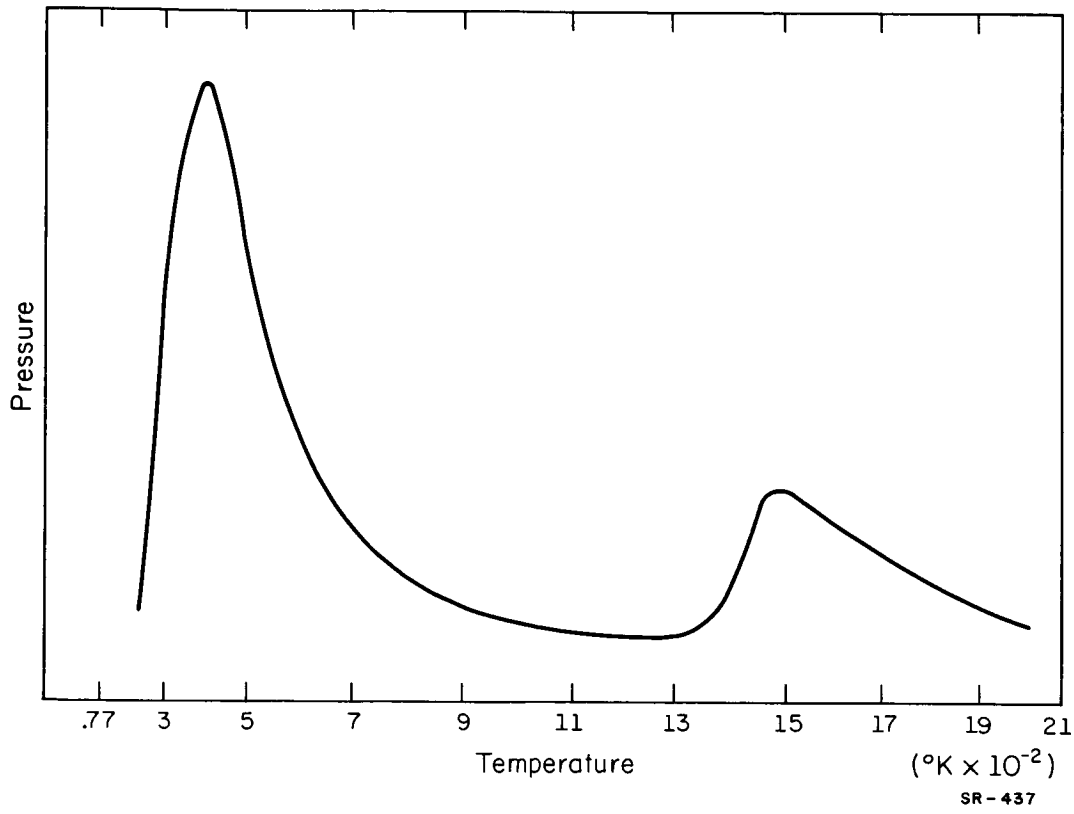

Figure 47. Flash filament desorption spectrum of N_2 adsorbed on (111) W at 120°K.

that the number of molecules adsorbing into the α state grows to be much greater than the number in the β state. The number of α molecules grows to be at least 13×10^{14} and possibly larger.

7. H_2 on Polycrystalline Tungsten

Figure 48 shows flash filament desorption spectra of H_2 from polycrystalline W for several initial coverages. Curves 1 and 2, at 0.3 and 0.6L, show only the filling of a broadly distributed low energy state with peak desorption energy corresponding to about 1.52 eV. A sharper peak forms at higher coverage and corresponds to an energy of 1.26 eV. Since these states fill from the high energy end, a gradual decrease in the calorimetric heat of adsorption would be observed.

The amount of H_2 held on the surface at saturation is 3.3×10^{14} molecules/cm^2. As we have seen, Figure 19 compares the amount of gas held on the target at any time measured by flash filament desorption with $\frac{\Delta\gamma}{\Delta\gamma_{5L}}$, the Auger yield change associated with adsorption. The sticking coefficient measured from the inception of the flash filament curve is 0.23.

Analysis of Auger desorption experiments shows that the broad desorption region is actually a set of very closely packed states. A typical desorption rate curve shows the decreasing slope closely corresponding to the results we have calculated for densely packed states.

Hagstrum[34] has hypothesized that H adatoms may diffuse into the bulk at high temperatures during surface cleaning and then re-

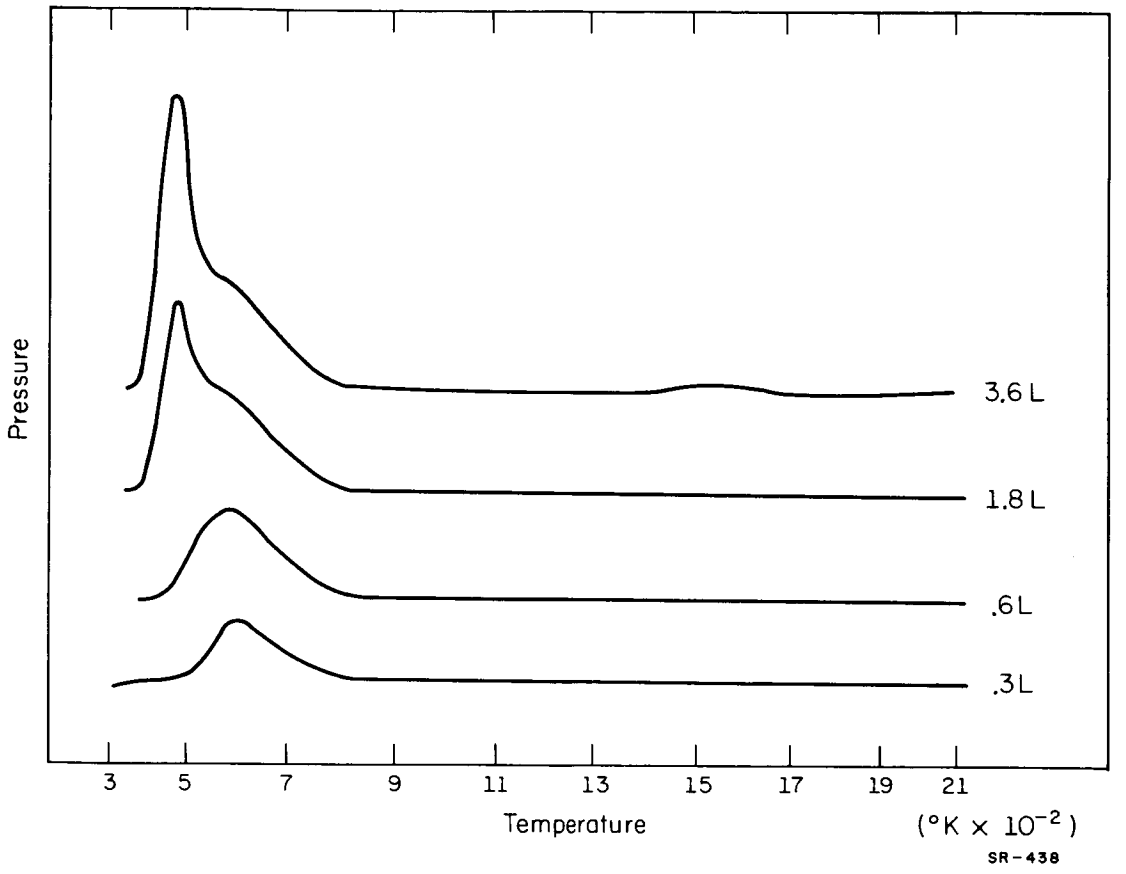

Figure 48. Flash filament desorption spectra for H_2 adsorbed at 350°K on polycrystalline W.

diffuse out to the surface as the interior cools. This would alter the flash filament results since not all the particles adsorbed on the surface would enter the gas phase and raise the pressure in the system.

In order to check this possibility, the following experiment was performed several times. The target was cleaned and heated to several different temperatures, while observing the Auger yield. Then it was allowed to cool. No decrease in Auger current was observed but a uniform one, that due to readsorption. Diffusion of a significant fraction of a monolayer of bulk H atoms onto the surface on cooling should cause a noticeable decrease in Auger current. Therefore, it appears that H does not diffuse from the interior of clean tungsten onto the surface in amounts comparable to a monolayer.

As the target is cooled to 120°K, more even lower energy states are open for occupancy, and the saturation surface coverage rises to 3.7×10^{14}, as obtained from the increase in Auger yield change associated with desorption. These states extend down to 0.8 eV at saturation coverage up to a high energy limit around 1.8 eV with an average peak energy around 1.52 eV.

8. H_2 on (111) Tungsten

Figure 49 presents some flash filament desorption curves for various initial coverages of H_2 from (111) tungsten. The lower line is a desorption curve taken at room temperature, whereas the two upper lines were taken for adsorption at 120°K.

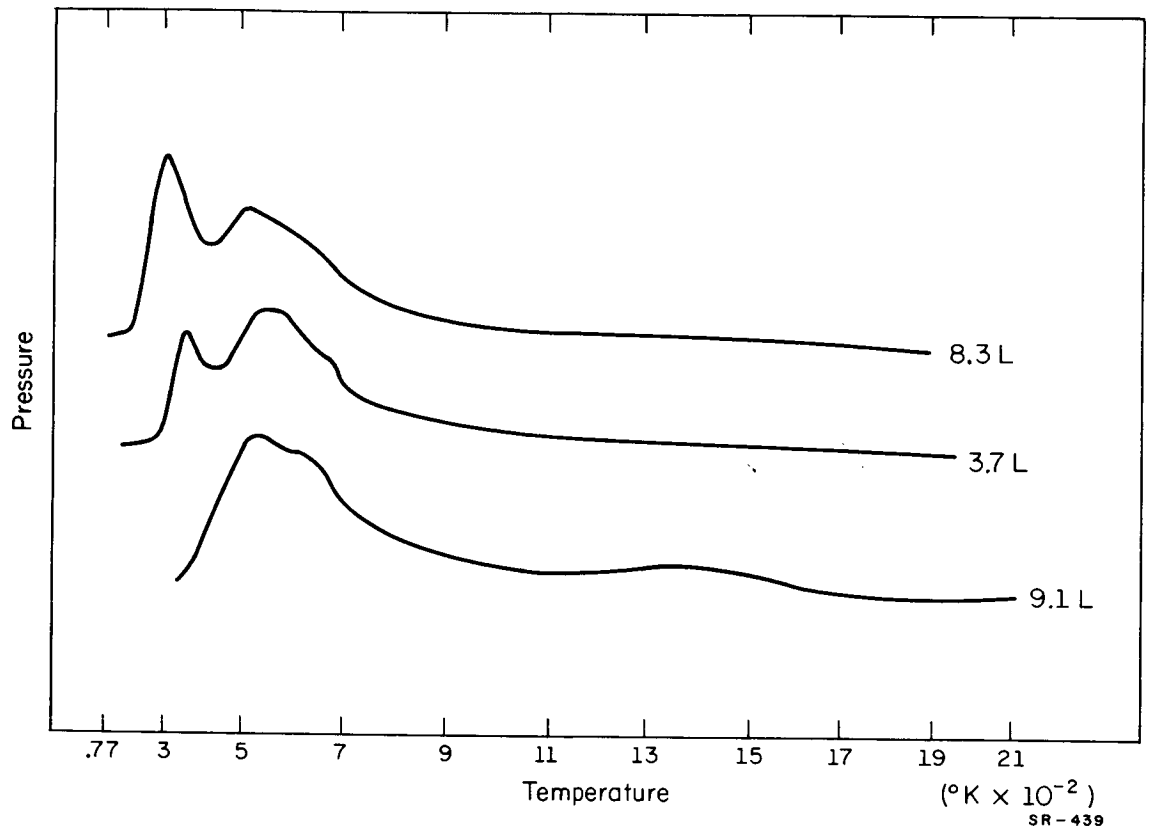

Figure 49. Flash filament desorption spectra for H_2 adsorbed at 350°K and 120°K on (111) W.

Again we see that, at room temperature, H_2 is adsorbed in a broad band of states peaking around 1.5 eV. The cooled target allows even lower energy states to be filled. Saturation coverages (at about 10L exposure) range from 3.5×10^{14} molecules/cm^2 for the room temperature target to 4.2×10^{14} molecules/cm^2 for the 120°K target. At low temperatures, another sharp desorption peak at 0.96 eV begins to appear.

The Auger cross section for H_2 adsorbed on this face is only slightly less than for H_2 adsorbed on the polycrystal, allowing desorption to be easily observed by this method. Again many equilibria may be reached during desorption, indicating a densely parked set of states between 0.9 eV and 1.8 eV.

9. H_2 on (110) Tungsten

Figure 50 shows the desorption of various initial coverages of H_2 from (110) tungsten. In general form, these desorption curves are similar to H_2 desorption from the polycrystal. From the pressure peaks, binding energies ranging from 1.60 to 1.40 eV for H_2 adsorbed at 300°K may be calculated. However, on this face the sticking coefficient is 0.015, much less than on the polycrystal. Saturation coverage is also less, being about 1.3×10^{14} molecules/cm^2. When the target is cooled to 120°K (top line of Figure 50), the low energy states again are filled so that saturation coverage on the face increases to 2.5×10^{14} molecules/cm^2. As Figure 50 shows, a well defined peak appears at 1.00 eV, and another peak appears to be forming at 0.65 eV.

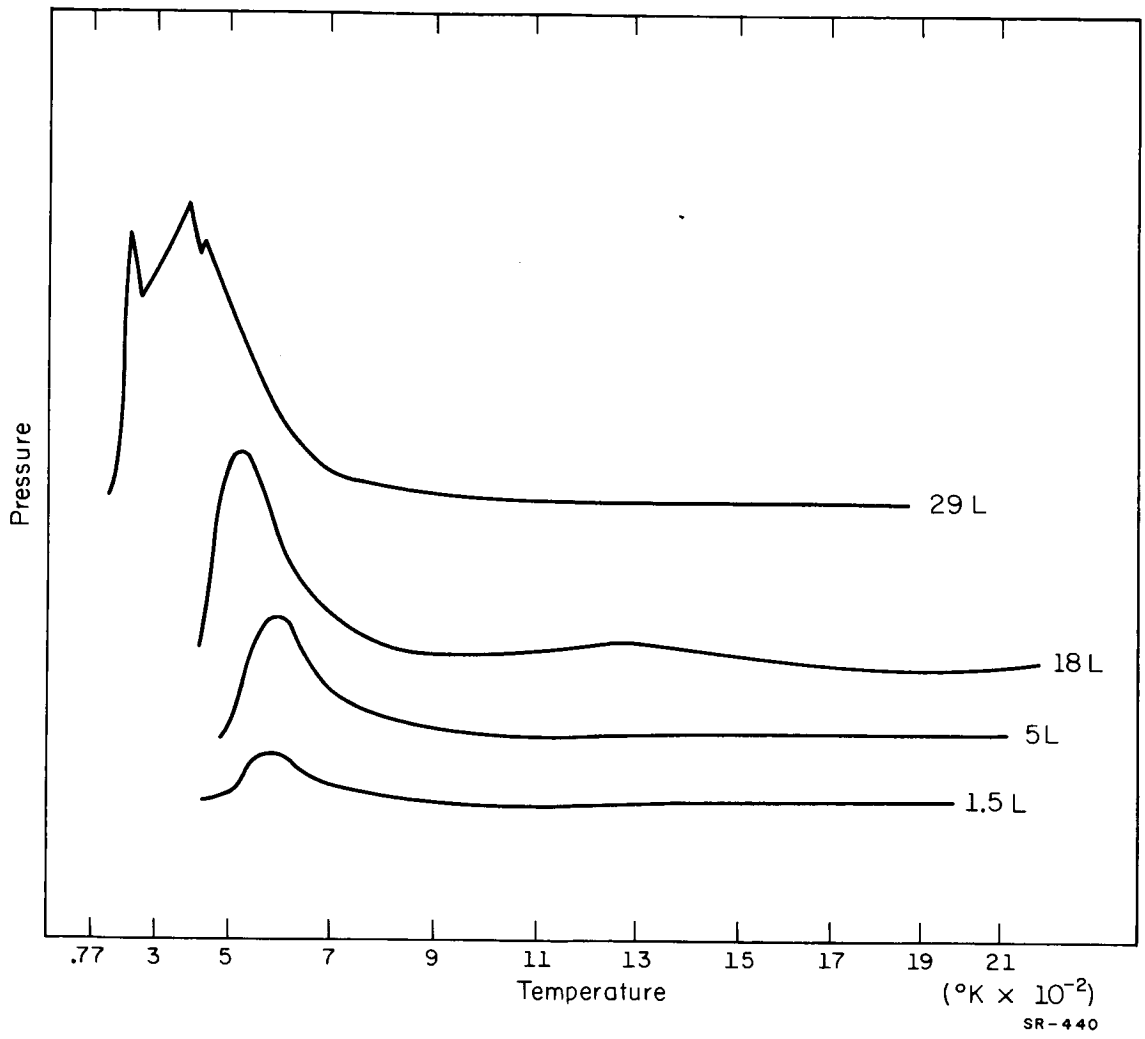

Figure 50. Flash filament desorption spectra for H_2 adsorbed at 350°K and 120°K on (110) W.

The Auger cross section was much smaller on this face than on polycrystalline W, dropping from 0.091 to 0.031. Thus, in the most favorable case, $\Delta\gamma$ is only 0.08 of γ_{CL} for the clean surface. This, coupled with the lower surface coverage, made the sensitivity for the Auger process very small. The same pattern of distributed desorption states could be verified, but determination of desorption kinetics and energy state densities was not feasible at these sensitivities.

VII. DISCUSSION OF RESULTS

A. Introduction

Measurements have been made of quantities associated with the adsorbed states of CO, N_2, and H_2 on polycrystalline, (111), and (110) tungsten surfaces. These measurements allow us to make numerous tentative conclusions about the adsorbed state. These conclusions will be discussed in this chapter.

B. General Conclusions

One obvious result, confirming Ehrlich's earlier conclusion,[5] is that macroscopic surfaces can be prepared having consistent orientational properties for gaseous adsorption. Figure 39 is a striking demonstration of this. It shows that the (110) single crystal has completely different adsorption properties for N_2 than the polycrystalline sample. H_2 was also found to have Auger cross sections differing by a factor of 3 on two different single crystal planes, showing that the Auger properties of adsorbed layers on different tungsten crystal faces may also vary widely.

Another result of basic importance in our work is the observation that Auger yield is independent of temperature between 100°K and 2300°K. At present, the lack of knowledge of the phonon distribution in tungsten and the excitation depth and angular distribution of Auger secondaries, precludes drawing basic conclusions about the nature of the Auger process from this observation.

Figure 51 summarizes our measurements on the adsorbed states of gases. The height of the peak for each binding state represents the relative saturation coverage of that state of 120°K. Note that the α and γ state coverages of N_2 and CO may actually be higher than our measurements because we usually did not attempt to get full saturation values. Cross hatched areas represent states of multiple desorption energies, whereas states drawn as solid lines desorb with simple kinetics. The value of the average Auger cross section for each state is written beside it.

C. Cross Sections

For convenience, we have used a somewhat unusual definition of cross section. We have defined

$$\sigma = \frac{\text{fractional decrease of Auger electrons of energy above 7.5 eV}}{10^{14} \text{ adsorbed molecules/cm}^2},$$

This number would be close to, but slightly smaller than, the fraction of Auger electrons scattered out of the high energy tail of the distribution in the theory of Propst and Luscher.

Usually, one thinks of a scattering cross section as the probability of scattering of an incident particle from one target particle per cm^2. This quantity is just 10^{-14} times that which we have been reporting, and would give the cross section in cm^2.

The data of Propst and Luscher is compared in the table below with our own results for polycrystalline W. As before, all $\Delta\gamma$'s refer to the

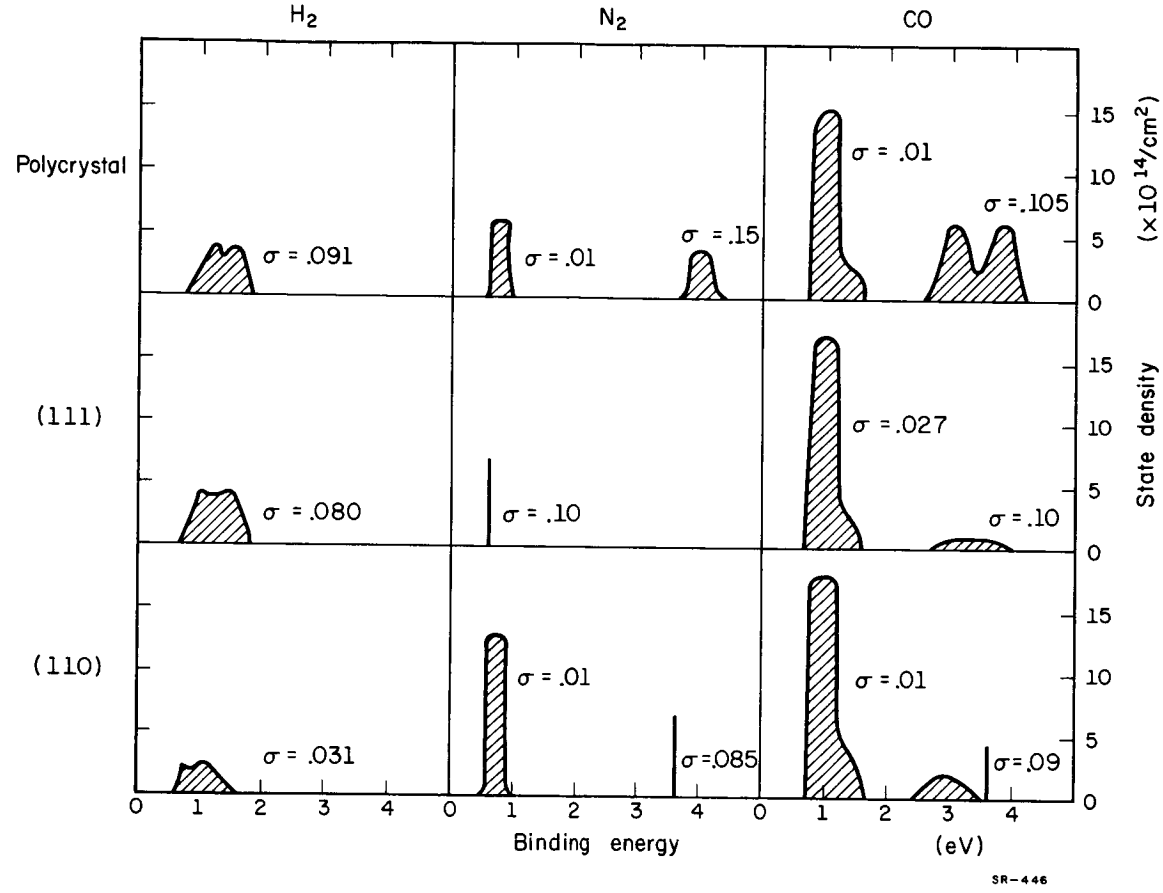

Figure 51. State density summary for adsorption of gases on tungsten at 120°K. Simple states are represented as straight lines with height equal to the maximum population of the state. Multiple states are represented as areas with maxima equal to the maximum population.

portion of the Auger yield made up of electrons with energy larger than 7.5 eV. γ_{CL} is the clean surface yield. $\Delta\gamma_{H_2}$ is the change in yield on H_2 adsorption, with the surface covered to saturation at room temperature. $\Delta\gamma_{N_2}$ is the corresponding quantity for N_2.

TABLE 3

	Propst and Luscher	This Work
$\frac{\Delta\gamma_{H_2}}{\gamma_{CL}}$	.36	.30
$\frac{\Delta\gamma_{N_2}}{\gamma_{CL}}$	.49	.41
$\frac{\Delta\gamma_{N_2}}{\Delta\gamma_{H_2}}$	1.36	1.35

Because of the completely different geometry of electron collection in these experiments, the discrepancy in first two rows is not surprising. Propst and Luscher collected nearly all the secondaries, whereas we collected only those between 12° and 47° of the normal. A shift in the angular distribution of secondary electrons away from the surface normal as gas adsorbs could account for these differences. However, unless the angular distribution changes are different with each species of adsorbed gas, the ratio of the yield decrease for different gases would be similar for the two geometries. This ratio is the same for the two sets of results. Propst and Luscher have shown that these cross sections are of a reasonable magnitude for electron-electron scattering.

D. Adsorption Equilibrium

Flash filament experiments have not answered the fundamental question: "Do molecules occupy an equilibrium distribution as they are adsorbed on a surface at low temperature, or do they merely desorb from an equilibrium distribution after rearrangement during the desorption cycle?"

Auger experiments indicate that gases do indeed occupy equilibrium distributions from the moment of adsorption for the range of temperatures used here. Firstly, for CO, a gas whose sticking coefficient does not vary much between 300 and 400°K,[21] curves taken showing the Auger yield decrease during a 100 sec. adsorption interval at high pressure show the same $\Delta\gamma$'s as those measured from desorption experiments. Migration into states of higher Auger cross section between adsorption and desorption would result in $\Delta\gamma$ measured from desorption experiments being greater than $\Delta\gamma$ measured from adsorption experiments.

Secondly, as a surface is heated above the temperature at which adsorption has taken place, through the temperature range at which migration is expected, an increase in $\Delta\gamma$ corresponding to migration from states of low binding energy and low cross section to states of high binding energy and high cross section would be expected. This phenomenon was never observed.

This evidence is consistent with the hypothesis of intrinsic surface heterogeniety only if all the adsorbed molecules are free to

migrate to the high binding energy positions even at 100°K. The case where the range of binding energies is due to interactions between adsorbed atoms is consistent with the above observations even if diffusion is not possible.

E. Adsorption of Gases

1. H_2

In our work H_2 appears to be unique in that it never forms a pure state having a unique desorption energy. Rather, H_2 desorbs from a continuous spectrum of states, beginning at low coverages with the states of highest binding energy. When the surface is held at sufficiently high temperatures, the lower energy binding states may be above their desorption temperature, and hence unable to permanently bind gas. By the reasoning of the last chapter, this implies that the saturation coverage will vary with surface temperature.

Reasons for the apparent decrease in adsorption energy of H_2 and other gases have long been discussed. Some investigators attribute this decrease on polycrystalline tungsten to surface heterogeniety.[18,47] Others have attributed the decrease to the induced heterogeniety caused by the adsorbed particles on the surface.[48,49] If this were the case, the effect would be due to direct electronic overlap between the adsorbed molecules, as longer range forces will not give a great enough energy variation. In fact, the dipole-dipole interaction could account for only a 4 kcal/mole decrease in the heat of adsorption on a surface

covered with a monolayer of H_2.[50] As a surface begins to fill up with adsorbed molecules, the adsorbate electronic orbitals begin to overlap. The electronic energy states of the surface binding electron will be split, both because of the overlapping of the wave function of the adsorbate atom with the wave functions of the substrate and of the other adsorbed atoms. This splitting creates a band of states corresponding to different binding energies which gradually fills as the number of adsorbed atoms increases.

Temkin[51] has proposed that the surface binding electrons form a two dimensional electron gas. A calculation equivalent to the three dimensional calculation which yields the Fermi energy of a metal in the Sommerfeld model gives for the Fermi energy of a surface gas,

$$E_f = \frac{h^2 n}{4 \pi M} , \qquad (47)$$

where h is Plank's constant, n the number of adsorbed atoms per cm^2, and M the electronic mass. This energy will represent the maximum energy range of the surface electrons. For H_2 on W, it is about 50% too large. It is not surprising that this approximation is greatly in error, since the surface binding electrons can hardly be considered to be completely free; moreover this model does not take into account the nature of the surface at all.

Although the low magnitude and consistent range of binding energies tend to make us compare the H_2 binding states with the α states of CO and N_2, the Auger cross section of H_2 is definitely similar to the β rather than the α cross section of CO and N_2.

It is interesting that, even though saturation coverage of H_2 on (110) W is only 1/3 as great as on the polycrystalline or (111) surface, the range of desorption energies is the same. This would be the case if intrinsic surface heterogeneity alone were responsible for the range of desorption energies. To one performing a series of flash filament experiments at higher and higher coverage, the downward movement of the flash filament peak appears to be a shift in the desorption energy with coverage as in eq. 7. This expression clearly cannot encompass all of the peaking observed at the lower end of the flash filament desorption spectra.

It is more natural for one doing a desorption experiment at a fixed temperature (as our Auger desorption experiments) to think in terms of groups of states. This viewpoint is much more flexible and can account for flash filament data as well as eq. 7.

2. CO and N_2

The relations between the α and β states of CO and N_2 is quite intriguing. With the exception of the (110) surface, where N_2 does not bond at room temperature, α and β states exist simultaneously below $\sim$ 400°K. For both N_2 and CO, the β state can form without any large α state being present. The α state of CO can also form with only a small β state present. This is shown in the case of CO adsorbed in 110, where the α population is much larger than the β population even at room temperature. Thus the α state of CO is not necessarily a second adsorbed layer. None of our experiments at different heating rates

indicated measurable conversion of α state molecules into β state molecules before desorption.

Figure 52a shows a model of the exterior layer of atoms of a tungsten (111) surface. The lattice constant of body centered cubic tungsten is 3.16 Å, the covalent radius of W is 1.37 Å, and the triple bond radius of N is 0.55 Å. Under this crude hard sphere approximation, it can be seen that the N_2 molecules can fit in "binding wells" on the (111) surface at the rate of 1 molecule per surface tungsten atom. We would expect a CO molecule to be about the same size as a N_2 molecule. Our experimental results were that 6.4×10^{14} CO molecules/cm^2 and 6.6×10^{14} N_2 molecules/cm^2 adsorb in the β state on the (111) surface at saturation at 300°K. There are 5.8×10^{14} W atoms/cm^2 on this surface, so that, within a 10% error, there is one β state per surface tungsten atom for CO and N_2 molecules. This error of 10% is well within our previous estimate of the error in measurements of absolute surface coverages (Chapter V, Section D).

Figure 52b shows a model of the exterior layer of atoms of a tungsten (110) surface. The absence of a well developed β adsorption layer may be attributed to the smooth nature of the (110) face. No binding sites comparable to those on the (111) face allow the adsorbed molecules to fit "into" the surface.

As the surface is cooled, lower binding energy sites on the (111) and (110) faces become available. These sites can bind 3 CO molecules and 2 N_2 molecules per surface tungsten atom on the (111)

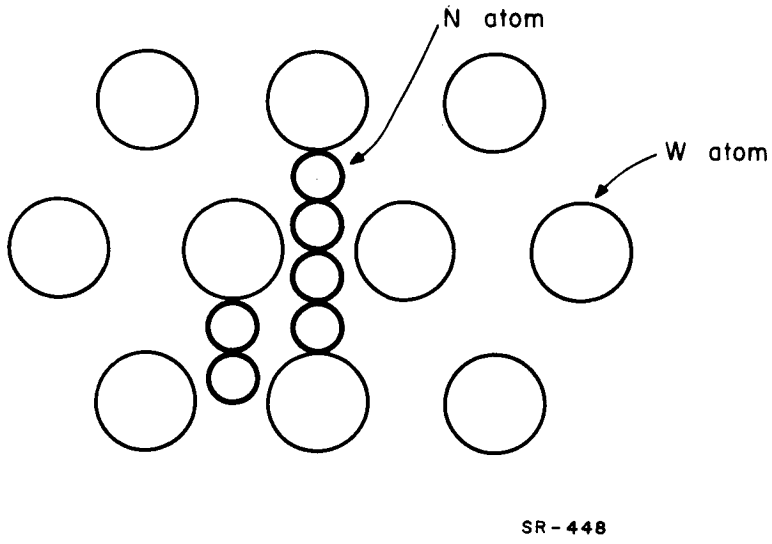

Figure 52a. Representation of the exterior layer of W atoms on the (111) surface including adsorbed N_2 molecules.

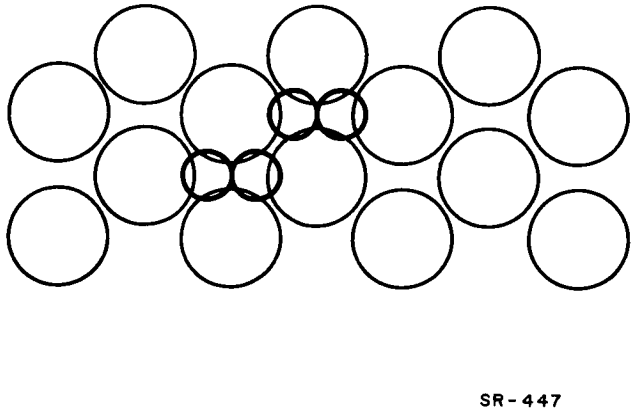

Figure 52b. Representation of the exterior layer of W atoms on the (110) surface including adsorbed N_2 molecules.

face. This large population clearly militates against any model featuring N_2 and CO molecules bound flat on the surface. The fact that the β-sorbed molecules inside the (111) surface's binding wells (surrounded by 3 surface W atoms) are much more strongly bound than the α-sorbed molecules, is one other convincing argument that there are great structural differences between the binding of the α and β states. The Auger cross section for the β-sorbed species is much higher than for the α species. However, it would be oversimplifying to imply that β Auger cross sections should be higher than α merely because the Auger electron sees a larger molecular cross section for a β-sorbed molecule lying flat on the surface than an α-sorbed molecule presenting its end view. Exact calculation of these cross sections could be made only by knowing the wave functions of the binding electrons.

What is the reason for the 2 simple β states observed on the (111) face? The β state of N_2 is apparently able to fill up to one molecule per surface W atoms without overlapping other N_2 molecules to alter the binding energy significantly. CO, however, begins to have non-zero overlap after the surface is 2/3 filled. Thus, subsequently adsorbed molecules are bound with less energy. These molecules are the first to be desorbed. It seems reasonable that such desorption should occur with first order kinetics, as was observed with N_2. Our measurement of non-integral order kinetics of CO desorption from (111) tungsten are rather difficult to accept. We would tend to attribute it immediately to instrumental effects were we not in the same period making the

reasonable measurements of N_2 desorption kinetics. Obviously, further experimental work should be done to clarify this point.

VIII. SUMMARY

In summary, we have studied adsorption at room temperature and at liquid nitrogen temperature by the flash filament and Auger techniques. We have discussed the desorption kinetics of H_2, CO, and N_2 from polycrystalline, (110), and (111) tungsten foils. H_2 is bound in the energy range .7 to 1.8 eV on all these surfaces and desorbs with multiple state kinetics. CO is bound in a β state region on polycrystalline W which actually consists of a large number of states with energies varying between 2.6 and 4.2 eV. From room temperature down to liquid nitrogen temperature (77°K), CO also forms independently an α state desorbing with multiple state kinetics, and having binding energies between approximately .7 and 1.2 eV. On (111) and (110) tungsten, an α state with about the same characteristics forms.

N_2 adsorbs on polycrystalline W in a set of many states in a smaller energy region than CO. Most of the gas is held between 3.7 and 4.3 eV. As the W is cooled below room temperature, an α state, desorbing again with multiple state kinetics and energies up to .9 eV, appears. A very similar α state of N_2 can bound on (111) W. N_2 desorbs from (111) tungsten with a unique activation energy of 3.62 eV. N_2 molecules can be adsorbed to a density of 1 molecule per surface tungsten atom and are desorbed with first order kinetics and rate constant.

$$\beta(T) = 1.88 \times 10^{12} \exp\left(\frac{-3.62\ \text{eV}}{kT}\right) \text{sec.}^{-1}$$

CO adsorbs initially with a unique, slightly lower, binding energy; but as the surface fills to its saturation value of 1 molecule per surface W atom, the unique binding energy splits into a series of lower energy multiple states.

(110) tungsten does not adsorb nitrogen until it is cooled to liquid nitrogen temperatures when N_2 adsorbs in a state of unique binding energy of .61 eV. This state desorbs with first order kinetics. The β state of CO is always small on this face.

Our experimental technique, Auger desorption spectrometry, gives promise of being useful in surface investigations. The present apparatus is limited by vacuum conditions so that adsorption of background gases interferes with studies made under conditions of low sticking coefficients. Beam stability could be improved by separating the ion source from the main vacuum chamber. This would result in more accurate determination of cross sections and kinetics. Probably the most effective way to improve the experiment would be to increase the frequency response of the circuit measuring the collector current by installing an electron multiplier within the vacuum chamber.

We felt that the power of this experimental method could best be shown by surveying the binding of many gases on various surfaces. Because we considered this work to be exploratory in nature, our results are somewhat qualitative. More detailed experiments and analysis with our present apparatus could still yield useful approximate binding state density curves. Future work must rest on exact determination of Auger

cross sections as a function of surface coverage and on detailed examination of the desorption rate curves.

LITERATURE CITED

1. Gert, Ehrlich, Ann. N. Y. Acad. Sci. 101, 722(1963).

2. Franklin, M. Propst and Thomas C. Piper, Jour. Vac. Sci. Technol. 4, 53, (1967).

3. M. Boudart, Structure and Properties of Solid Surfaces, edited by Robert Gomer and Cyril Stanley Smith (U. of Chicago Press, Chicago, 1953), p. 400.

4. J.W. May and L.H. Germer, J. Chem Phys. 44, 2895, (1966).

5. T.A. Delchar and G. Ehrlich, J. Chem. Phys. 42, 2686, (1965).

6. Gert Ehrlich, Advances in Catalysis, edited by D.D. Eley (Academic Press, N.Y., 1963), Vol. 14, p. 255.

7. Gert Ehrlich, J. Appl. Phys. 32, 4, (1961).

8. P.A. Redhead, Vacuum 12, 203 (1962).

9. L.H. Germer and A.U. MacRae, Proc. Natl. Acad. Sci., 48, 997, (1962).

10. J. Anderson and W.E. Danforth, J. Franklin Inst. 279, 160 (1965).

11. L.H. Germer, Advances in Catalysis, edited by D.D. Eley (Academic Press, New York, 1962) Vol. 13, 1962.

12. Robert Gomer, Field Emission and Field Ionization, (Harvard University Press, Cambridge, 1961).

13. Erwin W. Muller, Advances in Electronics and Electron Physics, edited by L. Marton (Academic Press, N.Y., 1960), Vol. 13, p. 83.

14. Erwin W. Muller, Science 149, 591, (1965).

15. Joseph Eisinger, J. Chem. Phys. 29, 1154, 1958.

16. T.E. Madey and John T. Yates, J. Chem. Phys. 44, 1675 (1966).

17. V.J. Mimeault and Robert S. Hansen, J. Chem. Phys. 45, 2240, (1966).

18. T.W. Hickmott, J. Chem. Phys. 32, 810 (1960).

19. Takeo Oguri, J. Phys. Soc. Japan 18, 1280, (1963).

20. L.J. Rigby, Can. Jour. Phys. 43, 532 (1965).

21. Gert Ehrlich, J. Chem. Phys. 34, 39, (1961).

22. L.J. Rigby, Can. Jour. Phys. 42, 1256 (1964).

23. M.L.E. Olephant and P.B. Moon, Proc. Roy Soc. (London) A127, 388, (1930).

24. A. Cobas and W.E. Lamb Jr., Phys. Rev. 65, 327, (1944).

25. S.S. Shekhter, J. Exptl. Theoret. Phys. (U.S.S.R.) 7, 750, (1937).

26. L.J. Varnerin Jr., Phys. Rev. 91, 859, (1953).

27. Homer D. Hagstrum, Phys. Rev. 96, 325 (1954).

28. Homer D. Hagstrum, Phys. Rev. 104, 317, (1956).

29. Homer D. Hagstrum, Phys. Rev. 104, 672, (1956).

30. Homer D. Hagstrum, Phys. Rev. 91, 543, (1953).

31. Homer D. Hagstrum, Phys. Rev. 119, 940, (1960).

32. Homer D. Hagstrum, Phys. Rev. 96, 336, (1954).

33. Homer D. Hagstrum, Phys. Rev. 122, 83, (1961).

34. Homer D. Hagstrum, Phys. Rev. 104, 1516, (1956).

35. F.M. Propst, Phys. Rev. 129, 7, (1963).

36. Franklin M. Propst and Edgar Luscher, Phys. Rev. 132, 1037, (1963).

37. Homer D. Hagstrum, Solid Surfaces, edited by H.C. Gatos (N. Holland, Amsterdam, 1964).

38. Homer D. Hagstrum, Ann. N.Y. Acad. Sci. 101, 674, (1963).

39. Homer D. Hagstrum, J. Appl. Phys. 32, 1020, (1961).

40. H.B. Hichaelson, J. Appl. Phys. 21, 536, (1950).

41. M.H. Nichols, Revs. Mod. Phys. 21, 185, (1949).

42. G. Tibbetts and F. M. Propst, Rev. Sci. Instr. 34, 1268, (1963).

43. J. A. Becker, E. J. Becker, and R. G. Brandes, J. Appl. Phys. 32, 411, (1961).

44. Gerhard Lewin, Fundamentals of Vacuum Science and Technology, (McGraw Hill, N. Y., 1965), p. 95.

45. T. W. Hickmott, Jour. Vac. Sci. Technol. 2, 257, (1965).

46. W. C. Scheumann, J. L. de Segovia, and D. Alpert, Transactions of the Tenth National Vacuum Symposium, 1963, edited by G. H. Bancroft (Macmillan Co., N. Y., 1963), p. 223.

47. Gert Ehrlich, Jour. Chem. Phys. 36, 1171, (1962).

48. J. H. DeBoer, Chemisorption, edited by W. E. Garner (Academic Press, London, 1957).

49. M. Boudart, Jour. Am. Chem. Soc., 74, 1531, (1952).

50. J. K. Roberts, Proc. Roy. Soc., (London), A152, 445, (1935).

51. M. I. Temkin, Symposium on Problems of Chemical Kinetics, Catalysis and Reactivity, Moscow, 1955.

VITA

Gary George Tibbetts was born on October 12, 1939, in Omaha, Nebraska, where he attended Central High School, graduating in 1957. He then enrolled at the California Institute of Technology in Pasadena, California, where he received the Bachelor of Science degree in physics in 1961.

In September, 1961, he began graduate study in physics at the University of Illinois. He received the Master of Science degree in February, 1963. During his graduate study at the University of Illinois he has held both teaching and research assistantships.

Publication:

G. Tibbetts and F. M. Propst, "Preparation of Thin Single-Crystal Tungsten Ribbons," Rev. Sci. Inst. 34, 1268 (1963).

DISTRIBUTION LIST AS OF APRIL 1, 1967

1 Dr. Edward M. Reilley
Asst. Director (Research)
Ofc. of Defense Res. & Engrg.
Department of Defense
Washington, D. C. 20301

1 Office of Deputy Director
(Research and Information Rm. 3D1037)
Department of Defense
The Pentagon
Washington, D. C. 20301

1 Director
Advanced Research Projects Agency
Department of Defense
Washington, D. C. 20301

1 Director for Materials Sciences
Advanced Research Projects Agency
Department of Defense
Washington, D. C. 20301

1 Headquarters
Defense Communications Agency (333)
The Pentagon
Washington, D. C. 20305

50 Defense Documentation Center
Attn: TISIA
Cameron Station, Bldg. 5
Alexandria, Virginia 22314

1 Director
National Security Agency
Attn: TDL
Fort George G. Meade, Maryland 20755

1 Weapons Systems Evaluation Group
Attn: Col. Daniel W. McElwee
Department of Defense
Washington, D. C. 20305

1 National Security Agency
Attn: R4-James Tippet
Office of Research
Fort George G. Meade, Maryland 20755

1 Central Intelligence Agency
Attn: OCR/DD Publications
Washington, D. C. 20505

1 Colonel Kee
AFRSTE
Hqs. USAF
Room 1D-429, The Pentagon
Washington, D. C. 20330

1 Colonel A. Swan
Aerospace Medical Division
Brooks Air Force Base, Texas 78235

1 AUL3T-9663
Maxwell AFB, Alabama 36112

1 AFFTC (FTBPP-2)
Technical Library
Edwards AFB, California 93523

1 Space Systems Division
Air Force Systems Command
Los Angeles Air Force Station
Los Angeles, California 90045
Attn: SSSD

1 Major Charles Waespy
Technical Division
Deputy for Technology
Space Systems Division, AFSC
Los Angeles, California 90045

1 SSD(SSTRT/Lt. Starbuck)
AFUPO
Los Angeles, California 90045

1 Det. #6, OAR (LOOAR)
Air Force Unit Post Office
Los Angeles, California 90045

1 Systems Engineering Group (RTD)
Technical Information Reference Branch
Attn: SEPIR
Directorate of Engineering Standards
& Technical Information
Wright-Patterson AFB, Ohio 45433

1 ARL (ARIY)
Wright-Patterson AFB, Ohio 45433

1 Dr. H. V. Noble
Air Force Avionics Laboratory
Wright-Patterson AFB, Ohio 45433

1 Mr. Peter Murray
Air Force Avionics Laboratory
Wright-Patterson AFB, Ohio 45433

1 AFAL (AVTE/R.D. Larson)
Wright-Patterson AFB, Ohio 45433

2 Commanding General
Attn: STEWS-WS-VT
White Sands Missile Range,
New Mexico 88002

1 RADC (EMLAL-I)
Griffiss AFB, New York 13442
Attn: Documents Library

1 Academy Library (DFSLB)
U. S. Air Force Academy
Colorado Springs, Colorado 80912

1 Lt. Col. Bernard S. Morgan
Frank J. Seiler Research Laboratory
U. S. Air Force Academy
Colorado Springs, Colorado 80912

1 APGC (PGBPS-12)
Elgin AFB, Florida 32542

1 Commanding Officer
Human Engineering Laboratories
Aberdeen Proving Ground, Maryland 21005

1 Director
U. S. Army Engineer Geodesy, Intelligence
and Mapping
Research and Development Agency
Fort Belvior, Virginia 22060

1 Commandant
U. S. Army Command and General Staff College
Attn: Secretary
Fort Leavenworth, Kansas 66270

1 Dr. H. Robl
Deputy Chief Scientist
U. S. Army Research Office (Durham)
Box CM, Duke Station
Durham, North Carolina 27706

1 Commanding Officer
U. S. Army Research Office (Durham)
Attn: CRD-AA-IP (Richard O. Ulsh)
Box CM, Duke Station
Durham, North Carolina 27706

1 Librarian
U. S. Army Military Academy
West Point, New York 10996

1 The Walter Reed Institute of Research
Walter Reed Medical Center
Washington, D. C. 20012

1 Commanding Officer
U. S. Army Electronics R&D Activity
Fort Huachuca, Arizona 85163

1 Commanding Officer
U. S. Army Engineer R&D Laboratory
Attn: STINFO Branch
Fort Belvoir, Virginia 22060

1 Commanding Officer
U. S. Army Electronics R&D Activity
White Sands Missile Range, New Mexico 88002

1 Dr. S. Benedict Levin, Director
Institute for Exploratory Research
U. S. Army Electronics Command
Fort Monmouth, New Jersey 07703

1 Director
Institute for Exploratory Research
U. S. Army Electronics Command
Attn: Mr. Robert O. Parker, Executive
Secretary, JSTAC (AMSEL-XL-D)
Fort Monmouth, New Jersey 07703

1 Commanding General
U. S. Army Electronics Command
Fort Monmouth, New Jersey 07703

Attn: AMSEL-SC
RD-D
RD-G
RD-GF
RD-MAT
XL-D
XL-E
XL-C
XL-S
HL-D
HL-CT-R
HL-CT-P
HL-CT-L
HL-CT-O
HL-CT-I
HL-CT-A
NL-D
NL-A
NL-P
NL-R
NL-S
KL-D
KL-E
KL-S
KL-T
VL-D
WL-D

1 Chief of Naval Research
Department of the Navy
Washington, D. C. 20360
Attn: Code 427

3 Chief of Naval Research
Department of the Navy
Washington, D. C. 20360
Attn: Code 437

2 Naval Electronics Systems Command
ELEX 03
Falls Church, Virginia 22046

1 Naval Ship Systems Command
SHIP 031
Washington, D. C. 20360

1 Naval Ship Systems Command
SHIP 035
Washington, D. C. 20360

2 Naval Ordnance Systems Command
ORD 32
Washington, D. C. 20360

2 Naval Air Systems Command
AIR 03
Washington, D. C. 20360

2 Commanding Officer
Office of Naval Research Branch Office
Box 39, Navy No. 100 F.P.O.
New York, New York 09510

1 AFETR Technical Library
(ETV, MU-135)
Patrick AFB, Florida 32925

1 AFETR (ETLLG-I)
STINFO Officer (For Library)
Patrick AFB, Florida 32925

1 Dr. L. M. Hollingsworth
AFCRL (CRN)
L. G. Hanscom Field
Bedford, Massachusetts 01731

1 AFCRL (CRMXLR)
AFCRL Research Library, Stop 29
L. G. Hanscom Field
Bedford, Massachusetts 01731

1 Colonel Robert E. Fontana
Department of Electrical Engineering
Air Force Institute of Technology
Wright-Patterson AFB, Ohio 45433

1 Colonel A. D. Blue
RTD (RTTL)
Bolling Air Force Base, D. C. 20332

1 Dr. I. R. Mirman
AFSC (SCT)
Andrews AFB, Maryland 20331

1 Colonel J. D. Warthman
AFSC (SCTR)
Andrews AFB, Maryland 20331

1 Lt. Col. J. L. Reeves
AFSC (SCBB)
Andrews AFB, Maryland 20331

2 ESD (ESTI)
L. G. Hanscom Field
Bedford, Massachusetts 01731

1 AEDC (ARO, INC)
Attn: Library/Documents
Arnold AFS, Tennessee 37389

2 European Office of Aerospace Research
Shell Building
47 Rue Cantersteen
Brussels, Belgium

5 Lt. Col. Robert B. Kalisch
Chief, Electronics Division
Directorate of Engineering Sciences
Air Force Office of Scientific Research
Arlington, Virginia 22209

1 U. S. Army Research Office
Attn: Physical Sciences Division
3045 Columbia Pike
Arlington, Virginia 22204

1 Research Plans Office
U. S. Army Research Office
3045 Columbia Pike
Arlington, Virginia 22204

1 Commanding General
U. S. Army Materiel Command
Attn: AMCRD-RS-DE-E
Washington, D. C. 20315

1 Commanding General
U. S. Army Strategic Communications Command
Washington, D. C. 20315

1 Commanding Officer
U. S. Army Materials Research Agency
Watertown Arsenal
Watertown, Massachusetts 02172

1 Commanding Officer
U. S. Army Ballistics Research Laboratory
Attn: V. W. Richards
Aberdeen Proving Ground
Aberdeen, Maryland 21005

1 Commandant
U. S. Army Air Defense School
Attn: Missile Sciences Division, C&S Dept.
P.O. Box 9390
Fort Bliss, Texas 79916

1 Redstone Scientific Information Center
Attn: Chief, Document Section
Redstone Arsenal, Alabama 35809

1 Commanding General
Frankford Arsenal
Attn: SMUFA-1310 (Dr. Sidney Ross)
Philadelphia, Pennsylvania 19137

1 U. S. Army Munitions Command
Attn: Technical Information Branch
Picatinney Arsenal
Dover, New Jersey 07801

1 Commanding Officer
Harry Diamond Laboratories
Attn: Dr. Berthold Altman (AMXDO-TI)
Connecticut Avenue and Van Ness Street, N.W.
Washington, D. C. 20438

1 Commanding Officer
U. S. Army Security Agency
Arlington Hall
Arlington, Virginia 22212

1 Commanding Officer
U. S. Army Limited War Laboratory
Attn: Technical Director
Aberdeen Proving Ground
Aberdeen, Maryland 21005

1 Commanding Officer
Office of Naval Research Branch Office
219 South Dearborn Street
Chicago, Illinois 60604

1 Commanding Officer
Office of Naval Research Branch Office
1030 East Green Street
Pasadena, California 91101

1 Commanding Officer
Office of Naval Research Branch Office
207 West 24th Street
New York, New York 10011

1 Commanding Officer
Office of Naval Research Branch Office
495 Summer Street
Boston, Massachusetts 02210

8 Director, Naval Research Laboratory
Technical Information Officer
Washington, D. C. 20390
Attn: Code 2000

1 Commander
Naval Air Development and Material Center
Johnsville, Pennsylvania 18974

2 Librarian
U. S. Naval Electronics Laboratory
San Diego, California 95152

1 Commanding Officer and Director
U. S. Naval Underwater Sound Laboratory
Fort Trumbull
New London, Connecticut 06840

1 Librarian
U. S. Navy Post Graduate School
Monterey, California 93940

1 Commander
U. S. Naval Air Missile Test Center
Point Mugu, California 95468

1 Director
U. S. Naval Observatory
Washington, D. C. 20390

2 Chief of Naval Operations
OP-07
Washington, D. C. 20350

1 Director, U. S. Naval Security Group
Attn: G43
3801 Nebraska Avenue
Washington, D. C. 20016

2 Commanding Officer
Naval Ordnance Laboratory
White Oak, Maryland 21162

1 Commanding Officer
Naval Ordnance Laboratory
Corona, California 91720

1 Commanding Officer
Naval Ordnance Test Station
China Lake, California 93555

1 Commanding Officer
Naval Avionics Facility
Indianapolis, Indiana 46218

1 Commanding Officer
Naval Training Device Center
Orlando, Florida 32813

1 U. S. Naval Weapons Laboratory
Dahlgren, Virginia 22448

1 Weapons Systems Test Division
Naval Air Test Center
Patuxtent River, Maryland 20670
Attn: Library

1 Head, Technical Division
U. S. Naval Counter Intelligence Support Center
Fairmont Building
4420 North Fairfax Drive
Arlington, Virginia 22203

1 Mr. Charles F. Yost
Special Asst. to the Director of Research
National Aeronautics and Space Administration
Washington, D. C. 20546

1 Dr. H. Harrison, Code RRE
Chief, Electrophysics Branch
National Aeronautics and Space Administration
Washington, D. C. 20546

1 Goddard Space Flight Center
National Aeronautics and Space Administration
Attn: Library C3/TDL
Green Belt, Maryland 20771

1 NASA Lewis Research Center
Attn: Library
21000 Brookpark Road
Cleveland, Ohio 44135

1 National Science Foundation
Attn: Dr. John R. Lehmann
Division of Engineering
1800 G Street, N.W.
Washington, D. C. 20550

1 U. S. Atomic Energy Commission
Division of Technical Information Extension
P. O. Box 62
Oak Ridge, Tennessee 37831

1 Los Alamos Scientific Laboratory
Attn: Reports Library
P. O. Box 1663
Los Alamos, New Mexico 87544

2 NASA Scientific & Technical Information
Facility
Attn: Acquisitions Branch (S/AK/DL)
P. O. Box 33
College Park, Maryland 20740

1 Director
Research Laboratory of Electronics
Massachusetts Institute of Technology
Cambridge, Massachusetts 02139

1 Polytechnic Institute of Brooklyn
55 Johnson Street
Brooklyn, New York 11201
Attn: Mr. Jerome Fox
Research Coordinator

1 Director
Columbia Radiation Laboratory
Columbia University
538 West 120th Street
New York, New York 10027

1 Director
Coordinated Science Laboratory
University of Illinois
Urbana, Illinois 61801

1 Director
Stanford Electronics Laboratories
Stanford University
Stanford, California 94305

1 Director
Electronics Research Laboratory
University of California
Berkeley, California 94720

1 Director
Electronic Sciences Laboratory
University of Southern California
Los Angeles, California 90007

1 Professor A. A. Dougal, Director
Laboratories for Electronics and Related
Sciences Research
University of Texas
Austin, Texas 78712

1 Division of Engineering and Applied Physics
210 Pierce Hall
Harvard University
Cambridge, Massachusetts 02138

1 Aerospace Corporation
P. O. Box 95085
Los Angeles, California 90045
Attn: Library Acquisitions Group

1 Professor Nicholas George
California Institute of Technology
Pasadena, California 91109

1 Aeronautics Library
Graduate Aeronautical Laboratories
California Institute of Technology
1201 East California Boulevard
Pasadena, California 91109

1 Director, USAF Project RAND
Via: Air Force Liaison Office
The RAND Corporation
1700 Main Street
Santa Monica, California 90406
Attn: Library

1 The Johns Hopkins University
Applied Physics Laboratory
8621 Georgia Avenue
Silver Spring, Maryland 20910
Attn: Boris W. Kuvshinoff
Document Librarian

1 Hunt Library
Carnegie Institute of Technology
Schenley Park
Pittsburgh, Pennsylvania 15213

1 Dr. Leo Young
Stanford Research Institute
Menlo Park, California 94025

1 Mr. Henry L. Bachmann
Assistant Chief Engineer
Wheeler Laboratories
122 Cuttermill Road
Great Neck, New York 11021

1 School of Engineering Sciences
Arizona State University
Tempe, Arizona 85281

1 University of California at Los Angeles
Department of Engineering
Los Angeles, California 90024

1 California Institute of Technology
Pasadena, California 91109
Attn: Documents Library

1 University of California
Santa Barbara, California 93106
Attn: Library

1 Carnegie Institute of Technology
Electrical Engineering Department
Pittsburgh, Pennsylvania 15213

1 University of Michigan
Electrical Engineering Department
Ann Arbor, Michigan 48104

1 New York University
College of Engineering
New York, New York 10019

1 Syracuse University
Department of Electrical Engineering
Syracuse, New York 13210

1 Yale University
Engineering Department
New Haven, Connecticut 06520

1 Airborne Instruments Laboratory
Deerpark, New York 11729

1 Bendix Pacific Division
11600 Sherman Way
North Hollywood, California 91605

1 General Electric Company
Research Laboratories
Schenectady, New York 12301

1 Lockheed Aircraft Corporation
P. O. Box 504
Sunnyvale, California 94088

1 Raytheon Company
Bedford, Massachusetts 01730
Attn: Librarian

1 Dr. G. J. Murphy
The Technological Institute
Northwestern University
Evanston, Illinois 60201

1 Dr. John C. Hancock, Director
Electronic Systems Research Laboratory
Purdue University
Lafayette, Indiana 47907

1 Director
Microwave Laboratory
Stanford University
Stanford, California 94305

1 Emil Schafer, Head
Electronics Properties Info Center
Hughes Aircraft Company
Culver City, California 90230

Security Classification

DOCUMENT CONTROL DATA - R & D

(Security classification of title, body of abstract and indexing annotation must be entered when the overall report is classified)

1. ORIGINATING ACTIVITY (Corporate author) University of Illinois Coordinated Science Laboratory Urbana, Illinois 61801	2a. REPORT SECURITY CLASSIFICATION Unclassified 2b. GROUP

3. REPORT TITLE

APPLICATION OF THE AUGER PROCESS TO THE STUDY OF GASEOUS ADSORPTION ON TUNGSTEN

4. DESCRIPTIVE NOTES *(Type of report and inclusive dates)*

5. AUTHOR(S) *(First name, middle initial, last name)*

TIBBETTS, GARY

6. REPORT DATE August, 1967	7a. TOTAL NO. OF PAGES 135	7b. NO. OF REFS 51
8a. CONTRACT OR GRANT NO. DA 28 043 AMC 00073(E) 20014501B31F; b. PROJECT NO. also in part NASA NsG-376. c. d.	9a. ORIGINATOR'S REPORT NUMBER(S) R-363 9b. OTHER REPORT NO(S) *(Any other numbers that may be assigned this report)*	

10. DISTRIBUTION STATEMENT

DISTRIBUTION OF THIS REPORT IS UNLIMITED

11. SUPPLEMENTARY NOTES	12. SPONSORING MILITARY ACTIVITY Joint Services Electronics Program thru U.S. Army Electronics Command Fort Monmouth, New Jersey 07703

13. ABSTRACT

This experiment evolved from a three-fold purpose. Firstly, it was a natural extension of previous work on the potential ejection of electrons by ions. Verifying and expanding experimental data concerning the role of adsorbed gas molecules in decreasing the number of secondary electrons could, we felt, deepen knowledge of the basic physical process.

Secondly, we hoped to gain some understanding of the binding of gases on surfaces. Modern desorption experiments have begun to point out the baffling complexity of this binding, so that new "flash filament" experiments are now as likely to produce new questions as new answers.

Thirdly, we hoped to introduce a new tool into surface investigations which could complement information gained by other techniques. While this method is admittedly far more difficult experimentally than, for instance, the flash filament technique, we hoped to show that the use of the two tools in conjunction would be a powerful experimental method.

14. KEY WORDS	LINK A		LINK B		LINK C	
	ROLE	WT	ROLE	WT	ROLE	WT
Adsorption of gases						
Desorption of gases						
Surface science						
Tungsten single crystal surfaces						
Electron ejection by low energy ions						
Auger effect						